Solutions for the flows induced by lazy, forced and pure turbulent plumes

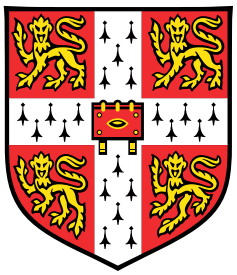

Ramanan M. Loganathan

Department of Engineering
University of Cambridge

This dissertation is submitted for the degree of
Doctor of Philosophy

St Edmund's College

January 2018

To my parents for their unparalleled love, support and dedication throughout my education. They are my inspiration and to whom I am immensely grateful as without them I would not be in this position.

Declaration

I hereby declare that except where specific reference is made to the work of others, the contents of this dissertation are original and have not been submitted in whole or in part for consideration for any other degree or qualification in this, or any other university. This dissertation is my own work and contains nothing which is the outcome of work done in collaboration with others, except as specified in the text and Acknowledgements. This dissertation contains fewer than 65,000 words including appendices, bibliography, footnotes, tables and equations and has fewer than 150 figures.

Ramanan M. Loganathan
January 2018

Acknowledgements

I am indebted to Professor Gary R. Hunt for providing this opportunity. I am eternally grateful for his wisdom and guidance, and for his constant dedication and enthusiasm throughout the journey. He has provided many thought-provoking and insightful conversations, which have inspired a number of ideas in this thesis, alongside sharing captivating stories and amusing notes that have helped me maintain a positive attitude and kept a smile on my face. Working closely with him has not only amplified my interest in and knowledge of fluid mechanics and mathematics, but has given me an education about life and inspired me to maintain a positive mindset. He has become more than a supervisor; a mentor and friend, and I hope we can continue our relationship for many years into the future.

Special thanks go to Dr Tim Jukes, Fred Nicolas and Jimmy Lirvat at Dyson Ltd. for their enthusiasm to translate the work in this thesis to commercial applications, which has provided for many interesting discussions. I also value their hospitality on visits to the company.

I am appreciative to past and present members of the research group, colleagues in the department and close friends at St Edmund's College who have supported me throughout the duration and made my time in Cambridge a fun and enjoyable experience.

The financial support provided by the Engineering and Physical Sciences Research Council and Dyson Ltd is gratefully acknowledged.

Abstract

In this thesis an analytical modelling approach is employed to predict and gain insight into the flows induced by turbulent plumes and jets above slender horizontal slots, in otherwise quiescent uniform environments. To supplement the solutions, the effect on the environment of a plume driven by an off-source supply of buoyancy was also considered. The solutions derived provide an advancement on existing idealised models for the jet and plume induced flows, and moreover, complement a number of key advances that have been made in our understanding of plume flows in recent years.

The theory of functions of a complex variable, which has not previously been applied in such an application, has been utilised as a fundamental tool throughout the work. This has enabled the entrainment behaviour and geometry of the plumes to be accounted for when developing the induced flow solutions. A novel conformal mapping has been devised specifically to account for the curved perimeter of the contracting lazy plume. This modelling approach is robust in that future developments to aspects of the modelling, for instance, the formulation of a new entrainment closure, can be straightforwardly accounted for using the method.

The induced flow solutions exhibit a range of flow patterns which are dependent on the source Richardson number of the plume flow. A pure plume induces a uniform horizontal flow. Forced and lazy plumes correspond to a relative deficit and excess in source buoyancy flux compared to the pure plume, respectively. Generally, forced plumes induce downwardly inclined flows, in contrast to lazy plumes, which induce upwardly inclined flows. Consistent with these solutions, the notionally lazy plume driven by a vertical uniform off-source supply of buoyancy induces an upwardly inclined flow.

In addition to an improved understanding of induced flows, our solutions have provided us with insight into the plume flow. Notably, the solution corresponding to the forced plume has led us to fundamentally question existing models describing the plume and, in particular, closures that have been employed to model entrainment. We find that the existing well accepted closures exhibit some form of non-physical flow behaviour.

Table of contents

Nomenclature

Symbol	Dimensions	Quantity
Coordinates		
(ξ, η)	-	Cartesian coordinate system in complex Z-plane
(ζ, Δ)	-	Cartesian coordinate system in complex W-plane
(r, θ)	L	plane polar coordinate system of induced flow
(r_a, θ_a)	L	plane polar coordinate system originating at the plume offset distance a below the horizontal boundary
$(r_{\mathrm{pc}}, \theta_{\mathrm{pc}})$	L	plane polar coordinates of fluid particle
(x, y)	L	Cartesian coordinate system of jet/plume flow
Roman Symbols		
$\bar{b}$	-	scaled plume half width, $= b/b_0$
$\bar{w}$	-	scaled plume velocity, $= w/w_0$
$\bar{y}$	-	scaled vertical coordinate, $= y/(2b_0)$
a	L	vertical plume offset
a_{h}	L	mapping constant representing horizontal translation
a_{v}	L	mapping constant representing vertical translation in the Z-plane
b	L	plume half-width
B_0	L^3T^{-3}	plume source buoyancy flux
b_0	L	plume source half-width
c_{h}	$ML^2T^{-2}\Theta$	specific heat capacity
D	L^2T^{-1}	thermal diffusivity
d	-	matching exponent

Symbol	Dimensions	Quantity
e_c	Θ^{-1}	coefficient of thermal expansion
f	-	scaled plume buoyancy flux, $= B/B_0$
F, G	-	functions mapping coordinates from Z-plane to W-plane
F_D	-	plume Froude number, $= 1/(\Gamma_0 R_p)$
g	LT^{-2}	gravitational acceleration
g'	LT^{-2}	buoyancy
Gr	-	Grashof number, $= g'y^3/\nu^2$
H	MT^{-3}	heat flux
h	$MT^{-3}\Theta^{-1}$	heat transfer coefficient
J	-	velocity shape factor
k	L^2T^{-2}	turbulent kinetic energy
K_c	-	spread rate of concentration (or scaled buoyancy flux), $= b_c/z$
K_w	-	spread rate of velocity, $= b_w/z$
l	L	characteristic streamwise distance
L_c	L	characteristic length in the induced flow
L_j	L	'jet-length'
M	L^3T^{-2}	local plume momentum flux
m	-	scaled plume momentum flux, $= M/M_0$
M_0	L^3T^{-2}	plume source momentum flux
Ma	-	Mach number
Nu	-	Nusselt number, $= Hy/(\rho_a c_p D\Delta T)$
P	ML^2T^{-3}	source power input
p	$ML^{-1}T^{-2}$	local pressure of jet/plume
Pr	-	Prandtl number, $= \nu/D$
Q	L^2T^{-1}	local plume volume flux
q	-	scaled plume volume flux, $= Q/Q_0$
Q_0	L^2T^{-1}	plume source volume flux
Q_t	L^2T^{-1}	source volume flux of tracer
R	-	alternative local plume Richardson number/flux balance parameter, $= BQ^3/M^3$
R_0	-	alternative source plume Richardson number/flux balance parameter, $= B_0{Q_0}^3/{M_0}^3$
r_{it}	L	radial coordinate of image source of tracer

Symbol	Dimensions	Quantity
r_t	L	radial coordinate of source of tracer
r_u	L	radius of the 'unit' contour
Ra	-	Rayleigh number, $= g'y^3/(D\nu)$
Re	-	Reynolds number, $= UL_\mathrm{c}/\nu$
s	L	displacement along induced flow streamline
T	Θ	temperature
U	LT^{-1}	speed of induced flow, $= \lvert\nabla\chi\rvert$
u	Θ	relative temperature of metal plate
u_r	LT^{-1}	radial component of velocity
u_e	LT^{-1}	entrainment velocity
U_t	LT^{-1}	speed of tracer
u_θ	LT^{-1}	angular component of velocity
v	-	coefficient of interior angle of the polygon
W	T^{-2}	time averaged square of vorticity fluctuations
w_0	LT^{-1}	source velocity
w_x	LT^{-1}	horizontal velocity component of jet
w_y	LT^{-1}	vertical velocity component of jet
w_m	LT^{-1}	(maximum) centre-line velocity
y_sc	L	virtual origin source correction
z	-	complex coordinate in the Z-plane
H	-	Heaviside step function

Greek Symbols

α_j	-	jet entrainment coefficient
α_p	-	plume entrainment coefficient
β	L^2T^{-3}	source buoyancy flux of vertically distributed plume
$\boldsymbol{\Psi}$	L^2T^{-1}	three-dimensional stream function vector
$\boldsymbol{w}$	LT^{-1}	three-dimensional velocity vector
χ	L^2T^{-1}	scalar component of stream function vector $\boldsymbol{\Psi}$
χ_vdp	L^2T^{-1}	vertically distributed plume boundary condition
δ	L	coordinate of edge of plume source in Z-plane
ε	L^2T^{-3}	dissipation rate of turbulent kinetic energy
ε_j	-	jet coefficient
ε_p	-	plume coefficient

Symbol	Dimensions	Quantity
ε_t	$ML^{-1}T^{-1}$	'virtual' eddy viscosity
η	-	similarity coordinate, = $\sigma x/y$
Γ	-	local Richardson number, $= BQ^3/(2^{3/2}\alpha M^3)$
γ	-	mapping exponent
Γ_0	-	source Richardson number, $= B_0{Q_0}^3/(2^{3/2}\alpha {M_0}^3)$
κ	-	ratio of jet and plume entrainment coefficients, $= \alpha_j/\alpha_p$
λ	-	separation of variables constant
ν	$ML^{-1}T^{-1}$	kinematic viscosity
ω	L	complex coordinate in the W-plane
ϕ	-	entrainment closure defined in terms of spreading rates
Ψ	-	scaled stream function, $= \chi/\chi_0$
ρ	ML^{-3}	density of plume
ρ_0	ML^{-3}	source density of plume
ρ_a	ML^{-3}	density of ambient
ρ_o	ML^{-3}	reference density
σ	-	spreading rate of jet, $= y/b$
τ	$ML^{-1}T^{-2}$	flow shear stress
θ_b	-	angular coordinate of horizontal boundary
θ_i	-	angular coordinate of initial position of a fluid particle in induced flow
θ_j	-	inclination of induced flow streamlines at perimeter of jet
θ_{max}	-	maximum inclination of induced flow streamlines at perimeter of plume
θ_{min}	-	angular coordinate of transition from deceleration to acceleration of a fluid particle in induced flow
θ_p	-	inclination of induced flow streamlines at perimeter of plume
θ_{vdp}	-	angular coordinate of perimeter of vertical distributed plume
θ_Z	-	angular coordinate in complex Z-plane
ζ_L	-	height above which plume entrainment velocities fall
ζ_{max}	-	height of maximum inclination of induced flow streamlines at perimeter of plume

Symbol	Dimensions	Quantity
ζ_{n}	-	plume neck height
ζ_{tp}	-	height of turning point

Subscripts

$(\cdot)_l$	-	value at characteristic distance l
$(\cdot)_0$	-	value at source
$(\cdot)_{\mathrm{b}}$	-	horizontal boundary
$(\cdot)_{\mathrm{fp}}$	-	forced plume
$(\cdot)_{\mathrm{f}}$	-	far-field
$(\cdot)_{\mathrm{j}}$	-	jet
$(\cdot)_{\mathrm{lp}}$	-	lazy plume
$(\cdot)_{\mathrm{m}}$	-	centre-line velocity
$(\cdot)_{\mathrm{n}}$	-	near-field
$(\cdot)_{\mathrm{pc}}$	-	fluid particle in induced flow
$(\cdot)_{\mathrm{p}}$	-	plume/pure plume
$(\cdot)_{\mathrm{sc}}$	-	source correction
$(\cdot)_{\mathrm{tp}}$	-	turning point
$(\cdot)_{\mathrm{t}}$	-	tracer
$(\cdot)_{\mathrm{vdp}}$	-	vertical distributed plume

Chapter 1

Preface

Turbulent plumes are widely encountered in everyday life, from the evaporated water vapour above a hot cup of coffee, to the exhaust gases observed rising from a domestic chimney stack or flue of a power plant, or at a larger scale, the air above so-called urban heat islands created by densely populated cities. These flows are driven by a density difference between the source fluid and surrounding environment. A visualisation of a turbulent plume is shown in figure 1.1 (a), where warm water is continuously released from a slender horizontal slot into a cooler, otherwise quiescent, environment. A turbulent jet, illustrated in figure 1.1 (b), by contrast, has no such density difference with the environment, and is instead driven by a high velocity injection of fluid. Examples of turbulent jets include the effluent of drainage water issuing from a submerged pipe into a river body, the flow from a room or desk fan used to maintain occupant comfort and the emptying of rivers into lakes and estuaries. Turbulent jets and plumes create local low pressure regions relative to their environments. Consequently, these flows entrain across their perimeters, which is represented by a well-defined (though irregularly moving) interface (Townsend, 1976), and simultaneously induce a slower bulk secondary inflow. The inflow, referred to as the induced flow, is illustrated using a streakline of dye in figure 1.1, and the (white) smoke filaments in figure 1.2. Two features are immediately apparent from the visualisations. Firstly, by contrast to the turbulent jet and plume, the induced flow is laminar, and rather unexpectedly, the induced flow of the jet is inclined downwards towards the source. The difference between the jet and plume induced flows in the figures indicates that the source conditions of a turbulent flow can have a pronounced effect on the flow pattern induced in the surrounding environment. Figure 1.3 is a visualisation from van Dyke (1982) of the laminar flow induced by an unconfined jet issuing from a horizontal slot. By contrast to the induced flows in figures 1.1 and 1.2, in this configuration, fluid is drawn in from below the source with an upward inclination. Thus, removing the horizontal boundary adjacent to the source also has a pronounced effect on the

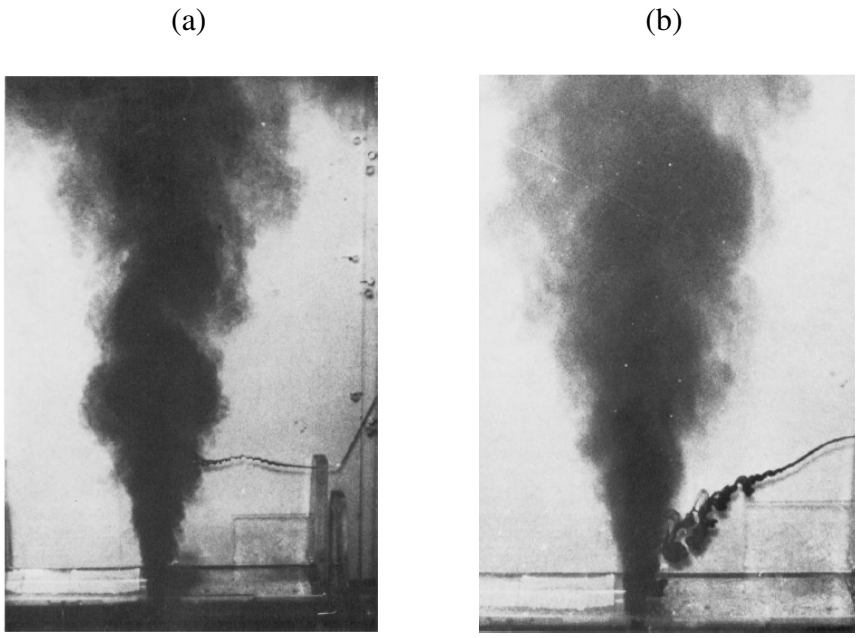

Fig. 1.1 Photographs from Kotsovinos (1977) (taken after 2 seconds) of a turbulent (a) pure plume and (b) jet following a continuous discharge of water from a slot in a horizontal boundary. The dye lines in the ambient illustrate the contrasting flow patterns that are induced external to the perimeters of the jet and plume.

flow pattern induced. Induced flows have been directly exploited in numerous applications. For instance, in World War I, plume induced flows created by lighting a line of oil drum fires on the side of aircraft runways were used to clear fog (Taylor, 1958). Plume induced flows also play an integral role in setting the pattern of bulk air motion in naturally ventilated buildings (Hunt & van den Bremer, 2011), and in the coalescence and dilution of plumes rising from multiple sources in close proximity (see Kaye & Linden (2004), Rooney (2015)), for instance, the flow above a row of chimneys. As shown in Hunt (1994), the Aaberg exhaust hood specifically utilised the induced flow of a radial jet to create a stronger suction to remove pollutants and toxic fumes in industrial environments.

Modelling induced flows enables one to predict the effect that jets and plumes have on their surrounding environments, and further, to elucidate the key physics of the induced flows. Taylor (1958) introduced the seminal approach to theoretically model induced flows. He devised solutions for the flow induced by an (idealised) steady turbulent line jet issuing from a slot (of infinite length and infinitesimal width), into an unconfined environment, as well as out from a horizontal boundary. These solutions were found to broadly have close (qualitative) agreement with the visualisations in figures 1.2 and 1.3. Taylor's (1958) induced flow solutions for the line jet have been widely applied, examples of which include, to model

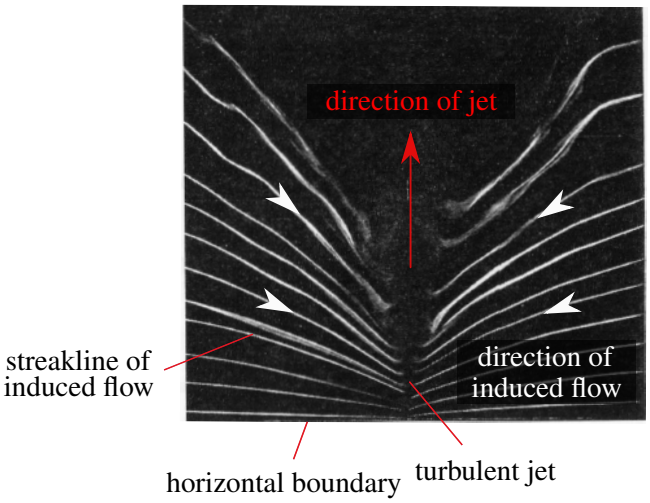

Fig. 1.2 Flow visualisation from Lippisch (1958), taken at a cross-section along the spanwise extent of the flow, illustrating the (white) streaklines of the secondary motion induced by a turbulent jet issuing vertically from a slot in a horizontal boundary.

the circulation induced by a tidal jet in an ebbing ocean (see Joshi & Taylor (1983)), and to represent the motion induced into the turbulent flow originating from multi-port diffusers (see Adams & Trowbridge (1985)). In addition to the jet induced flows, Taylor (1958) proposed a solution for the flow induced by a steady turbulent line plume rising vertically from a horizontal boundary. The solution is (qualitatively) consistent with observations in Rankine's wind tunnel experiments which are discussed in Taylor (1961). The general modelling approach taken and the induced flow solutions derived in Taylor (1958) are detailed in Chapter 2.

There has been little advancement in the modelling of induced flows since the early work of Taylor (1958). In particular, our knowledge of induced flows has not kept pace with recent developments that have occurred in our understanding of plumes, particularly those issuing from (non-idealised) sources with a finite velocity and buoyancy input. Non-idealised plume flows broadly fall into one of three flow regimes; namely pure, forced or lazy (Morton, 1959). Pure plumes maintain a local balance of (inertial and buoyancy) forces that act on the flow. These flows are formed above an idealised source of buoyancy, but more realistically, when the source supply of fluid at a non-idealised source has a balance of the forces. The plume in figure 1.1 (a) is an example of the latter, as in the experiment, water forming the plume is warm relative to the environment and so gives rise to the buoyancy force, and is injected giving rise to the inertia force. Pure plumes have been the subject of some of the earliest work on plumes (e.g. Yih (1951), Rouse et al. (1952)), and whose flow characteristics are generally regarded as well-understood. Their more complex (non-pure) counterparts,

Fig. 1.3 Flow visualisation from van Dyke (1982) of streamlines (marked by tiny air bubbles) of the induced flow of a turbulent unconfined (water) jet, with source velocity 1 ms^{-1}, issuing from a horizontal slot.

specifically the non-idealised forced and lazy plumes, corresponding to a relative excess in inertial and buoyancy forces, respectively (see Chapter 2), have been the focus of more recent work. Significant progress has been made in our understanding of their large-scale flow physics (see Morton (1959), Morton & Middleton (1973), Kotsovinos (1975), van den Bremer & Hunt (2014)) and entrainment characteristics (see List & Imberger (1973), List & Imberger (1975), Kotsovinos & List (1977), van Reeuwijk & Craske (2015), van Reeuwijk et al. (2016), Carlotti & Hunt (2017)). Despite these advancements, however, we have no knowledge of the effect that non-idealised plumes have on their environments. Building on the classic work of Taylor (1958), in this thesis our goal is to complement the recent developments that have occurred in our understanding of these plumes, and bridge the gap in our knowledge of their corresponding induced flows. Following a derivation of the induced flow solution for the (non-idealised) pure plume in Chapter 2, as a straightforward extension of the solution for the line plume induced flow from Taylor (1958), our main focus and challenge faced is to model the flows induced by non-pure plumes. Consequently, the broad aim of the research is to:

develop a modelling capability and to enhance our understanding of the flows induced by turbulent plumes, with a particular focus on non-pure plumes, issuing from slender horizontal sources into otherwise quiescent environments.

With this aim in mind, the specific objectives are as follows:

- to compare the flows induced by the (idealised) line jet and line plume, and discuss the implications for the movement and control of the surrounding air;

- to model and develop insight into the flow induced by contracting lazy plumes issuing from slender horizontal sources;

- to model and gain insight into the induced flow of notionally lazy plumes that are formed via an off-source supply of buoyancy; and

- to model the flow induced by forced plumes above a slender horizontal source, in order to determine the effect that increasing the relative forcing at the source has on the induced flow.

Prior to discussing the work undertaken in the subsequent chapters, we rationalise our choice of objectives. Though our focus in this thesis is primarily to gain insight into non-pure plume induced flows, we begin with work inspired by the induced flow solutions for the (idealised) line jet and line plume from Taylor (1958). Specifically, we develop a set of quantitative diagnostics that utilise these induced flow solutions as a means to compare the effect that the jet and plume, flows driven by fundamentally different mechanisms, have on their respective environments. Following this, our attention turns to modelling the flows induced by the (non-idealised) non-pure plumes, and specifically those that are Boussinesq, i.e. maintain small density differences with the ambient. Non-pure plumes have been the subject of a wide body of work undertaken within the research group in recent years. Significant developments have occurred in our understanding of lazy plumes above horizontal sources (see Hunt & Kaye (2005), Carlotti & Hunt (2005), Carlotti & Hunt (2017)) and following an off-source supply of buoyancy (see Cooper & Hunt (2010)). These advancements inspired us to consider the effect that these plumes have on their surrounding environment. On gaining an understanding of the flows induced by lazy plumes, which correspond to an excess in the supply of buoyancy (or equivalently a deficit in the supply of inertia) relative to the pure plume, we proceed to consider the effect of a relative deficit of buoyancy (or a relative excess of inertia) at the source. This study of both lazy and forced

plumes provides us with a more complete picture of the role that the source conditions of the plume flow plays on the flow induced in the environment.

In Chapter 3 we propose two diagnostics, referred to as the 'Velocity Ratio' and 'Bounding Locus' methods, in order to directly compare the effect that the line jet and line plume have on their surrounding environments. In addition to enabling the direct comparison of these two induced flows, the diagnostics enable one to assess some of the wider implications of the difference between a velocity and buoyancy input at the source for the movement and control of surrounding air. Following this, our focus turns to modelling the flows induced by turbulent plumes issuing from more complex (non-idealised) non-pure sources. More specifically, in Chapter 4 we use the theory of functions of a complex variable (outlined in Chapter 2), to model the flow induced by the contracting lazy plume above a slender horizontal slot. This approach has not previously been applied to model induced flows. Indeed a new conformal mapping was required in order to apply the method so as to account for the curved geometry of the contracting plume perimeter. The solution for the flow induced by the plume that is formed via an off-source supply of buoyancy, namely the vertically distributed plume, is developed in Chapter 5. To provide a more complete picture of the effect of the plume source conditions, and determine the role played by the relative forcing at the source, we adopt an analogous approach to that in Chapter 4 to model the flow induced by the forced plume in Chapter 6. In Chapter 7 we challenge many of the accepted assumptions and models employed in the earlier chapters. Conclusions are drawn in Chapter 8.

The contents of Chapter 3 were presented at the 2016 British Applied Mathematics Colloquium (5 - 8th April) at the University of Oxford. The work in Chapters 4 and 5 on modelling the flow induced by the lazy plume and the vertically distributed plume are ready for submission for publication in an international journal, and model development based on the insights gained from the latter chapters is currently under progress, with the aim of publishing in the near future.

Chapter 2

Methodology

The aim of this chapter is twofold. Firstly, to discuss the fundamental physics of induced flows and outline the general approach taken in the literature to theoretically model them, and secondly, to equip the reader with the mathematical tools that are central to the development of the new induced flow models in subsequent chapters.

Turbulent flows entrain ambient fluid across their perimeter, drawing a slower external laminar inflow — which we refer to as the induced flow. In contrast to the highly unsteady turbulent flow, the laminar induced flow is steady. Illustrations of induced flows were presented in figures 1.1, 1.2 and 1.3. Viewing a turbulent flow from the reference frame of the ambient, the flow acts as a sink of fluid. The magnitude and vertical distribution of the sink strength, properties which are inherently governed by the entrainment characteristics of the turbulent flow, define the corresponding external flow that is induced. We broadly discuss the entrainment characteristics of a jet and pure plume flow above a horizontal slot in the following.

A jet is driven by a high velocity injection of fluid. Turbulent frictional Reynolds stresses in the jet flow continuously dissipate energy and deplete the source supply of kinetic energy with height. Consequently, the jet has increasingly less energy available for entrainment, and the local entrainment velocity at the perimeter of the jet falls. To satisfy the increased entrainment demand closer to the source, the jet issuing from a horizontal boundary induces an inflow that is downwardly inclined towards the source. Thus, fluid is drawn into the jet at a given streamwise location from downstream in the ambient, as is evident in the visualisation in figure 1.2 from Lippisch (1958).

A pure plume forms above an idealised source of buoyancy or when buoyant fluid is injected from a source with a balance of inertial and buoyancy forces. Buoyancy continuously does work with height and compensates for the energy that is dissipated by the plume's

turbulent Reynolds stresses. As a consequence, the pure plume entrains at a constant rate with height. This leads to a horizontal flow induced by the plume issuing vertically from a horizontal boundary. Such a flow pattern is observed in figure 1.1 (a) and confirmed from Rankine's wind tunnel experiments which are discussed in Taylor (1961). Rankine observed that the vertical convection currents rising above a row of burners placed on the floor of a wind tunnel produced a uniform inflowing current in the ambient on each side of the plume.

2.1 Solution method

Having broadly discussed the entrainment characteristics of jets and pure plumes and the resulting flow patterns that are induced, our attention turns to modelling the induced flows. Taylor (1958) introduced the seminal approach to model jet and plume induced flows in otherwise quiescent environments. Jets and plumes issuing from sources with a length that is long relative to their width will have flow properties that have relatively small variation along the spanwise extent in comparison to the cross-stream and vertical directions. Consequently, flow properties are averaged along the spanwise extent. Properties are also averaged over time so as to model mean flow behaviour. Thus, jets and plumes, and their respective induced flows, are modelled using a (double-averaged) two-dimensional model. Taylor (1958) models the induced flow as an (inviscid) potential flow governed by the Laplace equation,

$$\nabla^2 \chi = 0, \tag{2.1}$$

where χ denotes the scalar stream function. Expression (2.1) follows from observations that the induced flow is low speed, with $Ma << 1$ (where Ma denotes the Mach number of the flow), laminar and absent of any large velocity gradients (cf. figure 1.2). These observations led Taylor to represent the induced flow as irrotational ($\nabla \times \mathbf{w} = 0$, where $\mathbf{w}$ denotes the three-dimensional velocity vector with a zero spanwise component) and incompressible ($\nabla \cdot \mathbf{w} = 0$). Utilising the divergence free property to represent the velocity in terms of the scalar stream function χ, as

$$\mathbf{w} = \nabla \times \mathbf{\Psi} \quad \text{where} \quad \mathbf{\Psi} = (0, 0, \chi) \tag{2.2}$$

denotes a vector potential, the irrotationality condition can be redefined to give the Laplace equation in (2.1).

In order to develop a boundary condition for the effect of the jet/plume flow on the environment, jets and plumes are modelled using a vertical distribution of line sinks (or equivalently two-dimensional point sinks in the plane), with local strength governed by the

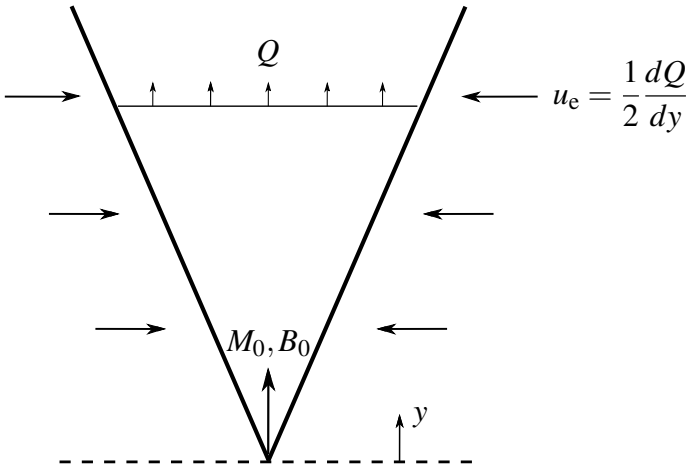

Fig. 2.1 Schematic of a cross-section along the spanwise extent of the flow which indicates a well-defined perimeter (bold) that separates the turbulent jet/plume flow from the laminar inflow induced in the environment. The relevant physical quantities to the problem (as defined in the text) have been included in the schematic.

local velocity of the fluid entrained into the jet or plume at that height. The local entrainment velocity is given by $u_e = (1/2) \cdot dQ/dy$ (where Q ($m^2 s^{-1}$) (defined in Appendix A) denotes the local flux of volume per unit length along the plume), and is shown in the schematic in figure 2.1. The entrainment velocity is equivalent to the local vertical gradient of the stream function, i.e. $u_e \equiv d\chi/dy$. With this knowledge, Taylor formulates a boundary condition for the jet and plume in terms of χ. Pertinent to the fully developed flow regime, following dimensional arguments Taylor derives the expressions,

$$\chi = \chi_j = \varepsilon_j {M_0}^{1/2} y^{1/2} \tag{2.3}$$

and

$$\chi = \chi_p = \varepsilon_p {B_0}^{1/3} y, \tag{2.4}$$

to represent the jet and pure plume flows, respectively, issuing from an idealised line source (of infinitesimal width and infinite length) with a zero source supply of fluid. The subscripts '$(\cdot)_j$' and '$(\cdot)_p$' refer to the jet and pure plume, respectively, and is notation used throughout the thesis. The quantities $M_0 \propto Q_0 w_0$ and $B_0 \propto Q_0 g'_0$ (which are formally defined in Appendix A) represent the fluxes per unit length of momentum and buoyancy, respectively, supplied at each source (where the subscript '0' corresponds to the source value and is notation used hereinafter). The term w_0 denotes the source velocity, Q_0 the source volume flux

per unit length and $g'_0 = g(\rho_0 - \rho_a)/\rho_a$ the source buoyancy, where ρ_0 and ρ_a represent the plume source and ambient densities, respectively, and g the gravitational acceleration. The fluxes of momentum M_0 and buoyancy B_0 per unit length are finite (as the singular jet source velocity w_0 and plume source buoyancy g'_0 compensate for the respective zero source fluxes per unit length of volume Q_0) and remain invariant with height in a uniform environment. In the interest of conciseness, we direct the reader to Appendix A for details on the invariance of these fluxes, where it is identified that the momentum flux per unit length is conserved on integrating the shear-layer equations, and that the buoyancy flux per unit length is conserved when formulating the plume equations by appropriately manipulating the definition of the quantity. The coefficients ε_j and ε_p in (2.3) and (2.4), respectively, are dimensionless constants that are evaluated in §2.1.1. All fluxes considered hereinafter are per unit length, unless otherwise stated, and for conciseness, we do not mention this when defining or referring to fluxes from this position onwards. Noting the equivalence between the entrainment velocity and vertical gradient of the stream function as stated previously, we take the vertical gradient of the expressions in (2.3) and (2.4), to give

$$u_e = \frac{d\chi_j}{dy} = \frac{1}{2}\varepsilon_j {M_0}^{1/2} y^{-1/2} \quad \text{and} \quad u_e = \frac{d\chi_p}{dy} = \varepsilon_p {B_0}^{1/3}. \tag{2.5}$$

From the scalings on the vertical coordinates in these expressions, we identify that the jet acts as a sink that decreases in strength with height, in contrast to the plume, which maintains a fixed sink strength.

Taylor (1958) considered two environments when modelling jet and plume induced flows; a free unconfined ambient, and a partially-confined ambient whereby the flow issues from a horizontal boundary. To account for these configurations a second boundary condition corresponding to a streamline is imposed. The streamline represents the horizontal boundary for the partially-confined flow (i.e. the slip condition), and the vertical plane of symmetry below the source in the case of the unconfined flow. Schneider (1981) pointed out that the error resulting from assuming the slip condition at the horizontal boundary of the partially-confined flow is negligible when modelling the flow induced by turbulent flows above slender sources. This is based on order of magnitude arguments, using which Schneider (1981) identifies that the local Reynolds number $Re = UL_c/\nu$ (where ν is the kinematic viscosity), in the turbulent jet/plume flow is of the same order of magnitude as the laminar induced flow. Despite speeds in the induced flow, U, being an order of magnitude lower compared with that of the jet/plume, the characteristic length, L_c, over which the induced flow occurs is significantly larger. Analogous to the turbulent jet/plume, the effects of the fluid's viscosity

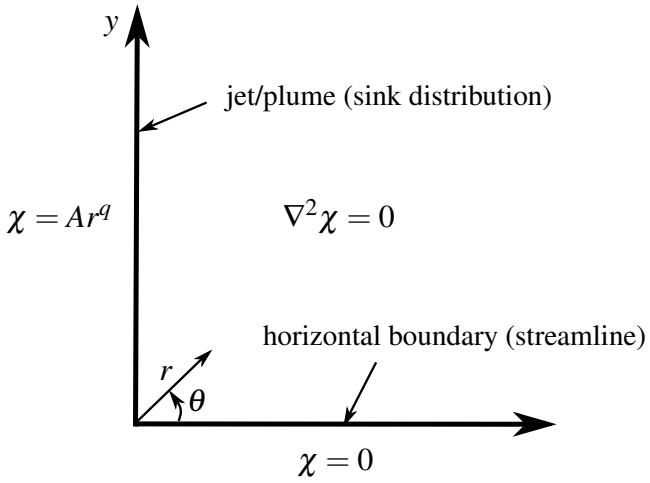

Fig. 2.2 Boundary value problem describing the flow induced by the line jet/plume issuing vertically out of a horizontal boundary.

is negligible to a first-order approximation in the external induced flow, and the assumption of the slip condition at the solid boundary is justified.

Introducing the plane polar coordinates (r, θ) that originate at the source of the jet/plume flow, with θ taken anti-clockwise from the positive horizontal axis, Taylor (1958) models the induced flows using Laplace's equation (2.1), subject to the jet/plume boundary condition

$$\chi = Ar^q \quad \text{at} \quad \theta = \pi/2, \tag{2.6}$$

and the streamline

$$\chi = 0 \quad \text{on} \quad \theta = 0 \quad \text{or} \quad \theta = -\pi/2. \tag{2.7}$$

The constants, identified from (2.3) and (2.4), are $A = \varepsilon_{\mathrm{j}} {M_0}^{1/2}$ and $q = 1/2$ for the jet, and $A = \varepsilon_{\mathrm{p}} {B_0}^{1/3}$ and $q = 1$ for the pure plume. The streamlines along $\theta = 0$ and $\theta = -\pi/2$ correspond to the partially-confined and unconfined flows, respectively. Figure 2.2 is a schematic of the governing boundary value problem for the flow induced by the jet/plume in the partially-confined environment. Notice in the formulation above that only half of the induced flow has been modelled due to the plane of symmetry along the jet and plume centre-lines. The jet and pure plume are slender (i.e. $b << y$, where b is the local flow width) and straight-sided (Schlichting, 1968). Therefore, Taylor (1958) approximates the jet and plume flows as having an infinitesimal width by applying the jet/plume boundary condition along the vertical axis at $\theta = \pi/2$ in (2.6). The local vertical coordinate y in (2.3) and (2.4) has also been matched with the global coordinate r of the induced flow along the vertical axis.

Flow type	χ	U
Partially-confined plume	$\varepsilon_\mathrm{p} {B_0}^{1/3} r\sin\theta$	$\varepsilon_\mathrm{p} {B_0}^{1/3}$
Partially-confined jet	$2^{1/2}\varepsilon_\mathrm{j} {M_0}^{1/2} r^{1/2}\sin(\theta/2)$	$\varepsilon_\mathrm{j} {M_0}^{1/2} r^{-1/2}/2^{1/2}$
Unconfined jet	$\varepsilon_\mathrm{j} {M_0}^{1/2} r^{1/2}(\cos(\theta/2)+\sin(\theta/2))/2^{1/2}$	$\varepsilon_\mathrm{j} {M_0}^{1/2} r^{-1/2}/2$

Table 2.1 Induced flow solutions from Taylor (1958) for the stream function χ and speed U.

Taylor (1958) solved the governing boundary value problem ((2.1) subject to (2.6) and (2.7)) to obtain the solutions presented in table 2.1 for the stream function, χ, and corresponding speed, $U = |\nabla \times \boldsymbol{\Psi}|$, of the line jet and line plume induced flows (with '$|\cdot|$' denoting the magnitude of the vector). The solutions can be derived by identifying the general solution to Laplace's equation for χ, for instance, using the method of separation of variables, and matching the general solution to the corresponding boundary conditions in (2.6) and (2.7) (cf., for example, the analysis given in §2.3.1).

2.1.1 Evaluating the jet and plume coefficients

Prior to illustrating and discussing the solutions in table 2.1, we evaluate the coefficients ε_p and ε_j. These coefficients account for the turbulent entrainment into the jet and plume.

Experiments as early as those by Rouse et al. (1952), and later by Kotsovinos (1975), showed that (time-averaged) cross-stream profiles of velocity w and buoyancy g' in a slender vertical turbulent plume collapse onto a single bell-shaped curve once suitably scaled, i.e. the properties are self-similar. Assuming self-similar Gaussian profiles, Lee & Emmons (1961) formulate a coupled system of ordinary differential equations in terms of integral fluxes — the so-called plume (conservation) equations — to describe the plume. Solving the plume equations, the plume coefficient is identified as

$$\varepsilon_\mathrm{p} = {\alpha_\mathrm{p}}^{2/3} \tag{2.8}$$

(see §A.1 in Appendix A). The term $\alpha = \alpha_\mathrm{p}$ is the entrainment coefficient, which relates a local characteristic velocity in the plume to the local inflow velocity at the plume perimeter. There is a considerable spread in the values of α_p inferred from measurements. For example, Kotsovinos (1975) give $\alpha_\mathrm{p} = 0.10$, Lee & Emmons (1961) give $\alpha_\mathrm{p} = 0.16$ and Yuana & Cox (1996) give $\alpha_\mathrm{p} = 0.13$ (see table 1 in van den Bremer & Hunt (2014)). Herein, an average

value of $\alpha_p = 0.13$ has been used for the plume. The integral approach outlined above can also be straightforwardly employed for the jet (with $g' = 0$) to give

$$\varepsilon_j = 2^{1/4}\alpha_j{}^{1/2} \tag{2.9}$$

(see §A.1 in Appendix A). Values of the jet entrainment coefficient $\alpha = \alpha_j$ have a lower value, measured as 0.04 – 0.06 (Kotsovinos, 1975), 0.05 – 0.06 (Chen & Rodi, 1980) and 0.05 (Antonia et al., 1983) (see table 1 in van den Bremer & Hunt (2014)). Kotsovinos (1977) argues that the larger value of α for the plume is attributed to the contribution of buoyancy to the flow's turbulent energy, and the build up of turbulent 'eddies' to the scale of the plume width to create large-scale engulfment of ambient fluid. The differences in the entrainment behaviour are discussed further in Chapter 6 when modelling the flow induced by forced plumes.

The jet coefficient can alternatively be determined in terms of the spreading rate $\sigma = y/b$, as

$$\varepsilon_j = 3^{1/2}\sigma^{-1/2}/2 \tag{2.10}$$

(see §A.2 in Appendix A). This expression is based on Görtler's (self-similar) solution as derived upon directly solving the shear-layer equations with an eddy viscosity turbulence closure. The spreading coefficient has been measured by Reichardt (1942) as $\sigma = 7.67$.

2.2 Analysis of solution

Figure 2.3 illustrates streamlines, $\chi = const.$, and corresponding contours of constant speed, $U = const.$, of a cross-sectional plane in the induced flow of the jet issuing vertically from a horizontal boundary. The illustration is plotted using the solution in table 2.1 from Taylor (1958) (with the coefficient ε_j in (2.10) with $\sigma = 7.67$). All streamline portraits presented hereinafter are presented in such a cross-sectional plane. For illustrative purposes we have chosen a source strength $M_0 = 1.087$ m^{3}s^{-2} in figure 2.3, corresponding to a jet centre-line velocity, $w_m = (3M_0\sigma/4)^{1/2} = 2.5$ ms^{-1} (see expression (A.32) in Appendix A), at a metre downstream. This velocity is not unrepresentative of a typical flow velocity required to cool occupants in an office during the summer months (Aynsley, 2007), and so simply to add context, the streamline pattern could be regarded as that in a room. Figure 2.3 indicates that a bulk inflow is drawn in (in the direction indicated by the arrows) towards the jet (located at the vertical axis). The flow has a downward inclination, qualitatively consistent with the visualisation from Kotsovinos (1977) in figure 1.1 (b) and Lippisch (1958) in figure 1.2. Moreover, streamlines of the induced flow visualised in experiments by Giger et al. (1991)

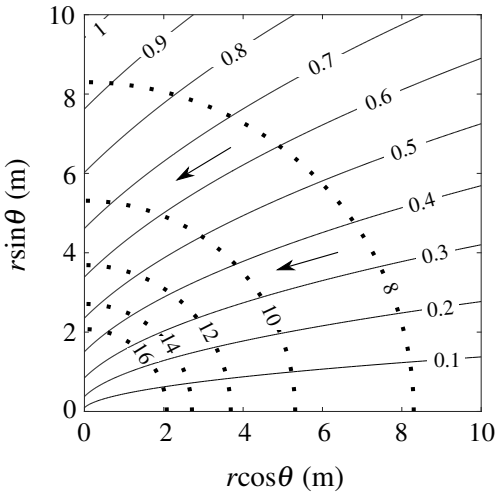

Fig. 2.3 Streamlines (solid lines) and contours of constant speed (dotted lines) of the flow induced by a partially-confined line jet with $M_0 = 1.087$ m^{3}s^{-2}. The induced flow is partially confined by a horizontal boundary at the level of the source along $\theta = 0$. Values of the stream function (m^{2}s^{-1}) corresponding to each streamline and flow speeds ($\times 10^{-2}$ ms^{-1}) are overlain on each contour. Arrows indicate the direction of motion.

are claimed to be in close agreement with those output using the solution (see figure 3 in Giger et al. (1991)). Interestingly, the jet's reducing entrainment demand with height has not been satisfied using a horizontal inflow with large vertical velocity gradients, but instead with a downwardly inclined flow and weak vertical velocity gradients. The induced flow streamlines maintain an angle of $\theta = 45^\circ$ along the jet edge. This inclination remains constant along the edge owing to the fixed rate with which the jet entrainment velocity falls with vertical extent, i.e. $u_e \propto y^{-1/2}$, and due to the singularity at the source. The reducing spacing between adjacent streamlines towards the jet implies (based on volume conservation) that fluid particles in the induced flow are accelerating towards the jet. The acceleration is also evident from the contours of constant speed that have been overlain onto the streamlines.

Figure 2.4 plots streamlines, $\chi = const.$, and corresponding contours of constant speed, $U = const.$, for the unconfined jet using the solution in table 2.1. The induced flow streamlines are (qualitatively) consistent with the visualisation from van Dyke (1982) illustrated in figure 1.3. Immediately apparent, upon comparison with the induced flow of the partially-confined jet in figure 2.3, is the key role played by confinement on the resulting induced flow. By contrast to the partially-confined jet, fluid in the unconfined environment is drawn from below the source with an upward inclination to satisfy the entrainment demand. The induced flow streamlines are (close to) horizontal at the jet perimeter. The induced flow, in general, has a lower speed in the unconfined environment, as a result of the greater extent of the domain.

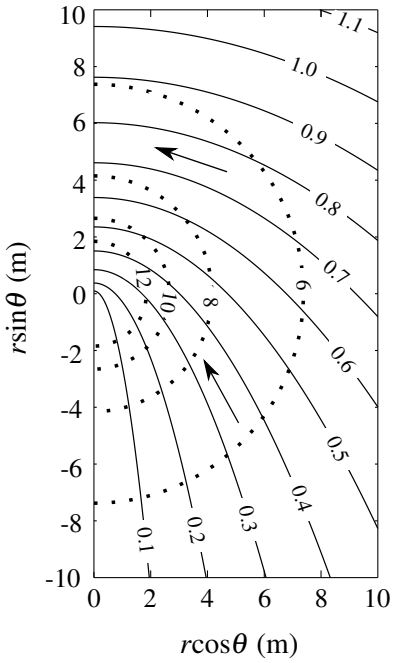

Fig. 2.4 Streamlines (solid lines) and contours of constant speed (dotted lines) of the flow induced by an unconfined line jet with $M_0 = 1.087$ m^{3}s^{-2} (identical in strength to the partially-confined jet in figure 2.3). Values of the stream function (m^{2}s^{-1}) corresponding to each streamline and flow speeds induced ($\times 10^{-2}$ ms^{-1}) are overlain on each contour. Arrows indicate the direction of motion.

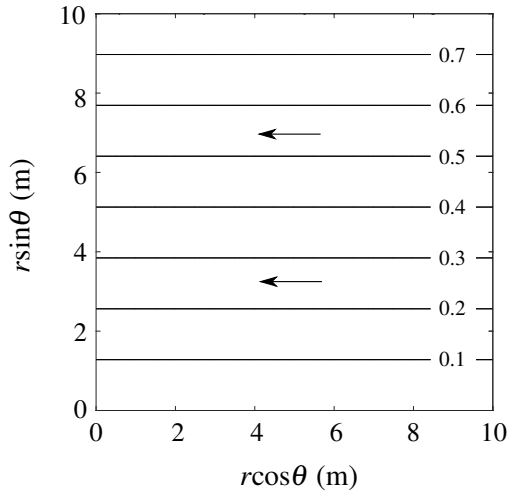

Fig. 2.5 Streamlines (solid lines) of the flow induced by a line plume with $B_0 = 0.028$ m^3s^{-3} (corresponding to a power input at the source of 1 kWm^{-1}). The induced flow is partially-confined at the level of the source at $\theta = 0$ by a horizontal boundary. A constant speed of 7.8×10^{-2} ms^{-1} is induced. Values of the stream function (m^2s^{-1}) corresponding to each streamline are overlain on each contour. Arrows indicate the direction of motion.

The flow induced by the line plume issuing vertically from a horizontal boundary is uniform and horizontal. The solution in table 2.1 is illustrated in figure 2.5 for a thermal plume in air, with source strength, B_0, corresponding to a power input of $P_c = B_0 c_h/(g e_c) =$ 1 $kW.m^{-1}$ (with c_h and e_c denoting the specific heat capacity and coefficient of thermal expansion, respectively). To add context, we select a power input typical of the plume flow rising from the top of a room convector (Quintiere, 1997, p. 60). Using the corresponding expression for speed in table 2.1, we identify that a constant speed $U = 7.8 \times 10^{-2}$ ms^{-1} is induced. No solution is derived for the flow induced by the unconfined line plume, as it is identified that in reality the plume flow at a large height has a significant effect on the flow near the source. Taylor (1961) highlights that this is an example of the inherent difficultly in devising two-dimensional models for plumes and their induced flows in an unconfined environment.

Figures 2.3, 2.4 and 2.5 highlight the significance of both the source conditions and confinement of the environment on the flow that is induced. Specifically, these properties have a pronounced effect on: the bulk shape of the induced flow; the velocities that are induced; and the location from which ambient fluid is drawn in. The influence of the source conditions provided motivation in this thesis to (i) devise diagnostics (in Chapter 3) to compare the line jet and line plume induced flows, and (ii) to assess the effect on the induced flow of an off-source input of buoyancy (in Chapter 5), and a combination of both buoyancy and momentum inputs (in different ratios) at the source (in Chapters 4 and 6).

2.3 Non-idealised plume induced flows

Thus far our focus has been on the flows induced by idealised line sources of momentum flux M_0 (i.e. the line jet) and buoyancy flux B_0 (i.e. the line plume). These induced flow models are unrepresentative of jet/plume flows with a source supply of fluid, i.e. with a non-zero source flux of volume Q_0. Therefore, in this section, we consider the general case of the flow induced by non-idealised plumes which have a source supply of all three fluxes, $Q_0 \neq 0$, $M_0 \neq 0$ and $B_0 \neq 0$. The non-idealised jet corresponds to the limiting case when $B_0 = 0$.

As briefly outlined in Chapter 1, a pure plume represents the equilibrium state when buoyancy and inertial forces in the plume are balanced for all heights. This occurs above idealised line sources of buoyancy, and also when forces are balanced at a (non-idealised) source with non-zero width (List, 1982). These two flows can be related, by viewing the latter as simply the flow above a line source located at some vertical distance below the source. We use this knowledge to represent the non-idealised pure plume, when modelling its induced flow, in the following section. Specifically, the non-idealised pure plume is modelled using a virtual line source of buoyancy located below the real source at $y = -y_{sc}$ (where 'sc' denotes 'source correction') (Hunt & Kaye, 2001). The induced flow solution derived below denotes a simple extension of the solution from Taylor (1958) in table 2.1. Whilst simple, this solution does not appear to have been documented before.

2.3.1 Pure plume induced flow solution

The virtual origin is located such that the fluxes Q_0, M_0 and B_0 at a non-idealised plume source are identical to the respective local fluxes Q, M and B above an idealised line source of buoyancy flux B_0. The local buoyancy flux B is invariant with height in a uniform environment. The local fluxes of volume and momentum above a line plume are given by Lee & Emmons (1961) in a self-similar form in terms of the source buoyancy flux and vertical coordinate, as

$$Q = c{B_0}^{1/3} y \quad \text{and} \quad M = c^{1/2}{B_0}^{2/3} y, \tag{2.11}$$

respectively, where the constant $c = 2{\alpha_p}^{2/3} = 2\varepsilon_p$ for Gaussian profiles of velocity w and buoyancy g' (see §A.1 in Appendix A). To identify the source correction y_{sc} for the pure plume, we equate (either of) the expressions in (2.11) to the corresponding source flux of the non-idealised pure plume, i.e. $Q = Q_0$ or $M = M_0$, and rearrange for the vertical coordinate to obtain

$$y = y_{sc} = \frac{Q_0}{c{B_0}^{1/3}} = \frac{M_0}{c^{1/2}{B_0}^{2/3}}. \tag{2.12}$$

Note that either of the fluxes (volume or momentum) can be used to determine the source correction in (2.12) owing to the local dependence between the fluxes Q, M and B (see §2.3.2). With the origin of the (global) induced flow plane polar coordinates (r,θ) located at the edge of the plume source at a flow cross-section, we represent the non-idealised pure plume using the line plume boundary condition in (2.6) with the addition of the source correction in (2.12), to give

$$\chi = \varepsilon_{\mathrm{p}} {B_0}^{1/3}(r+y_{\mathrm{sc}}) \quad \text{at} \quad \theta = \pi/2. \tag{2.13}$$

The corresponding boundary condition for the horizontal boundary represented using a streamline is

$$\chi = \varepsilon_{\mathrm{p}} {B_0}^{1/3} y_{\mathrm{sc}} \quad \text{at} \quad \theta = 0. \tag{2.14}$$

The value of the stream function in (2.14) is chosen so as to maintain continuity with the corresponding value at the source of the pure plume in (2.13). To solve for the induced flow we seek a solution to the Laplace equation (2.1) that satisfies the boundary conditions in (2.13) and (2.14). The general solution to Laplace's equation, derived using the method of separation of variables (see Chapter 5), takes the form

$$\chi(r,\theta) = (k_0 \ln r + l_0)(m_0\theta + n_0) + \sum_{\lambda=1}^{\infty} (k_\lambda r^{\lambda} + l_\lambda r^{-\lambda})[m_\lambda \cos(\lambda\theta) + n_\lambda \sin(\lambda\theta)], \tag{2.15}$$

for constant coefficients k_0, l_0, m_0, n_0, k_λ, l_λ, m_λ and n_λ. We match the general solution with the boundary conditions in (2.13) and (2.14). To satisfy the plume boundary condition we first set $\lambda = 1$ (and $l_\lambda = 0$) in order to match the exponent of the coordinate r with that in (2.13), and assign $k_\lambda n_\lambda = \varepsilon_{\mathrm{p}} {B_0}^{1/3}$ corresponding to the coefficient of the radial coordinate. To then represent the streamline boundary condition along $\theta = 0$ and simultaneously enforce the virtual origin correction in (2.13), the constant $n_0 l_0$ in (2.15) is equated to the value of the stream function corresponding to the streamline in (2.14) and the coefficients k_0, m_0, m_λ are set to zero. The resultant solution for the induced flow of the pure plume is

$$\chi = \varepsilon_{\mathrm{p}} {B_0}^{1/3}(r\sin\theta + y_{\mathrm{sc}}). \tag{2.16}$$

The solution in (2.16) predicts that the flow induced by the (non-idealised) pure plume is horizontal and has a constant speed, $U = \varepsilon_{\mathrm{p}} {B_0}^{1/3}$, throughout the domain. This speed is identical to that for the induced flow solution of the line plume in table 2.1.

2.3.2 Γ-centred approach

Non-pure plumes cannot be modelled accurately using a virtual source of buoyancy flux located below the source. These plumes have a force imbalance at their source, which is continuously reduced as the source input of buoyancy undertakes work with height. Thus, representing the non-pure plume flow using a virtual line source model would only be representative in the vertical limit. Consequently, we directly account for all three plume source fluxes, Q_0, M_0 and B_0, when formulating the non-pure plume boundary condition for the induced flow (in Chapters 4 and 6). The approach we adopt is discussed in the following.

To formulate the non-pure plume boundary condition, we introduce what we refer to hereinafter as the Γ-centred formulation, originally proposed in Hunt & Kaye (2005) to describe plumes above a circular source, and later by van den Bremer & Hunt (2014) to represent plumes above a slender slot. The approach is centred around defining a flow Richardson number (or flux balance parameter), defined in terms of the local fluxes, Q, M and B, and equivalently in terms of the local width b, and characteristic values of velocity w_m and buoyancy g'_m, as

$$\begin{aligned}\Gamma(y) &= \frac{1}{2^{3/2}\alpha}\frac{B(y)Q(y)^3}{M(y)^3} \\ &= \frac{\pi^{1/2}}{2^{1/2}\alpha}\frac{g'_\mathrm{m}(y)b(y)}{w_\mathrm{m}(y)^2}.\end{aligned} \tag{2.17}$$

This key dimensionless quantity governing the physics of the plume flow represents the local balance of the plume's buoyancy and inertial forces. The prefactors $(2^{3/2}\alpha)^{-1}$ and $\pi^{1/2}(2^{1/2}\alpha)^{-1}$ in (2.17) are specific to the Gaussian profiles adopted for buoyancy and vertical velocity (van den Bremer & Hunt, 2014). The characteristic values of velocity $w = w_\mathrm{m}$ and buoyancy $g' = g'_\mathrm{m}$ are chosen as the respective centre-line values. As will become evident, working with the plume Richardson number provides direct insight into the local plume dynamics, and further, enables one to assess the effect that the balance of the forces at the plume source, or locally, has on the induced flow in the environment.

The dynamics of a plume are dependent on its source Richardson number,

$$\Gamma(0) = \Gamma_0 = \frac{1}{2^{3/2}\alpha}\frac{B_0{Q_0}^3}{{M_0}^3}, \tag{2.18}$$

and can be characterised in terms of Γ_0 as pure ($\Gamma_0 = 1$), forced ($0 < \Gamma_0 < 1$) or lazy ($\Gamma_0 > 1$) (van den Bremer & Hunt, 2014). A jet corresponds to $\Gamma_0 = 0$. Based on this characterisation, forced and lazy plumes can be viewed as having a relative deficit and excess in buoyancy flux at their sources, respectively, (with identical source fluxes of volume and momentum)

compared to the pure plume. In contrast to the pure plume, which maintains its source Richardson number with height, i.e. $\Gamma = \Gamma_0 = 1$, the local value of Γ above the forced and lazy plumes locally varies and asymptotes to the equilibrium state of the pure plume, i.e. $\Gamma \to 1$ as $y \to \infty$ (see van den Bremer & Hunt (2014)).

Following van den Bremer & Hunt (2014), the Γ-centred formulation is based on recasting the plume conservation equations from Lee & Emmons (1961) where they are expressed in terms of the local fluxes Q, M and B. The equations are recast in terms of three dimensionless local parameters; the Richardson number Γ, the half-width

$$\bar{b} = \frac{b}{b_0} \tag{2.19}$$

and the centre-line velocity

$$\bar{w} = \frac{w_\mathrm{m}}{w_0}. \tag{2.20}$$

The recast system of ordinary differential equations (ODEs) take the form

$$\frac{d\Gamma}{d\zeta} = \frac{3\Gamma(1-\Gamma)}{\bar{b}}, \quad \frac{d\bar{b}}{d\zeta} = 2-\Gamma, \quad \frac{d\bar{w}}{d\zeta} = \frac{\bar{w}}{\bar{b}}(\Gamma-1), \tag{2.21}$$

where $\zeta = 2\alpha y/(\pi^{1/2} b_0)$ denotes the dimensionless (Gaussian) vertical coordinate (see Appendix B for derivation). The corresponding source conditions for the plume are

$$\Gamma = \Gamma_0, \quad \bar{b} = 1, \quad \bar{w} = 1 \ \text{ at } \ \zeta = 0. \tag{2.22}$$

The ODEs in (2.21) subject to (2.22) can be solved for $\bar{b}$ and $\bar{w}$ as a function of height (as they are in van den Bremer & Hunt (2014)), to determine the dimensionless volume flux $q = Q/Q_0 = \bar{b}\bar{w}$. This is equivalent to the dimensionless stream function

$$\Psi = \frac{\chi}{\chi_0}, \tag{2.23}$$

which we use to represent the non-idealised, non-pure plume boundary condition when developing our induced flow solutions in Chapters 4 and 6.

Evidently, using the recast equations in (2.21) provides greater direct physical insight into the plume flow and the associated local entrainment characteristics in comparison to working in terms of the fluxes Q, M and B. For instance, from the expression $\mathrm{d}\bar{b}/d\zeta$ in (2.21), we can identify that the plume will locally contract when it is sufficiently lazy, i.e. for $\Gamma > 2$, and from, $d\bar{w}/d\zeta$, that the pure plume ($\Gamma = \Gamma_0 = 1$) (modelled in §2.3.1) maintains a constant velocity with height, i.e. $d\bar{w}/d\zeta = 0$.

2.3.3 Exploiting complex analysis

The boundary value problem governing the flow induced by a non-pure plume does not readily lend itself to standard analytical solution techniques, such as the method of separation of variables. This is on account of the complexity of the plume boundary condition, and in the case of the contracting lazy plume ($\Gamma_0 > 2$) considered in Chapter 4, the geometry of the plume perimeter along which the boundary condition is applied. Instead, we appeal to the theory of functions of a complex variable to derive an analytical solution for the induced flow. Complex variable theory is a powerful tool for solving two-dimensional potential flow problems, and has been widely applied to solve problems across fluid mechanics. Some examples include the classic inviscid flow past an aerofoil (as shown in Batchelor (1969)), flows with free surfaces (e.g. Eggers & Smith (2010)) and biological fluid flows (e.g. Setchi (2012)).

To utilise theorems from complex analysis in a physical scenario, one must begin by reformulating the original boundary value problem, which in our case represents the induced flow, in the complex domain. This is achieved by directly reinterpreting real coordinates as components of a complex coordinate, for instance, viewing the plane polar coordinates (r, θ), used to develop the induced flow solutions in table 2.1, as part of the complex coordinate $z = re^{i\theta}$ (where $i = (-1)^{1/2}$ denotes the imaginary unit). Thus, the induced flow now corresponds to a region in the complex plane. Cauchy's integral theorem (Morse & Feshbach, 1953) states that any property (governed by the Laplace equation) can be determined in a region internal to a closed boundary, subject to specifying the values of the property along the boundary. Derived from Cauchy's theorem and formulated specifically in the upper-half complex plane, Poisson's theorem (2.27) gives a solution to Laplace's equation subject to specifying boundary conditions along the real-axis. To exploit Poisson's theorem, a complex function must be determined that maps from the region of the induced flow to the upper-half plane, and crucially, the function must be conformal, i.e. preserve the property of the Laplace equation (Paliouras & Meadows, 1990). In this way, one can identify the corresponding locations of the boundary conditions of the induced flow along the real axis of the upper-half plane. The boundary conditions can then be input into Poisson's theorem between specified limits, which correspond to the locations along the real axis where the boundary conditions are applied. A unique solution is thus identified for the governing boundary value problem in the upper-half plane. To obtain the solution in the original domain of the induced flow, one must subsequently apply the inverse of the original conformal mapping function to the coordinates in the upper-half plane. We apply the aforementioned technique to develop the solution for the flow induced by the contracting lazy plume and forced plume in Chapters 4 and 6, respectively. A novel mapping function is developed to map between the induced flow

region of the lazy plume, bounded by a contracting then expanding (curved) plume perimeter, and the upper-half plane.

To readers unfamiliar with the approach outlined above, a simple example is presented below to demonstrate its application. Consider a metal sheet (with sides of infinite length), that is uniformly heated along one edge and cooled along a perpendicular edge at constant temperatures. The temperature difference between the two edges, given by ΔT, is independent of time. The temperature distribution within the plate is well-known to be described by the heat equation (see Riley et al. (2006)), which in the steady-state reduces to the Laplace equation. Working with the variable of temperature relative to the cooled edge, u, for convenience, we define a boundary value problem for the steady-state (relative) temperature in the metal plate as governed by the Laplace equation, $\nabla^2 u = 0$, subject to the boundary conditions, $u = 0$, at the cooled edge, and $u = \Delta T$ along the heated edge.

To solve the boundary value problem, we begin by viewing the metal plate as the shaded region in the complex W-plane shown in figure 2.6, with the heated and cooled edges of the plate aligned with the vertical and horizontal axes, respectively. To utilise Poisson's theorem we use the complex function,

$$z = \omega^2 \tag{2.24}$$

(see Appendix C for formal derivation), defined in terms of the complex coordinates z and ω in the Z- and W-planes, respectively. This function maps from the quadrant in the W-plane (in which the problem is originally formulated) to the upper-half Z-plane illustrated in figure 2.6. This function maintains the Laplacian property as it is independent of the conjugate of the complex coordinate $\bar{\omega}$ (Morse & Feshbach, 1953). To gain insight into the mechanics of the mapping, we express the mapping in its polar form as

$$z = \omega^2 = r^2 e^{i2\theta}. \tag{2.25}$$

This indicates that the function uniquely maps the complex coordinates (r, θ) to the coordinates $(r^2, 2\theta)$. Here, the argument, which denotes the interior angle between the vertices, is doubled, and thus the perpendicular edges of the plate are mapped to the real axis. Specifically, the heated edge corresponds to $Re(z) < 0$, and the cooled edge corresponds to $Re(z) > 0$, along the real axis (where '$Re()$' denotes 'the real coordinate of'). The corresponding inverse mapping function (from the Z-plane to the W-plane) can be straightforwardly identified from the forward mapping in (2.24) as

$$\omega = z^{1/2}. \tag{2.26}$$

Having identified the forward (2.24) and inverse (2.26) mappings, and thereby the locations along the real axis of the upper-half plane where the boundary conditions are

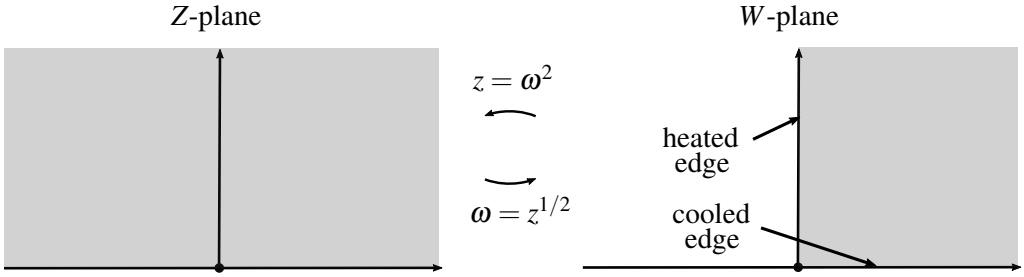

Fig. 2.6 The forward mapping, $z(\omega) = \omega^2$, and corresponding inverse mapping, $\omega(z) = z^{1/2}$, between the shaded regions of a quadrant in the W-plane and the upper-half Z-plane.

applied, we can utilise Poisson's theorem to derive a solution to the governing boundary value problem. Defining $z = \eta + i\xi$, Poisson's theorem (Paliouras & Meadows, 1990) is stated in the upper-half plane as

$$u(\eta,\xi) = \frac{\xi}{\pi}\int_{-\infty}^{\infty} \frac{u(\tau,0)}{(\eta-\tau)^2+\xi^2}\, d\tau. \tag{2.27}$$

The real-valued input function $u(\tau,0)$ corresponds to the boundary condition along the real axis. This function must be specified and bounded for all values of τ, though, it need not be continuous. It is expressed as a function of the dummy variable τ, which can be taken to be equivalent to the real coordinate η in the upper-half plane. The location along the real-axis where the boundary condition is applied is specified by the limits of the integral in (2.27). In our example there are two boundary conditions, corresponding to $u = \Delta T$ along $\eta < 0$, and to $u = 0$ along $\eta > 0$ on the real-axis. Consequently, we divide Poisson's theorem into two integrals to account for each of the boundary conditions, and derive the result

$$\begin{aligned} u(\eta,\xi) &= \frac{\xi}{\pi}\int_{-\infty}^{0} \frac{\Delta T}{(\eta-\tau)^2+\xi^2} d\tau + \frac{\xi}{\pi}\int_{0}^{\infty} \frac{0}{(\eta-\tau)^2+\xi^2} d\tau \\ &= \frac{\Delta T}{\pi}\tan^{-1}\left(\frac{\xi}{\eta}\right) \\ &= \frac{\Delta T}{\pi}\theta_Z, \end{aligned} \tag{2.28}$$

in the upper-half Z-plane. In this problem the second integral, corresponding to the boundary condition, $u = 0$, is zero. Note that in (2.28) the term, $\theta_Z \equiv \tan^{-1}(\xi/\eta)$, corresponds to the angular coordinate taken anti-clockwise from the (positive) real axis in the Z-plane. Finally, we employ the inverse mapping (2.26) to map the solution (2.28) back to the original W-plane of the induced flow. To apply the inverse mapping, we map the coordinates from the Z-plane,

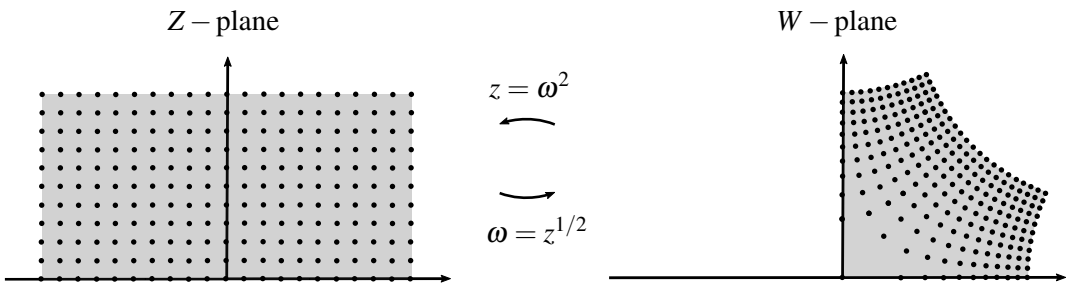

Fig. 2.7 The rectangular grid in the Z-plane and curvilinear grid in W-plane between which the functions $z=\omega^2$ and $\omega=z^{1/2}$ map.

or equivalently, express θ_Z as a function of θ, i.e. $\theta_Z=2\theta$, and substitute into (2.28) to give

$$u=\frac{2\Delta T}{\pi}\theta. \tag{2.29}$$

The solution in (2.29) indicates that the temperature of the metal plate is constant along lines of constant θ, and increases linearly with the angle θ from the cool edge (along $\theta=0$) to the hot edge (along $\theta=\pi/2$).

Evaluating Poisson's integral numerically

In our example of the temperature distribution across a metal sheet, the integrals in (2.28), which result from the application of Poisson's theorem, were straightforwardly evaluated. The corresponding integrals devised to model the flows induced by the lazy and forced plumes in Chapters 4 and 6, respectively, cannot be readily evaluated. This is owing to the complexity of the plume boundary condition that is input into Poisson's theorem. In order to plot the induced flows, we adopt a numerical approach; numerically evaluating the integral derived using Poisson's theorem in the Z-plane, and then applying the inverse conformal map to discrete points. A key issue when applying this approach, associated with the conformal mapping, is evident from the illustration in figure 2.6, which correspond to the domains considered in figure 2.6. Specifically, the plot indicates that the (inverse) mapping stretches and deforms the rectangular grid in the upper-half Z-plane into a curvilinear grid in the W-plane. As a consequence, the evenly distributed rectangular grid is mapped to an unevenly distributed grid in the W-plane, where crucially, the region in the vicinity of the coordinate origin contains a sparse distribution of grid points. With less grid points in this region, a plot of the solution will have a lower accuracy here. This phenomenon is widely referred to as 'crowding' (Driscoll & Trefethen (2002)), and is addressed when plotting the induced flow

solutions in Chapters 4 and 6.

From the previous discussion, it is evident that Poisson's theorem and conformal maps provide a useful tool for solving (two-dimensional) boundary value problems governed by the Laplace equation. Crucially, the method can be used to derive solutions in situations where standard solution techniques are unsuccessful. This includes problems containing non-standard geometries with challenging boundary conditions. We exploit these features of the method to tackle the challenges associated with modelling the non-pure plume induced flows in Chapters 4 and 6.

2.4 Summary

This chapter commenced with an outline of the general modelling approach taken and solutions derived in Taylor (1958) for the flows induced by the idealised line jet and line plume. The solutions highlighted the significance of the flow source conditions on the induced flow. This provided us with motivation to consider the effect that non-idealised flows, driven by source fluxes of volume, momentum and buoyancy, have on their environment. We developed the solution for the flow induced by a non-idealised pure plume in this chapter, as a straightforward extension of Taylor's work. In the subsequent chapters we develop induced flow solutions for the non-pure plumes issuing from a horizontal slot and developing following an off-source vertical supply of buoyancy. The theory of functions of a complex variable, which was outlined towards the end of this chapter, provides a useful tool for modelling, as highlighted in the example of the heated plate, and will prove instrumental in determining the flows induced by non-pure plumes above horizontal sources.

Chapter 3

Comparative diagnostics

In this chapter we compare the influence that the source conditions of the idealised jet and idealised plume have on their environments. Specifically, we compare the effect of driving a flow by a finite source flux of momentum M_0 with that by a finite source flux of buoyancy B_0. We propose two diagnostics to make the comparison, herein referred to as the 'Velocity Ratio' and 'Bounding Locus' methods. These diagnostics use the induced flow as a means of identifying regions in the environment where the jet and plume each have a stronger effect.

One of the direct applications of this work is to using induced flows to move air in rooms. In this context, the comparative diagnostics provide a means, in a given scenario, to determine, for instance, whether blowing or heating should be used from a localised source to move a patch of fluid at a specified location.

We begin with an outline of the 'Velocity Ratio' and 'Bounding Locus' diagnostics in §3.1 and §3.2, respectively, before applying the diagnostics to compare the flows induced by the line jet and line plume in §3.3. The diagnostics are applied using analytical models in this chapter, however, in general, the diagnostics can also be applied using numerical or experimental data. Conclusions are drawn in §3.4.

3.1 'Velocity Ratio' diagnostic

The 'Velocity Ratio' diagnostic is a measure of the relative influence of the jet and plume on their environments based on a direct comparison of the flow speeds they induce. The diagnostic is applied by dividing the flow speeds induced by one flow by that of the other at every spatial location across the domain. This enables a contour to be defined along which the fraction — the velocity ratio — takes a unit value, corresponding to where the speeds induced by each of the flows is equal. We refer to this as the 'unit' contour, and it separates

regions of the induced flow where the jet and plume are 'dominant', i.e. where the flow speeds induced by each of the flows is greater.

3.2 'Bounding Locus' diagnostic

It can be difficult and sometimes impractical to apply the 'Velocity Ratio' diagnostic described in §3.1 directly in an application, as there is a requirement to predetermine the speeds across the induced flow domains. In response to this difficulty, we propose an alternative, more practical method which we refer to as the 'Bounding Locus' diagnostic.

The 'Bounding Locus' diagnostic is based on introducing a passive, neutrally-buoyant tracer from a line source (or point source in the plane), with a fixed source flux of volume, into each induced flow. On moving the tracer source around each domain, a locus can be defined corresponding to the marginal locations at which the tracer is able/unable to cross a small fixed distance from its source. Equivalently, the locus corresponds to the position at which speeds in the induced flow match those of the outflow from the line source at a given distance from the source. Once a separate locus is identified for each induced flow, the horizontal distance between the vertical axis and locus is determined at each height. By taking a ratio of these lengths, we identify heights at which the ratio is above and below unity, and thus heights over which each flow has a stronger influence.

The method, as described above, fails when applied to the unique scenario of an induced flow with constant speed (as in §3.3). In this case, use of the current method will result in a locus being defined either along the vertical axis or else at an infinite extent away. To overcome this shortcoming, we propose applying a modification to the diagnostic. Specifically, we propose varying the distance from the source of the tracer at which crossing is evaluated in the uniform induced flow, until we attain the marginal state when the tracer crosses. This modification is straightforward to implement in practice, and provides us with an indication of the strength of the uniform induced flow. The modified distance can then be utilised to evaluate the locus in the other induced flow, which enables the relative strengths of the two induced flows to be assessed.

3.3 Application of diagnostics

In this section we apply the diagnostics to compare the effects that the line jet and line plume have on their surrounding environments. Prior to applying the diagnostics, for convenience, we restate the analytical solutions for the induced flows of the line jet and line plume issuing from a horizontal boundary (as detailed in Chapter 2). The induced flow solution for the line

jet, in terms of the stream function χ, is

$$\chi = \chi_{\mathrm{j}} = \left(\frac{3}{2\sigma}\right)^{1/2} {M_0}^{1/2} r^{1/2} \sin\left(\frac{\theta}{2}\right), \tag{3.1}$$

with a corresponding speed

$$U = U_{\mathrm{j}} = \left(\frac{3}{8\sigma}\right)^{1/2} {M_0}^{1/2} r^{-1/2}. \tag{3.2}$$

The induced flow solution for the line plume is

$$\chi = \chi_{\mathrm{p}} = {\alpha_{\mathrm{p}}}^{2/3} {B_0}^{1/3} r \sin\theta, \tag{3.3}$$

with a corresponding speed

$$U = U_{\mathrm{p}} = {\alpha_{\mathrm{p}}}^{2/3} {B_0}^{1/3}. \tag{3.4}$$

Solutions (3.1) – (3.4) are illustrated in figures 2.3 and 2.5 in Chapter 2.

3.3.1 'Velocity Ratio' application

To apply the 'Velocity Ratio' diagnostic, we divide the induced flow speed in (3.4) by that in (3.2), to obtain the fraction

$$\frac{U_{\mathrm{p}}}{U_{\mathrm{j}}} = \left(\frac{8\sigma}{3}\right)^{1/2} {\alpha_{\mathrm{p}}}^{2/3} {B_0}^{1/3} {M_0}^{-1/2} r^{1/2}. \tag{3.5}$$

Figure 3.1 illustrates the 'unit' contour ($U_{\mathrm{p}}/U_{\mathrm{j}} = 1$) when $M_0 = 1.087\mathrm{m}^3\mathrm{s}^{-2}$, $B_0 = 0.028\mathrm{m}^3\mathrm{s}^{-3}$, $\sigma = 7.67$ and $\alpha_{\mathrm{p}} = 0.13$ (values used to plot figures 2.3 and 2.5). In this example, the contour, which corresponds to the location where the speeds induced by the jet are identical to that of the plume, is characterised by a quarter circle with radius $r_{\mathrm{u}} = 8.75$ m. The jet induces a stronger flow for $r < r_{\mathrm{u}}$, as the jet's source momentum flux is large in comparison to the momentum flux induced by the plume's buoyancy in this near-source region. For $r > r_{\mathrm{u}}$, the momentum flux induced by the plume's buoyancy is sufficient that the speed it induces exceeds that of the flow induced by the jet. This demarcation into two regions has implications for the movement of air in a large room for instance, indicating where localised forcing and heating at the source (with given strengths) provide the more effective means to move air.

Figure 3.2 (a) and (b) illustrate the shift to the 'unit' contour in figure 3.1 achieved upon doubling the source strengths of the line jet and line plume, respectively. Increasing the strength of the jet (and maintaining the strength of the plume) shifts the 'unit' contour

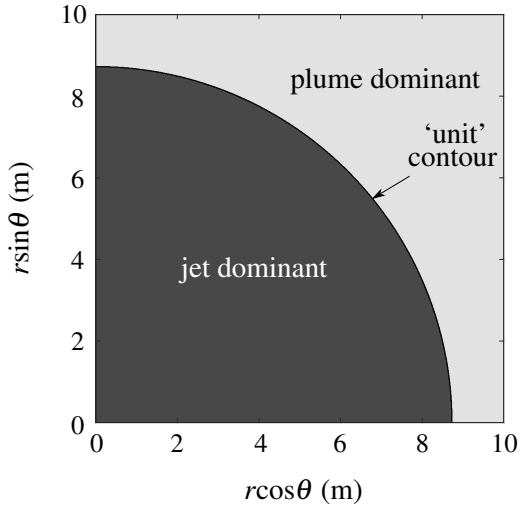

Fig. 3.1 'Unit' contour separating the jet dominant region (where $U_\mathrm{p}/U_\mathrm{j} < 1$) from the plume dominant region (where $U_\mathrm{p}/U_\mathrm{j} > 1$) in the induced flow. The jet and plume source strengths correspond to those used to plot figures 2.2 and 2.4.

radially outwards, resulting in the jet having a stronger influence in the environment. A larger strength of plume (with a maintained jet strength) has the opposing effect of moving the contour radially inwards towards the source, in which case the plume has a stronger influence in the environment. Interestingly, the magnitude of the 'unit' contour shifts differ between the plots. The jet dominant region doubles in radius in figure 3.2 (a), whilst the radius in figure 3.2 (b) reduces by a factor $2^{2/3}$; failing to (equivalently) reach a radius corresponding to half the original 'unit' contour. This effect is discussed further later. Thus, modifying the source strength of the jet has a more pronounced effect on the environment.

A natural question that arises on viewing figure 3.1 is whether the radius of the 'unit' contour, r_u, can be directly obtained using the bulk flow properties of the jet and plume. To answer this, we consider the notion of a 'jet-length' L_j ($\propto M_0/{B_0}^{2/3}$). This characteristic length, originally introduced when modelling flows with fluxes of buoyancy and momentum at their source by Morton (1959), is a representative scale over which the jet's source momentum flux is significant compared with the effect of the plume's source buoyancy flux — it is normally used to describe the vertical distance over which the flow can be regarded as 'jet-like'. The scale can be determined by equating the fluxes of volume driven by the line plume and line jet, and rearranging for the vertical coordinate, i.e.

$$Q_\mathrm{j} = \left(\frac{3}{\sigma}\right)^{1/2} {M_0}^{1/2} y^{1/2} = Q_\mathrm{p} = 2{\alpha_\mathrm{p}}^{2/3} {B_0}^{1/3} y \quad \Rightarrow \quad y = L_\mathrm{j} = \frac{3}{4\sigma {\alpha_\mathrm{p}}^{4/3}} \frac{M_0}{{B_0}^{2/3}}. \tag{3.6}$$

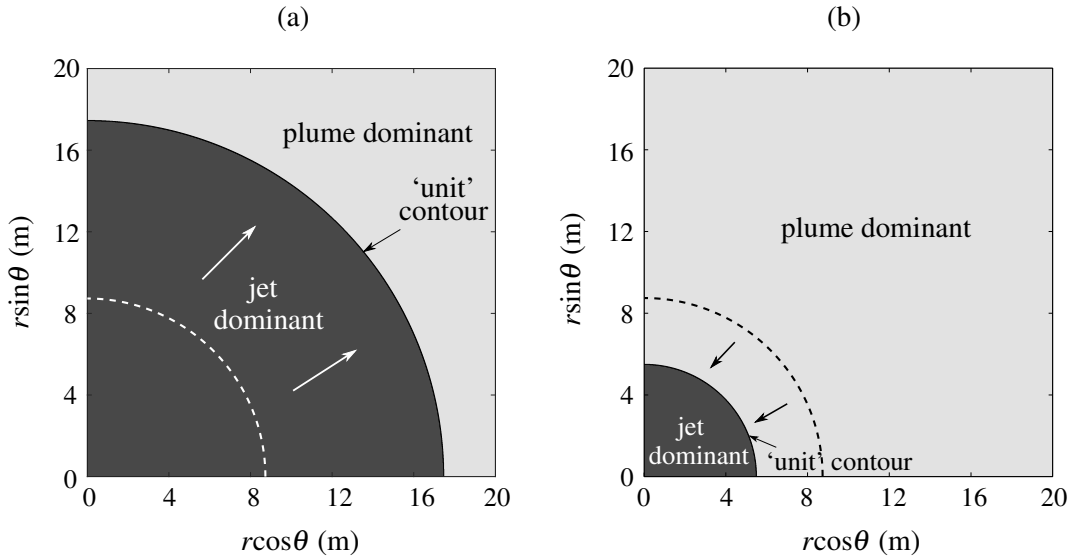

Fig. 3.2 The shift to the 'unit' contour in figure 3.1 achieved upon doubling the source strength (a) of the jet to $2M_0$, and (b) of the plume to $2B_0$. The dashed line corresponds to the original 'unit' contour in figure 3.1 and the arrows indicate the direction of the shifts.

As we seek to compare induced flows, we choose to define the length scale by equating the entrained velocities instead. There is an inherent assumption that the entrained flow at the jet/plume perimeter is purely horizontal. In our application, the jet induced flow, illustrated in figure 2.3, clearly has a vertical component. With this in mind, we modify our earlier definition of the 'jet length'. Specifically, we account for the inclination of the induced flow when equating the entrained velocities by considering the horizontal component of the induced flows, before rearranging for the vertical coordinate, to give the radius of the 'unit' contour

$$r_{\mathrm{u}} = \frac{3M_0}{16\sigma {B_0}^{2/3} {\alpha_{\mathrm{p}}}^{4/3}} \frac{\cos^2\theta_{\mathrm{p}}}{\cos^2\theta_{\mathrm{j}}} \tag{3.7}$$

(see Appendix D for derivation). In (3.7), θ_{j} and θ_{p} correspond to the respective angles that the jet and plume induced flow streamlines make with the horizontal at the vertical axis. The inclination angles are taken as positive in the clockwise direction so as to maintain consistency with subsequent chapters. The inclinations, which are invariant with height, take a value of $\theta_{\mathrm{j}} = -\pi/4$ and $\theta_{\mathrm{p}} = 0$ for the line jet and line plume, respectively (see figures 2.3 and 2.5). Inputting their values into expression (3.7), along with the instances of M_0, B_0, σ and α_{p} used to plot figure 3.1, we attain $r_{\mathrm{u}} = 8.75$ m as before.

The dependency of the 'unit' contour's location on specific values of M_0 and B_0 can be removed by scaling the axes of figure 3.1 on $M_0/{B_0}^{2/3}$. Note that the exponents of the source fluxes in this scaling are consistent with the magnitude of the shifts to the 'unit' contour in

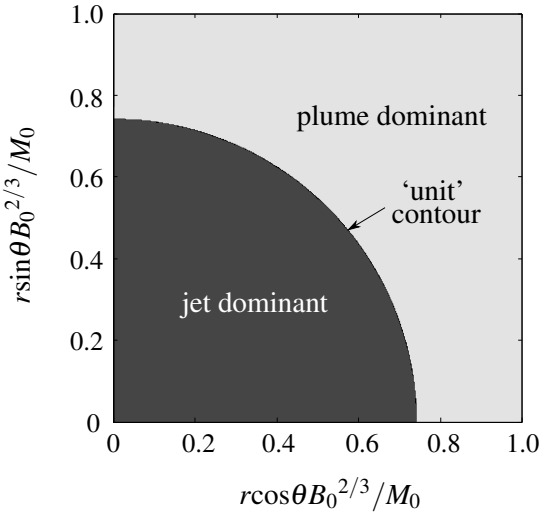

Fig. 3.3 Universal plot showing dimensionless equivalent of figures 3.1 and 3.2, with the axes scaled on the jet-length, $M_0/{B_0}^{2/3}$, to remove dependency on the choice of values of the governing fluxes M_0 and B_0.

figure 3.2 upon doubling the source strengths of the jet and plume. The resulting scaled plot, which we refer to as the 'universal' plot, is illustrated in figure 3.3. The radius of the 'unit' contour in this figure can be straightforwardly determined using expression (3.7) as

$$\frac{r_{\mathrm{u}}}{(M_0/{B_0}^{2/3})} = \frac{3}{16\sigma{\alpha_{\mathrm{p}}}^{4/3}}\frac{\cos^2\theta_{\mathrm{p}}}{\cos^2\theta_{\mathrm{j}}} = 0.74. \tag{3.8}$$

This dimensionless expression can be utilised directly to identify the location of the 'unit' contour (in dimensional space) corresponding to any chosen values of M_0 and B_0. This is an enhanced form of the diagnostic, as there is no longer the requirement to reimplement the method upon selecting different values of the source strengths.

3.3.2 'Bounding Locus' application

We introduce a line source issuing a (passive) neutrally-buoyant tracer at a fixed rate, i.e. with a fixed flux of volume, Q_{t} (where the subscript '$(\cdot)_{\mathrm{t}}$' refers to tracer), separately into the flows induced by the line jet and line plume. To account for the horizontal boundary (at the level of the source), we superpose a complementary image source (with an identical source strength to the original). The image source is maintained equidistant from and on the opposing side of the boundary, as illustrated in the schematic in figure 3.4. The flow speed

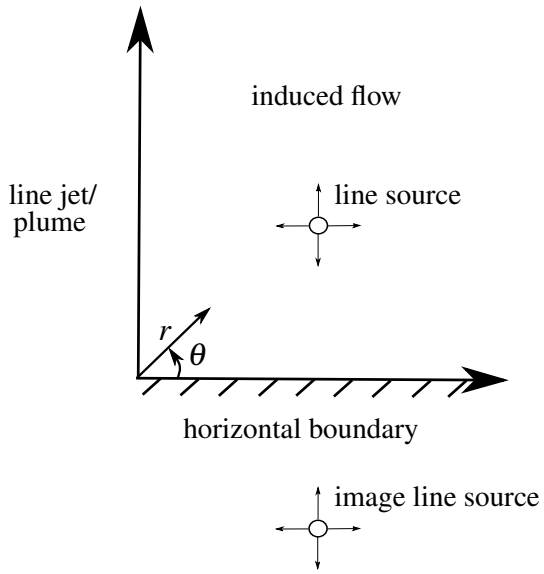

Fig. 3.4 Schematic to aid in visualising the 'Bounding Locus' diagnostic. A line source of tracer is positioned at $r = r_0$ in the induced flow, and a complementary image source included to ensure zero flux across the horizontal boundary.

induced by the tracer is

$$U_{\mathrm{t}} = \frac{Q_{\mathrm{t}}}{2\pi}\left(\frac{1}{r_{\mathrm{t}}} + \frac{1}{r_{\mathrm{it}}}\right), \tag{3.9}$$

where

$$r_{\mathrm{t}} = \left((r\cos\theta - r_0\cos\theta_0)^2 + (r\sin\theta - r_0\sin\theta_0)^2\right)^{1/2} \tag{3.10}$$

and

$$r_{\mathrm{it}} = \left((r\cos\theta - r_0\cos\theta_0)^2 + (r\sin\theta + r_0\sin\theta_0)^2\right)^{1/2} \tag{3.11}$$

denote the local radial coordinates which originate at the line and image sources, respectively. The coordinates (r, θ) denote the global induced flow coordinates, and the subscript '$(\cdot)_0$' corresponds to the position of the line source. Exploiting the linear property of Laplace's equation, we superpose the speed in (3.9) with the (negative value of the) flow speeds induced by the line jet from (3.2) and line plume from (3.4), to give

$$U = U_{\mathrm{t}} - U_{\mathrm{j}} \tag{3.12}$$

and

$$U = U_{\mathrm{t}} - U_{\mathrm{p}}. \tag{3.13}$$

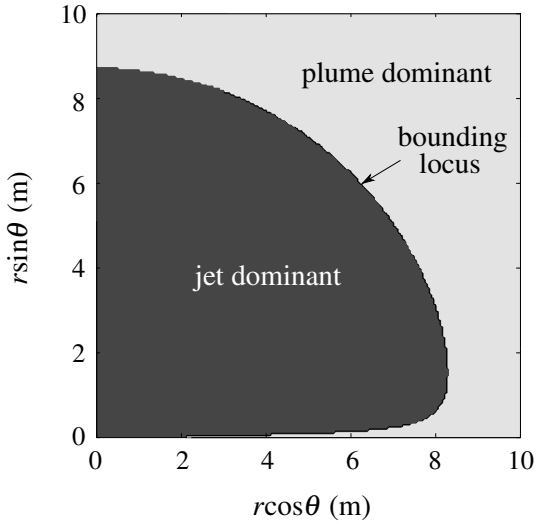

Fig. 3.5 Locus separating regions of the induced flow where the line jet and line plume have a 'dominant' influence. The jet and plume source conditions correspond to those used in figure 3.1, and for this example the line source issues a tracer volume flux $Q_t = 0.0245$ m^2s^{-1}.

Expressions (3.12) and (3.13) can be used to identify two separate loci along which the speeds are zero. This would define the marginal location in the induced flow at which a tracer issuing from the line source is unable to cross the locus.

Noting that the line plume induces an inflow with a constant speed, we apply the modified version of the 'Bounding Locus' diagnostic (outlined in §3.2). As an example, we place the passive tracer with a chosen source strength, $Q_t = 0.0245$ m^2s^{-1}, into the flow induced by a plume with $B_0 = 0.028$ m^3s^{-3} (corresponding to the source strength used to apply the 'Velocity Ratio' diagnostic in §3.1). Using expression (3.13), we identify the marginal distance from the tracer's source at which the tracer fails to cross, i.e. where $U = 0$. This gives a radius of $r_t = 5 \times 10^{-2}$ m. Adopting this value of the radius to evaluate (3.12) for the jet induced flow with $M_0 = 1.087$ m^3s^{-2} (corresponding to the strength used in §3.3.1), we output the locus in figure 3.5.

It is evident that away from the horizontal boundary, the locus illustrated in figure 3.5 has an identical radius to that output via the 'Velocity Ratio' diagnostic in figure 3.1, i.e. of $r_u =$ 8.75 m. Close to the horizontal boundary, however, the locus curves (sharply) inwards. To ensure that no flow crosses the horizontal boundary, the radial release of the passive tracer in this region is redirected along a horizontal path. This anisotropy in the outflow speed can effectively be viewed as an increase in the 'strength' of the line source. The net effect is a locus defined closer to the vertical axis near the boundary.

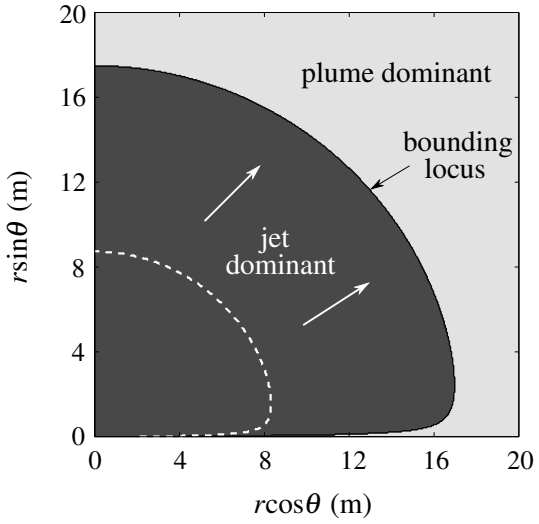

Fig. 3.6 The shift in the locus in figure 3.5 achieved upon doubling the source strength of the jet to $2M_0$. The dashed line corresponds to the original locus in figure 3.5 and the arrows indicate the direction of the shift.

The locus in figure 3.5 is shifted by a change to the source strengths of the jet and/or plume. For instance, in figure 3.6 we have doubled the jet momentum flux M_0, which, identical to figure 3.2 (a) output using the 'Velocity Ratio' diagnostic, has resulted in the locus being shifted to twice the original radius. The outward shift is a consequence of the source of the tracer needing to be moved outward in order for its outflow speed to match the larger magnitude of the jet induced flow speed. Similar to the 'universal' plot in figure 3.3, the dependency of the locus on the source fluxes can be removed by scaling on the 'jet length' L_j.

An alternative, arguably less practical proposal to introducing a passive tracer (in the form of a line source) into the induced flow, is to introduce a line sink (with source strength $-Q_\mathrm{t}$). By drawing fluid inward and removing it at a constant rate, the line sink induces a flow in the opposite (radial) direction to the line source. In this scenario, the locus can be interpreted as the marginal position inside of which the sink is able to capture fluid from. Despite the contrasting induced flow pattern that results and the different physical interpretation of the locus, interestingly, use of a line sink leads to an identical locus to that output in figure 3.5.

3.4 Conclusions

Both the 'Velocity Ratio' and 'Bounding Locus' diagnostics indicate that the source supply of momentum flux, M_0, has a pronounced effect on the surrounding environment close to

the source, relative to a source supply of buoyancy flux B_0. The source input of buoyancy flux continuously undertakes work with height, inducing an increasing local momentum flux, which leads to a stronger influence in the environment beyond a radial distance (specified by the contour/locus) from the source. Moreover, we identify that changing the source strength of the jet has a more pronounced effect on the environment in comparison to changing the plume strength. These results have implications, for instance, in applications that explicitly use flows from localised sources to move/control air in the ambient; identifying the more effective means by which to influence a patch of fluid at a given location. A governing length scale defined in terms of the source fluxes, referred to in the literature as a 'jet-length', which we have modified to include information on the inclination of the induced flow streamlines at jet/plume perimeter, enables the location of the contour/locus in the diagnostics separating the two 'dominant' regions in the environment to be directly identified.

Inspired by the effects that the competing fluxes of buoyancy and momentum from localised sources have on their environments, we consider non-idealised flows with both momentum and buoyancy fluxes in subsequent chapters. The flow induced by these more complex sources has not been considered previously. We model the induced flow corresponding to a broad range of non-idealised source conditions, beginning with the flow induced by the contracting lazy plume in the following chapter.

Chapter 4

Flows induced by contracting lazy plumes

In this chapter we investigate the flow induced by the contracting lazy plume above a slender horizontal source. A lazy plume typically issues from a large area source with a low source momentum flux. With reference to the source Richardson number (2.18), for a lazy plume $\Gamma_0 > 1$, and hence it may equivalently be regarded as a source excess of buoyancy flux compared to the pure plume. We focus on modelling the induced flow of the lazy plume in the near-field vicinity of the source. Here, the plume exhibits a near-source contraction when it is sufficiently lazy, due to a strong buoyancy-induced acceleration, before proceeding to expand with a close to pure plume-like linear growth rate at greater heights. The flow contraction can be seen in the (inverted) shadowgraph image in figure 4.1 of a lazy saline plume (above a circular source) with $\Gamma_0 \approx 1500$ (where we recall the subscript '0' refers to the source value). Note that a visualisation of the lazy plume above a circular source is presented, as no visualisations of the lazy plume above a narrow slot are currently available in the literature. The plot (right) in figure 4.1 depicts the curved plume perimeter (observed in the shadowgraph image), which has been output for lazy plumes above a slender horizontal slot with $\Gamma_0 = \{10, 100, 1500\}$ upon solving (4.7) and (4.8) in §4.1.1. Also included is a schematic of streamlines in the corresponding induced flow, with arrows superimposed to indicate the general flow direction.

Lazy plumes are markedly more complex than their pure counterparts (considered in Chapter 2), and insights into these flows have only more recently been made. Hunt & Kaye (2005) proposed and applied their Γ-centred formulation (outlined in §2.3.2), recasting the plume conservation equations from Morton et al. (1956), to gain insight into the flow dynamics of the lazy plume above the horizontal circular source. With this approach they obtained analytic solutions in the near-field contracting region. van den Bremer & Hunt

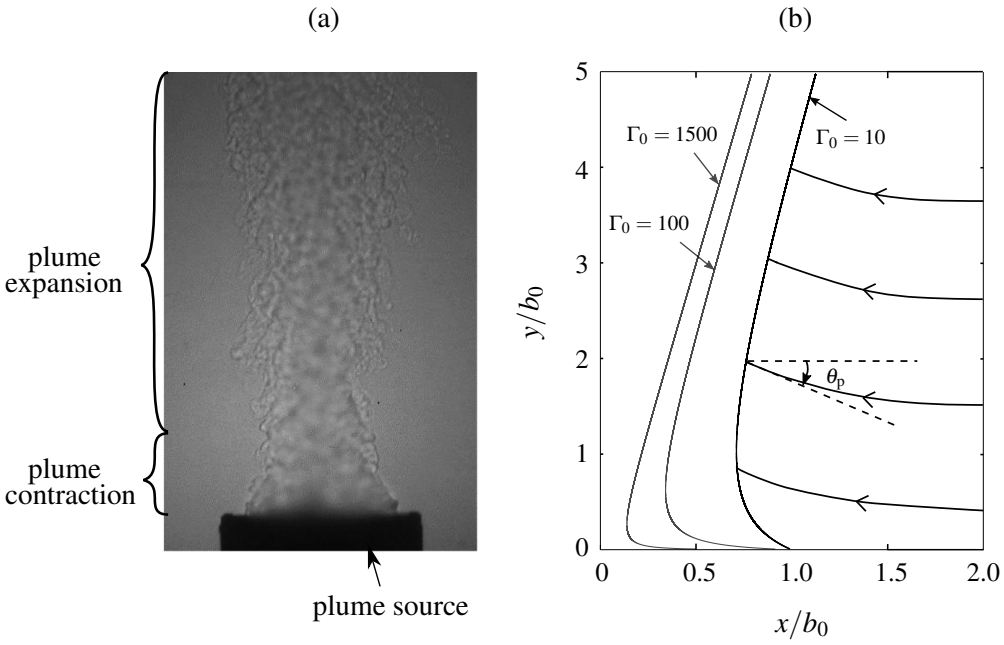

Fig. 4.1 (a) An inverted shadowgraph image from Hunt & van den Bremer (2011) of a lazy saline plume with source Richardson number $\Gamma_0 \approx 1500$ above a circular source with diameter 15×10^{-2} m. (b) The perimeter of the plume above a long and thin slot for source conditions corresponding to $\Gamma_0 = \{10,\ 100,\ 1500\}$, with the coordinate axes scaled on the plume source half-width b_0. A schematic of the induced flow streamlines has been superimposed in the region external to the plume with $\Gamma_0 = 10$, and the overlying arrows indicate the general direction of flow. The inclination of a given streamline at the plume perimeter is represented using the angular coordinate θ_p.

(2014) later reapplied the approach to model the lazy plume above a slender horizontal slot, and further, used 'scale diagrams' (cf. Morton & Middleton (1973)) in their analysis to locate points of interest within the plume, e.g. the neck height, as a function of Γ_0. To our knowledge, Pham et al. (2005) and Kaye & Hunt (2009) have conducted the only experimental campaigns on lazy contracting plume entrainment, focussing specifically on the lazy plume above a circular source. Based on their empirical results, Carlotti & Hunt (2017) recently devised a new entrainment model (presented in §7.3 in Chapter 7), as an alternative to the classic constant α model (A.8) introduced by Taylor (1945), in order to provide an improved description of lazy plume entrainment. However, for reasons outlined in §7.3, we choose to adopt the constant α model when formulating the induced flow solution for the lazy plume in this chapter.

Analogous to Taylor's (1958) approach to model the flow induced by the line jet and line plume (see Chapter 2), the effect of entrainment into the contracting plume on the environment is represented using a vertical distribution of line sinks. However, modelling the

sinks along a vertical line, which is readily justified when considering slender straight-sided plumes, such as the pure plume, becomes questionable in the current application owing to the strong curvature of the plume perimeter and the near-source contraction (figure 4.1). Crucially, part of the induced flow region is located directly above the source of the contracting lazy plume. As a consequence, we account for the plume's geometry in our solution, by enforcing the line sink distribution along the curved perimeter of the contracting plume. The local strength of the line sink is deduced by matching the near- and far-field solutions of the recast plume (conservation) equations. Examples of similar matching approaches of the near- and far-field are given in Hunt & Kaye (2005) and in the study of non-Boussinesq plumes by Carlotti & Hunt (2005). To solve the resulting governing boundary value problem, we exploit the theory of functions of a complex variable (outlined in Chapter 2), and devise a conformal mapping between the upper-half plane and the induced flow domain.

The chapter is laid out as follows. In §4.1 we define the boundary value problem governing the flow induced by a lazy plume. In §4.1.1 the plume boundary condition subsequently applied along the curved plume perimeter is formulated. A conformal mapping that maps between the upper-half plane and the induced flow domain is devised in §4.2. We develop a solution for the induced flow in §4.3, and analyse the solution and present predictions on the response of the induced flow following a change to the plume's source conditions in §4.4. Finally, conclusions are given in §4.5.

4.1 Model development

Induced flows are low speed ($Ma << 1$), and have been observed to be laminar and absent of strong velocity gradients (see figures 1.1, 1.2, 1.3). Based on these observations, we follow Taylor (1958) by modelling the induced flow using Laplace's equation,

$$\nabla^2 \chi = 0, \tag{4.1}$$

where χ denotes the stream function (see Chapter 2 for details). The horizontal boundary is represented using a streamline. The plume boundary condition, represented as a distribution of sinks, is based on the solutions to the recast conservation equations for the plume from van den Bremer & Hunt (2014). Owing to the strong curvature of the plume perimeter and the near-source contraction (figure 4.1), the plume boundary condition is applied along the curved perimeter of the plume.

4.1.1 Plume boundary condition

Following van den Bremer & Hunt (2014), the original plume conservation equations from Lee & Emmons (1961), closed using the classic entrainment model,

$$u_\mathrm{e} = \alpha w_\mathrm{m}, \tag{4.2}$$

from Taylor (1945), where the local entrainment velocity, u_e, is a constant fraction, given by the entrainment coefficient α, of the local centre-line velocity in the plume, w_m, are recast in terms the local plume Richardson number Γ, the dimensionless half-width $\bar{b}$ and dimensionless centre-line velocity $\bar{w}$, with

$$\bar{b} = \frac{b(y)}{b_0} = \frac{1}{(2\pi)^{1/2}}\frac{{Q_0}^2}{M_0}, \quad \bar{w} = \frac{w_\mathrm{m}(y)}{w_0}. \tag{4.3}$$

The recast equations take the form

$$\frac{d\Gamma}{d\zeta} = \frac{3\Gamma(1-\Gamma)}{\bar{b}}, \quad \frac{d\bar{b}}{d\zeta} = 2-\Gamma, \quad \frac{d\bar{w}}{d\zeta} = \frac{\bar{w}}{\bar{b}}(\Gamma-1) \tag{4.4}$$

(see Appendix B for the algebra). The vertical and horizontal coordinates are scaled on the source width and defined as,

$$\zeta = \frac{2\alpha}{\pi^{1/2}b_0}y \quad \text{and} \quad \Delta = \frac{2\alpha}{\pi^{1/2}b_0}x, \tag{4.5}$$

respectively. We adopt the (average) value of $\alpha = \alpha_\mathrm{p} = 0.13$ corresponding to the pure plume (see Chapter 2), owing to the limited data available on the lazy plume. The source conditions for the contracting lazy plume are

$$\Gamma = \Gamma_0 > 2, \;\; \bar{b} = 1, \;\; \bar{w} = 1 \;\; \text{at} \;\; \zeta = 0. \tag{4.6}$$

We specify $\Gamma_0 > 2$ in (4.6), as we note from (4.4) that plume contraction requires $\Gamma > 2$.

van den Bremer & Hunt (2014) solve (4.4) subject to (4.6) to obtain the variation of the plume width and vertical velocity with local Richardson number,

$$\bar{b} = \frac{(\Gamma_0-1)^{1/3}}{\Gamma_0^{2/3}}\frac{\Gamma^{2/3}}{(\Gamma-1)^{1/3}}, \quad \bar{w} = \left(\frac{\Gamma_0}{\Gamma}\right)^{1/3}, \tag{4.7}$$

where

$$\frac{d\Gamma}{d\zeta} = \frac{-3\Gamma_0^{2/3}}{(\Gamma_0 - 1)^{1/3}}\Gamma^{1/3}(\Gamma - 1)^{4/3}. \tag{4.8}$$

To determine the plume boundary condition, we use the equivalence between the plume volume flux Q and stream function χ, or more conveniently their corresponding dimensionless forms

$$q = \frac{Q}{Q_0} \equiv \Psi = \frac{\chi}{\chi_0}, \tag{4.9}$$

with $\Psi = 1$ at the plume source. Noting that $q = \bar{b}\bar{w}$, from (4.7) we have

$$q = \left(\frac{\Gamma_0 - 1}{\Gamma_0}\right)^{1/3}\left(\frac{\Gamma}{\Gamma - 1}\right)^{1/3}. \tag{4.10}$$

To obtain the variation of q with height ζ, as required for the plume boundary condition, the solution to (4.8) for $\Gamma(\zeta)$ must be input into (4.10). The solution, however, does not have a closed-form and cannot be expressed in terms of standard functions.

Analogous to modelling the flow induced by the pure plume in Chapter 2, the expression for $q(\zeta)$ could be derived by replacing the physical source with a virtual line source, located at the virtual origin, $\zeta = -\zeta_{\text{sc}}$, below the actual source. However, as the virtual line plume remains pure for all heights above its source, the resulting expression $q(\zeta + \zeta_{\text{avs}})$ does not accurately capture the vertical variation of q in the lazy plume, particularly in the near-source region, and further, the flow does not exhibit a near-source contraction. Alternatively, we opt to match (separate) analytical solutions to (4.4) subject to (4.6) in the vicinity of the source (i.e. the 'near-field') and at a large height (i.e. the 'far-field'), and fit the resulting expression to the corresponding numerical solution for $q(\zeta)$. To attain the 'near-field' solution we apply the large Γ approximation, namely $\Gamma \approx \Gamma - 1$ in (4.4), and solve for $\bar{b}$ and $\bar{w}$ to obtain

$$\bar{b}_{\text{n}} = \left(\frac{\Gamma}{\Gamma_0}\right)^{1/3}, \quad \bar{w}_{\text{n}} = \left(\frac{\Gamma_0}{\Gamma}\right)^{1/3}, \tag{4.11}$$

and thereby

$$q_{\text{n}} = 1. \tag{4.12}$$

It is well established that a lazy plume transitions to a pure plume state asymptotically with height. As a result, the equations in (4.4) can be solved with $\Gamma = 1$ at a large height to obtain

$$\bar{b}_{\text{f}} = \zeta, \quad \bar{w}_{\text{f}} = {\Gamma_0}^{1/3}, \tag{4.13}$$

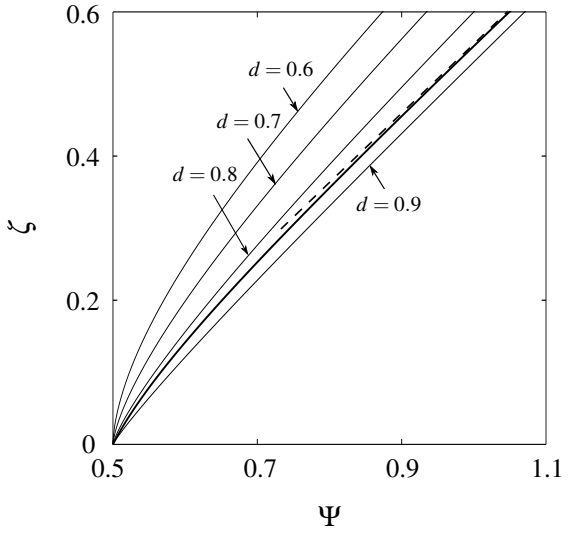

Fig. 4.2 Variation of the plume boundary condition Ψ with height ζ from (4.16) for $\Gamma_0 = 10$ with $d = \{0.6,\ 0.7,\ 0.8,\ 0.9\}$. Also shown are the corresponding numerical solution (bold line) and the linear vertical gradient corresponding to the far-field solution (4.14) (dashed line).

from which we evaluate a linearly increasing volume flux of the form

$$q_{\mathrm{f}} = \Gamma_0^{1/3}\zeta. \tag{4.14}$$

The subscripts '$(\cdot)_{\mathrm{n}}$' and '$(\cdot)_{\mathrm{f}}$' denote 'near-field' and 'far-field'. The 'far-field' solution in (4.13) – (4.14) indicates that the lazy plume entrains at a constant rate at a large height, and therefore acts as a sink of constant strength with respect to the ambient in this region. Matching the solutions (4.12) and (4.14), we approximate the lazy plume volume flux for $\zeta \geq 0$ using

$$q = \left(1 + (\Gamma_0^{1/3}\zeta)^{1/d}\right)^d, \tag{4.15}$$

where the exponent d is a constant. With the induced flow modelled on only one side of the plume due to the symmetry about the plume's centre-line, we halve the volume flux in (4.15), and use the equivalence between q and Ψ in (4.9) to obtain the plume boundary condition

$$\Psi = \frac{1}{2}\left(1 + (\Gamma_0^{1/3}\zeta)^{1/d}\right)^d \quad \text{on} \quad \Delta(\zeta) = \frac{2\alpha\bar{b}(\zeta)}{\pi^{1/2}} \tag{4.16}$$

for all $\zeta \geq 0$. The exponent d enables the vertical variation in Ψ to be matched with the equivalent numerical solution for $q(\zeta)/2$ (upon solving (4.8) and substituting into (4.10)).

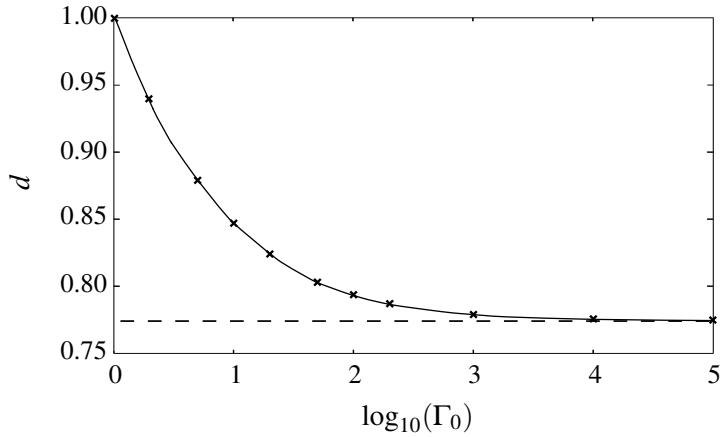

Fig. 4.3 The exponent d for $\Gamma_0 = \{1,\ 2,\ 5,\ 10,\ 20,\ 50,\ 100,\ 200,\ 1000,\ 10^4,\ 10^5\}$. The dashed line shows the large Γ_0 asymptote $d = 0.77$.

Figure 4.2 presents the variation of Ψ with height from (4.16) for a range of values of d, alongside the numerical solution (bold line) for a plume with source Richardson number $\Gamma_0 = 10$. A greater value of d corresponds to an increased vertical variation of Ψ or, equivalently, the (scaled) total volume entrained, over a given height. Evidently a value of $0.8 < d < 0.9$ provides the closest fit between the analytical model (4.16) and the numerical solution for the plume boundary condition in this instance. The matching exponent d has been optimised to fit to the corresponding numerical solution for the plume boundary condition using a Least Squares regression for plumes with source conditions ranging from pure ($\Gamma_0 = 1$) to strongly contracting lazy ($\Gamma_0 = 10^5$). With focus on the near-field region, we apply the fit below a height corresponding to $\Psi = 0.8$; that at which locally $1 < \Gamma < 1.35$, i.e. the plume is close to the pure regime, for all Γ_0 values considered. We evaluated the goodness-of-fit to be consistently above $R^2 = 0.996$. The values of d output using the regression are presented in table 4.1 (see §4.4) and have been plotted as a function of Γ_0 in figure 4.3. Evidently the exponent d reduces with source laziness and asymptotes to $d = 0.77$ (2 d.p.). Applying a fit to the points at which d has been evaluated at, we propose the function

$$d = \begin{cases} 0.235\Gamma_0^{-0.467} + 0.767 & \Gamma_0 < 10^4 \\ 0.770 & \Gamma_0 \geq 10^4. \end{cases} \tag{4.17}$$

In addition to identifying the plume boundary condition corresponding to a given source condition, expressions (4.16) and (4.17) enable one to straightforwardly determine the response of the boundary condition, and therefore the plume entrainment, to a change in the source conditions of the plume. For instance, figure 4.4 presents the vertical variation of Ψ

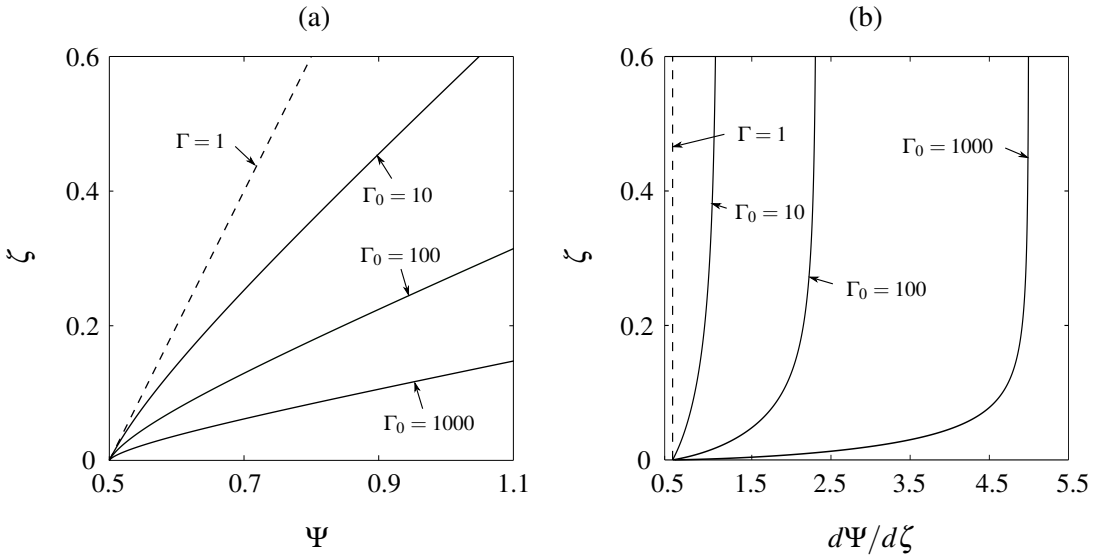

Fig. 4.4 Vertical variation of the lazy plume: (a) boundary condition Ψ from (4.16) using values of d from (4.17); and (b) its vertical gradient $d\Psi/d\zeta$ from (4.18) representing the (scaled) local entrainment velocity, for $\Gamma_0 = \{10,\ 100,\ 1000\}$. The corresponding expressions for the pure plume, $\Gamma = \Gamma_0 = 1$, are plotted for reference (dashed line).

(4.16) with height, and the corresponding (dimensionless) plume entrainment velocity,

$$\frac{d\Psi}{d\zeta} = \frac{u_\mathrm{e}}{2\alpha w_0} = \frac{\Gamma_0^{1/3}}{2}(\Gamma_0^{1/3}\zeta)^{(1-d)/d}\left(1+(\Gamma_0^{1/3}\zeta)^{1/d}\right)^{d-1}, \tag{4.18}$$

for $\Gamma_0 = \{10, 100, 1000\}$. We identify that a larger Γ_0 value corresponds to an increased (scaled) plume entrainment demand with height, i.e. an increasing $d\Psi/d\zeta$. Moreover, figure 4.4 (b) indicates that the plume entrainment velocity rapidly rises up to $\zeta \approx 0.2$, beyond which it grows at a markedly slower rate to the vertical gradient of the far-field (pure plume) behaviour in (4.14) given by $d\Psi/d\zeta = (dq_\mathrm{f}/d\zeta)/2 = \Gamma_0^{1/3}/2$.

Poisson's theorem, outlined in §4.2 and applied in §4.3 to solve the governing boundary value problem for the induced flow, requires that boundary conditions remain bounded. However, the plume boundary condition (4.16) is not bounded, and in its current form maintains non-zero velocities in the induced flow at an infinite height above the source. In practice, velocities in a plume will become indistinguishable from background air disturbances at sufficiently large heights. To capture this behaviour and simultaneously achieve boundedness, we continuously reduce the (positive) gradient of the stream function Ψ (4.16) beyond some height, and crucially, ensure that this local gradient, which is equivalent to the local entrained velocity, reaches zero at a finite height. Note that the value of the stream function must increase with height for the plume to remain acting as a sink to the induced flow. Accordingly,

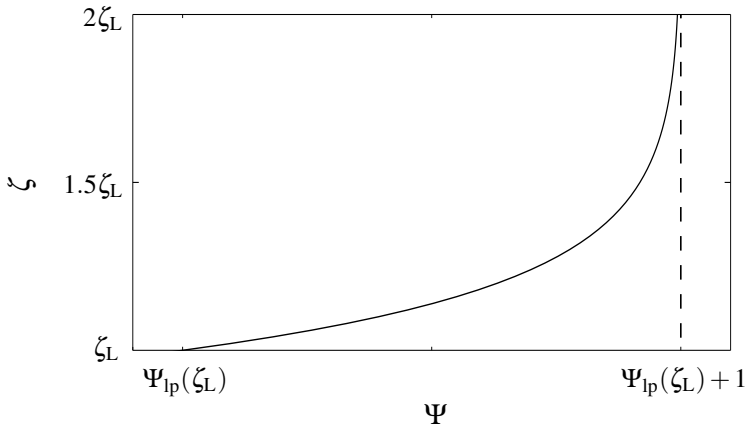

Fig. 4.5 The variation of the stream function Ψ imposed above the height $\zeta = \zeta_L$ in (4.19) to ensure boundedness of the plume boundary condition. An asymptote occurs at $\Psi = \Psi_{lp}(\zeta_L)+1$.

we modify the plume boundary condition (4.16), to

$$\begin{aligned}\Psi(\zeta) = \Psi_{lp}(\zeta) = (1/2)\cdot \mathrm{H}(\zeta_L - \zeta)\left(1+(\Gamma_0^{1/3}\zeta)^{1/d}\right)^d + \\ \mathrm{H}(\zeta-\zeta_L)\left[(1/2)\cdot\left(1+(\Gamma_0^{1/3}\zeta_L)^{1/d}\right)^d + 1 - e^{-(\zeta-\zeta_L)}\right],\end{aligned} \tag{4.19}$$

applied along $\Delta = \Delta_{lp} = 2\alpha_p \bar{b}(\zeta)/\pi^{1/2}$ for $\zeta \geq 0$. In (4.19) the subscript '$(\cdot)_{lp}$' denotes 'lazy plume' and ζ_L is the non-dimensional height beyond which the boundary condition is modified. We introduce the Heaviside step function H in (4.19) to ensure that the modification only occurs above the height $\zeta = \zeta_L$. The stream function has been plotted for $\zeta_L < \zeta < 2\zeta_L$ in figure 4.5. Evidently, the rate of increase of the stream function is reducing with height, and the function asymptotes to the value $\Psi = \Psi_{lp}(\zeta_L)+1$. This indicates that the entrainment velocity falls to a value of zero and thus the stream function maintains boundedness. The value of ζ_L was chosen so as not to affect the induced flow solution in our region of interest close to the source, and was achieved using $\zeta_L = 500 b_0$.

In summary, to model the induced flow we require a solution of

$$\nabla^2\Psi = \frac{\partial^2\Psi}{\partial\Delta^2} + \frac{\partial^2\Psi}{\partial\zeta^2} = 0, \quad \Delta_{lp} \leq \Delta < \infty, \quad 0 \leq \zeta < \infty \tag{4.20}$$

that satisfies the boundary condition (4.19) with values of the exponent d determined using (4.17), and

$$\Psi = 1/2 \quad \text{on} \quad \zeta = 0 \quad \text{for} \quad \Delta \geq \Delta_{\text{lp}}(x = b_0) = \frac{2\alpha}{\pi^{1/2}}. \tag{4.21}$$

4.2 The conformal mapping

Owing to complexity of the plume boundary condition (4.19) and the curved perimeter of the plume along which it is to be imposed, the boundary value problem (4.19) – (4.21) does not readily lend itself to standard analytical solution techniques, such as the method of separation of variables. However, appealing to the theory of functions of a complex variable, we show that it is possible to derive an analytical solution for the induced flow.

Poisson's integral theorem (see Chapter 2 for details) guarantees a solution to the Laplace equation (4.20) in the upper-half complex plane. Defining the complex variable $z = \eta + i\xi$, the theorem defines a unique function,

$$f(\eta,\xi) = \int_{-\infty}^{\infty} P(\eta - \tau) f(\tau, 0)\, d\tau, \quad \text{where} \quad P(\eta) = \frac{\pi^{-1}\xi}{\eta^2 + \xi^2}, \tag{4.22}$$

that is harmonic in the upper-half plane. The function $f(\tau, 0)$, which is bounded and defined along the entire real-axis, is specified as an input in (4.22). The function corresponds to the boundary condition applied along the real axis between locations specified by the limits of the integral, and is expressed in terms of the dummy variable, τ, which can be viewed as equivalent to the real coordinate η.

Alone, Poisson's theorem (4.22) is of limited use as our boundary value problem ((4.19) – (4.21)) is not defined in the upper-half plane in which the theorem is applied. To exploit Poisson's theorem, a one-to-one map is required that maps between the upper-half plane and the domain of the boundary value problem. In our case, the domain corresponds to the region occupied by the induced flow. The aim of the remainder of this section is to determine the one-to-one function (and its inverse). The function required must maintain the harmonic property of the Laplace equation, which is preserved by conformal (angle-preserving) mappings. Few conformal mappings exist in non-integral form and typically, those that do, straightforwardly map between simple geometries with straight edges (Ivanov & Trubetskov, 1994).

We construct a mapping consisting of a linear superposition of simple analytic functions to map between the region of the induced flow in the W-plane and the upper-half Z-plane. As a lead in, we begin with the source of inspiration for the proposed mapping, namely the

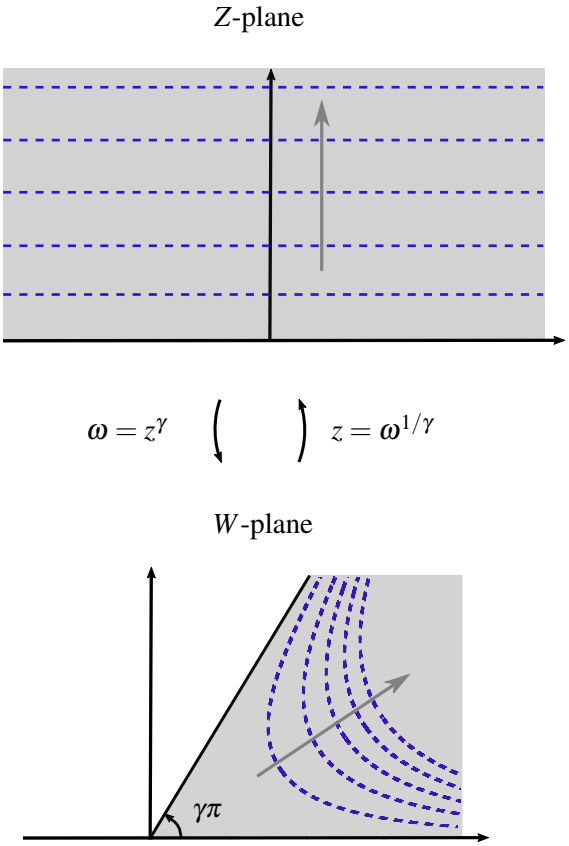

Fig. 4.6 The forward mapping, $z(\omega) = \omega^{1/\gamma}$, and corresponding inverse mapping, $\omega(z) = z^{\gamma}$, between the shaded regions of a straight-sided wedge with internal angle $\gamma\pi$ in the W-plane and the upper-half Z-plane. Each contour $\mathrm{Im}(z) = const. > 0$ in the Z-plane (dashed) maps to a corresponding curved contour internal to the wedge in the W-plane (dashed). The arrows indicate the direction of increasing value of the imaginary coordinate.

function

$$\omega(z) = z^{\gamma} \tag{4.23}$$

(derived using Schwarz-Christoffel's theorem in Appendix C), where the exponent γ is a constant. Commonly referred to as a power map, the function in (4.23) conformally maps the upper-half plane to the region internal to a straight-sided wedge with internal angle $\gamma\pi$, where $\gamma < 1$ (Ivanov & Trubetskov, 1994). The mapping (4.23) has the inverse

$$z(\omega) = \omega^{1/\gamma}. \tag{4.24}$$

Aside from a few simple geometries, including the straight-sided wedge, the Schwarz-Christoffel theorem (outlined in Appendix C) returns an integral that cannot be evaluated, and to find the values of the unspecified constants, typically a set of non-linear equations must be solved (Driscoll & Trefethen, 2002). In addition to these difficulties, the theorem is strictly limited to polygons. In our problem, the theorem can therefore only output a function that approximates the smooth curved boundary of the plume as a number of straight edges. Increased accuracy is attained upon increasing the number of straight edges, although, use of more than two edges requires a numerical evaluation of the integral function.

The starting point for the construction of a function that we propose to map between the upper-half plane and the induced flow region is based on the observation that, on applying the power map (4.23), horizontal lines corresponding to $\mathrm{Im}(z) = const. > 0$ in the upper-half Z-plane ('Im' reading 'imaginary part of') map to curves internal to a straight-sided wedge in the W-plane, as illustrated in figure 4.6. One immediately notes that these curves (dashed) have a similar shape to the curved perimeter of a contracting lazy plume (cf. figure 4.1). We exploit this observation to construct our mapping by first modifying (4.23) to give

$$\omega(z) = (z + a_{\mathrm{v}} i)^{\gamma}, \quad \text{where} \quad i^2 = -1 \tag{4.25}$$

and the constant $a_{\mathrm{v}} > 0$ corresponds to a vertical translation in the Z-plane. This translation ensures that the (mapped) region in the W-plane is enclosed by a curved boundary, and not the straight-sided boundary as is the case when $a_{\mathrm{v}} = 0$. Evident from figure 4.6, the location of the curved boundary internal to the straight-sided wedge is dependent on the chosen magnitude of the translation a_{v}, with increasing a_{v} corresponding to curves further from the corner of the wedge.

To complete the mapping we superpose: (i) an additional vertical translation, $-a_{\mathrm{v}} i$, to (4.25) in order to ensure that the curved boundary intersects the horizontal axis *in the W-plane*; and (ii) a horizontal translation $a_{\mathrm{h}} > 0$. The latter provides an additional degree of freedom when matching the coordinates of the curved boundary to the corresponding numerical solution for the plume perimeter. As a result, the completed (inverse) mapping takes the form

$$\omega(z) = (z + a_{\mathrm{v}} i)^{\gamma} + (a_{\mathrm{h}} - a_{\mathrm{v}} i). \tag{4.26}$$

Writing $c = a_{\mathrm{h}} - a_{\mathrm{v}} i$, the corresponding forward mapping is

$$z(\omega) = (\omega - c)^{1/\gamma} - a_{\mathrm{v}} i. \tag{4.27}$$

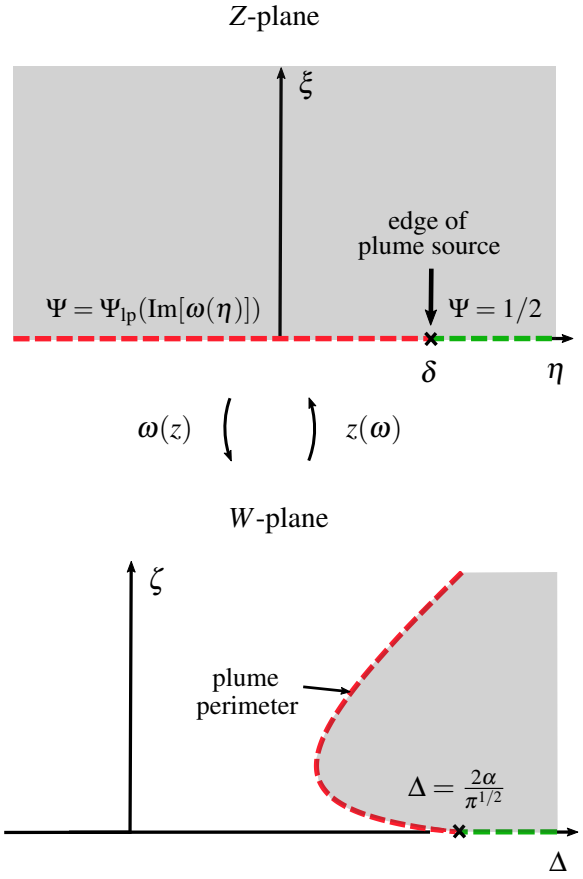

Fig. 4.7 The forward mapping, $z(\omega) = (\omega - c)^{1/\gamma} - a_v i$ (4.27), and corresponding inverse mapping, $\omega(z) = (z + a_v i)^{\gamma} + c$ (4.26), between the shaded upper-half Z-plane and induced flow region of the W-plane. Dashed lines show the plume perimeter (red) and the horizontal boundary (green). The colours indicate the corresponding locations where the boundary conditions representing the plume (4.19) and horizontal boundary (4.21) are applied. The edge of the plume source is indicated by a cross at ($\Delta = 2\alpha/\pi^{1/2}$, $\zeta = 0$) in the W-plane and maps to the coordinate ($\eta = \delta > 0$, $\xi = 0$) in the Z-plane.

The functions (4.26) and (4.27) map between the shaded areas in figure 4.7, corresponding to the upper-half Z-plane and the induced flow region in the W-plane. One should note that the portion of the mapped perimeter representing the horizontal boundary in the W-plane (represented schematically by the green dashed line in figure 4.7) is curved. However, owing to the small values of a_{v} required to represent the induced flow boundary in § 4.4, this curve has little noticeable difference from the required straight-sided boundary.

The physical location of the plume perimeter $\Delta = \Delta_{\mathrm{lp}}$ varies with the source Richardson number Γ_0. As a result, the constants γ, a_{h} and a_{v} in the inverse (4.26) and forward (4.27) mappings are to be identified for each Γ_0 value. These constants have been determined for $\Gamma_0 = \{2,\ 5,\ 10,\ 20,\ 50,\ 100,\ 200,\ 1000\}$ and are listed in table 4.1 in § 4.4.

4.3 Solution for the induced flow

Poisson's integral theorem (4.22), the conformal mapping constructed (4.27) and its inverse mapping (4.26) can now be applied to develop the solution for the induced flow.

To apply Poisson's theorem we first identify the location on the real axis in the Z-plane, $\mathrm{Im}(z) = 0$, to which the coordinate defining the edge of the plume source in the W-plane, $(\Delta = 2\alpha/\pi^{1/2},\ \zeta = 0)$, maps. This is necessary in order to specify the limits of the integrals in Poisson's theorem, which define the interval over which each boundary condition is applied. Accordingly, we define the real coordinate along the real axis in the Z-plane,

$$\eta = \delta = z\left(\frac{2\alpha}{\pi^{1/2}}\right), \tag{4.28}$$

which we substitute into (4.22) on writing

$$f(\tau,0) = f(\eta,0) = \begin{cases} \Psi_{\mathrm{lp}}(\mathrm{Im}[\omega(\eta)]) & \text{for } \eta = [-\infty,\delta] \\ 1/2 & \text{for } \eta = [\delta,\infty]. \end{cases} \tag{4.29}$$

The argument of the plume boundary condition in (4.29) corresponds to the vertical coordinate in the W-plane. To account for each of the boundary conditions in (4.29), Poisson's theorem (4.22) is decomposed into the sum of two integrals

$$f(\eta,\xi) = \int_{-\infty}^{\delta} P(\eta-\tau)\Psi_{\mathrm{lp}}(\mathrm{Im}[\omega(\tau)])\,d\tau + \frac{1}{2}\int_{\delta}^{\infty} P(\eta-\tau)\,d\tau. \tag{4.30}$$

Mapping back into the physical domain of the induced flow and evaluating the second integral in (4.30), we obtain the following harmonic solution for the induced flow

$$\begin{aligned}\Psi(\Delta,\zeta) &= F^{-1}(f(\eta,\xi)) \\ &= F^{-1}\left\{\int_{-\infty}^{\delta} P(\eta-\tau)\Psi_{\mathrm{lp}}(\mathrm{Im}[\omega(\tau)])\,d\tau + \frac{1}{4} - \frac{1}{2\pi}\tan^{-1}\left(\frac{\delta-\eta}{\xi}\right)\right\}.\end{aligned} \tag{4.31}$$

The mapping function $F^{-1}(f(\eta,\xi))$ in (4.31) maps the coordinates (η,ξ) in the Z-plane back to the coordinates (Δ,ζ) in the original W-plane of the induced flow domain, thus performing an equivalent operation to the inverse mapping $\omega(z)$ in (4.26) acting on the complex coordinate. Whilst we acknowledge that this is not conventional notation, we adopt it for convenience and reiterate that the function $F^{-1}()$ strictly acts on the coordinates (η,ξ) of the function.

In the following section we compare our induced flow solution (4.31) with that attained when the plume width is not accounted for, by applying the plume boundary condition, Ψ_{lp} in (4.19), along the vertical axis at $\Delta = 0$. For this domain, we employ the mapping exponent $\gamma = 1/2$. Selecting the mapping constants $a_{\mathrm{h}} = a_{\mathrm{v}} = 0$ (implying that $\delta = 0$), the solution takes the form

$$\Psi(\Delta,\zeta) = G^{-1}\left\{\int_{-\infty}^{0} P(\eta-\tau)\Psi_{\mathrm{lp}}(\mathrm{Im}[\omega(\tau)])\,d\tau + \frac{1}{4} - \frac{1}{2\pi}\tan^{-1}\left(\frac{\eta}{\xi}\right)\right\}, \tag{4.32}$$

where the mapping function $G^{-1}(f(\eta,\xi))$ maps the coordinates (η,ξ) in the Z-plane to the coordinates (Δ,ζ) of the quadrant in the W-plane representing the induced flow domain.

4.4 Streamline pattern

The matching exponent d (evaluated in §4.1.1) and mapping constants γ, a_{h} and a_{v} required to construct our solution for the induced flow (4.31) are given in table 4.1 for plumes with source conditions ranging from weakly lazy ($\Gamma_0 = 2$) to strongly lazy ($\Gamma_0 = 1000$). The mapping constants have been optimised to fit the mapped plume perimeter (represented by applying the inverse map (4.26) to the real axis of the Z-plane) to the corresponding numerical solution in the near-field. The near-field has been selected as the region, $\zeta \leq 8\alpha/\pi^{1/2}$ or, equivalently, below a height corresponding to four source half-widths. The source half-width represents the governing length-scale for a lazy plume as discussed in Hunt & Kaye (2005) and thus the chosen demarcation of near- and far-fields is reasonable. A constraint was applied during the optimisation to ensure that the fitted perimeter did not fall inside that of the corresponding numerical solution in order to maintain close agreement beyond the

Γ_0	d	γ	a_v $(\times 10^{-3})$	a_h
2	0.940	0.465	0.29	0.138
5	0.879	0.468	1.80	0.106
10	0.847	0.464	2.90	0.077
20	0.824	0.460	2.80	0.055
50	0.803	0.457	2.00	0.036
100	0.794	0.456	1.40	0.027
200	0.787	0.455	0.92	0.020
1000	0.779	0.454	0.32	0.011

Table 4.1 Values for the matching exponent d and mapping constants γ, a_v and a_h for $\Gamma_0 = \{2,\ 5,\ 10,\ 20,\ 50,\ 100,\ 200,\ 1000\}$.

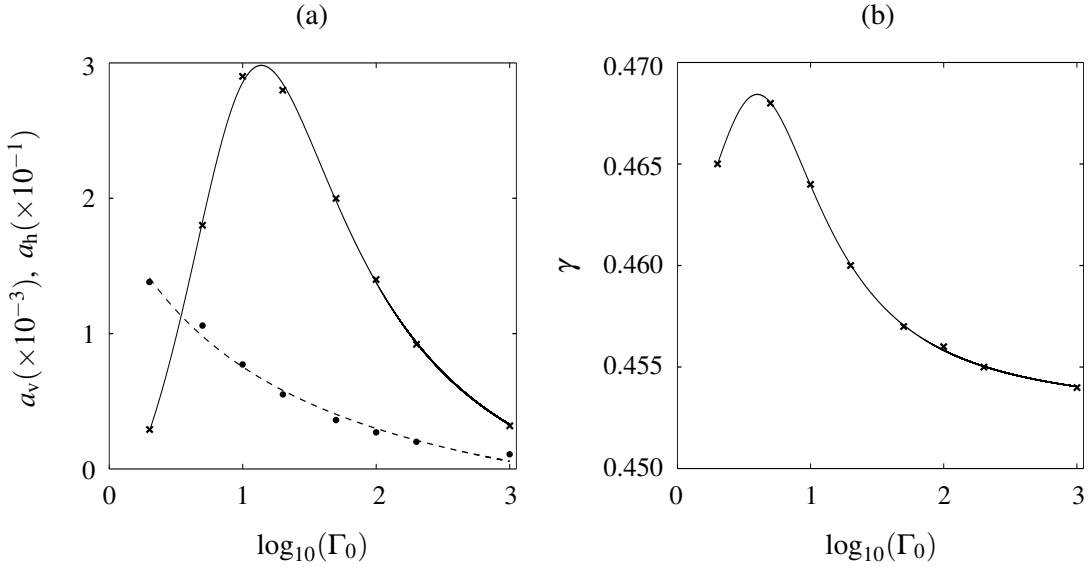

Fig. 4.8 Variation of the mapping constants (a) a_h (dashed line), a_v and (b) γ with Γ_0. The functions (4.33) – (4.35) have been fitted to values of the constants (markers) from table 4.1.

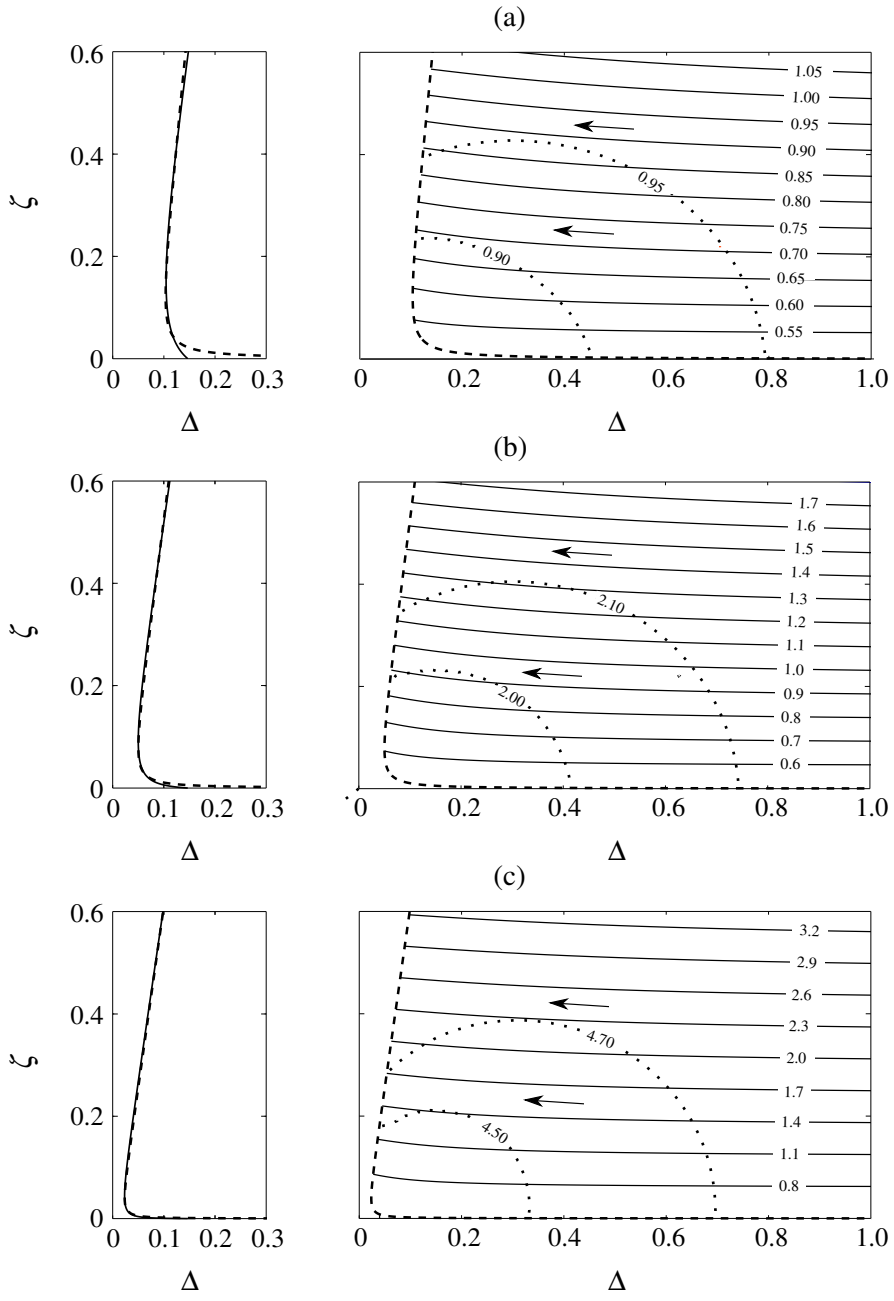

Fig. 4.9 Contracting plume perimeter (left) and streamlines in the induced flow (right) for (a) $\Gamma_0 = 10$, (b) $\Gamma_0 = 100$ and (c) $\Gamma_0 = 1000$. Left: the mapped plume perimeter (dashed line), plotted using values of the mapping constants from table 4.1, is presented alongside the corresponding numerical solution (solid line). Right: streamlines, $\Psi = const.$ (solid lines), and contours of constant speed, $\bar{u} = U/(2\alpha w_0) = const.$ (dotted lines). The values of the stream function and speeds are overlain. The dashed lines denote the mapped plume perimeter. Arrows indicate the bulk direction of flow.

immediate vicinity of the source. Figure 4.8 illustrates the variation of the mapping constants γ, $a_{\rm h}$ and $a_{\rm v}$ with Γ_0, to which we have fitted the following rational polynomial functions,

$$a_{\rm h} = \frac{-0.074E + 0.247}{E + 1.286}, \tag{4.33}$$

$$a_{\rm v} = \frac{-0.743E^2 + 2.943E - 0.548}{1000(E^2 - 1.860E + 1.439)} \tag{4.34}$$

and

$$\gamma = \frac{0.452E^2 - 0.490E + 0.303}{E^2 - 1.088E + 0.658}, \tag{4.35}$$

where $E = \log_{10}(\Gamma_0)$. Expressions (4.33) – (4.35) enable the mapping constants corresponding to any plume source Richardson number, $\Gamma_0 \geq 2$, to be determined. Note that only a small variation occurs in the exponent γ, however, fixing γ to a constant value (independent of Γ_0) and optimising to obtain $a_{\rm v}$ and $a_{\rm h}$ resulted in an increased error between the mapped plume perimeters and corresponding numerical solutions. Figure 4.9 (left) illustrating the fitted plume perimeter (dashed line) and corresponding numerical solution (solid line) for $\Gamma_0 = \{10, 100 \text{ and } 1000\}$ indicates close agreement between the curves. In fact, the fitted curve maintains a mean percentage error in the width (for $\zeta \leq 8\alpha/\pi^{1/2}$) of less than 5% for all source Γ_0 values considered in table 4.1. This error reduces with increasing Γ_0 value. Focussing on a given flow, it is evident that much of the contribution to the error is due to the region immediately above the source.

Streamline portraits of the induced flow are shown adjacent to plume perimeter plots in figure 4.9. For comparative purposes, we have fixed the source fluxes, Q_0 and M_0, to maintain the scaling, $b_0 = {Q_0}^2/((2\pi)^{1/2}M_0)$, for each plot, and solely varied B_0 to achieve the desired value of Γ_0. To plot figure 4.9 we have had to resort to numerics, owing to the complexity of our integral solution (4.31). The integral of the solution was evaluated using an adaptive quadrature numerical scheme. The resulting output was confirmed on comparison with the full numerical solution of the governing boundary value problem for the induced flow based on a finite-difference scheme (outlined in Appendix E, with further details in §4.3.1 and §4.3.2 in Hunt (1994)). Specifically, the streamline portrait output using the full numerical solution is graphically indistinguishable from that plotted using the analytical solution (4.31). We verified that 'crowding' (see Chapter 2) was not an issue when plotting streamlines for the near-source region of the induced flow on identifying that the solution remained grid independent, i.e. increasing the number of grid points in the numerics resulted in no change to the solution.

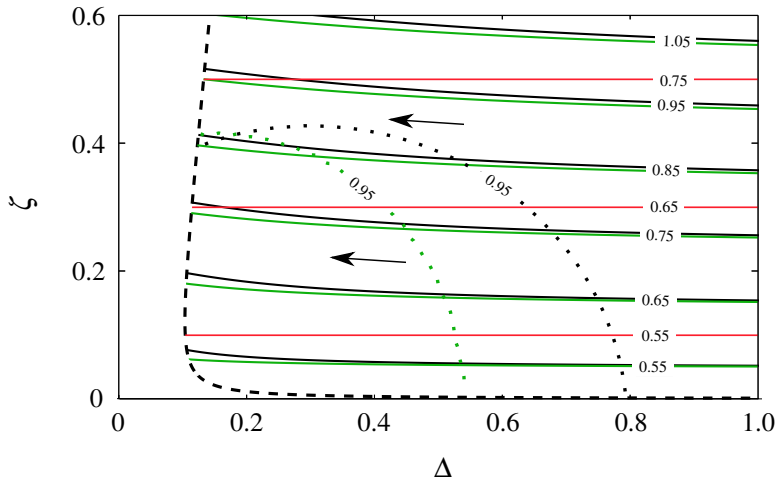

Fig. 4.10 Streamlines, $\Psi = const.$ (solid lines), and a contour of constant speed, $\bar{u} = U/(2\alpha w_0) = 0.95$ (dotted lines), in the induced flow of a lazy plume with $\Gamma_0 = 10$, when accounting for the plume width in the solution (4.31) (black) and when approximating the plume as a vertical line (4.32) (green). The induced flow solution for the pure plume from Chapter 2 (with the appropriate scalings) is superimposed. The dashed line represents the plume perimeter.

The streamline portraits in figure 4.9 indicate that the induced flows all have a shallow upward inclination. Fluid in the induced flow rises to match the increasing entrainment demand of the plume with height, a demand driven by the relative excess in buoyancy flux supplied at the source. From the contours of constant speed, $\bar{u} = const.$, we identify that the corresponding speed of the induced flow increases with distance from the source. Though there is little variation in the inclination of the streamlines evident upon comparing the plots in figure 4.9, we identify that the (dimensionless) speed (scaled on the plume source speed as $w_0 \equiv 2^{1/2} M_0/Q_0$), at a given location in the induced flow, rises with the source Richardson number Γ_0. This is due to the increased source buoyancy flux input B_0 for a higher Γ_0 value. It is important to note, however, that on a corresponding dimensional plot, which can be straightforwardly obtained using the dimensionless plots in figure 4.9, a plume with a greater Γ_0 value does not necessarily induce a greater (dimensional) speed at a given location. For instance, a flow with a greater source speed can induce a greater speed in the region close to the source, despite having, say, a lower source buoyancy or Γ_0 value. The scenario presented in §6.5 in Chapter 6 is an example of this, where the 'Velocity Ratio' diagnostic introduced in Chapter 3 has been applied to compare the speeds induced by a forced plume and a lazy plume. The forced plume is subject to a greater source velocity but a lower buoyancy input.

A natural question that arises at this stage is whether accounting for the curved plume perimeter has any significant effect on our induced flow solution (4.31). We compare streamlines and a contour of constant speed in the induced flow in figure 4.10 when the (contracting) curved plume perimeter is accounted for in the solution (4.31) (black) and when the plume perimeter is simply modelled as a vertical line (4.32) (green). Evidently, there is a difference between the two solutions, which becomes more pronounced closer to the plume perimeter and at greater heights. The streamlines in green are, in general, less inclined, as the inclination of the streamlines reduces with increasing horizontal distance from the location where the plume boundary condition is applied. Both streamline portraits provide a marked change from the corresponding streamlines of the horizontal flow induced by the pure plume (red).

The formulation of the induced flow solution (4.31), illustrated in figure 4.9, is the primary result of this chapter. In the following, we provide some additional insights based on further analysis of the solution. Specifically, we assess the role of source laziness on the induced flow pattern. Comparing the plots in figure 4.9, we noted that there was little discernible difference in the inclination of the streamlines. To quantify these differences, one can evaluate the inclination to the horizontal of the streamlines at the edge of the plume,

$$\theta_{\mathrm{p}} = -\tan^{-1}\left(\left.\frac{\mathrm{d}\zeta}{\mathrm{d}\Delta}\right|_{\Delta=\Delta_{\mathrm{lp}}}\right) \tag{4.36}$$

(cf. figure 4.1). The plume perimeter corresponds to the location of greatest inclination along each induced flow streamline. Figure 4.11 presents the inclination of the streamlines at the plume perimeter, θ_{p}, as a function of the local Richardson number Γ, which, for lazy plumes, decreases with height. Each curve in figure 4.11 represents a plume with a different source Γ_0 value, and moving from right to left along a given curve corresponds to increasing height. The position of each of the curves differs, indicating, contrary to our earlier qualitative visual comparison, that a (subtle) variation does in fact exist in the inclination of each induced flow along the plume perimeter. Further, in contrast to the idealised induced flows considered in Chapter 2, the curves in figure 4.11 indicate that a local variation in the inclination exists with height. The curves all have a similar shape across the range of Γ_0 values. Close the plume source, the horizontal boundary has a marked effect on the induced flow, resulting in less inclined streamlines in this region. The effect of the boundary becomes less pronounced with height, and the flow steepens up to a maximum (i.e. a local turning point). Following the local maximum, the plume asymptotes to a pure state ($\Gamma = 1$), which is associated with a horizontal induced flow (with zero inclination). The inclination at the plume perimeter reaches a local maximum when $1 < \Gamma < 2$.

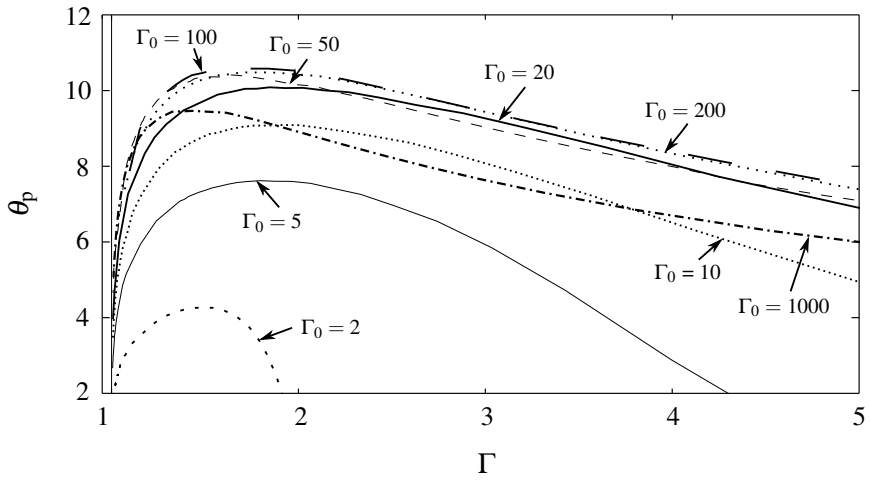

Fig. 4.11 Inclination (in degrees) of streamlines in the induced flow adjacent to the perimeter of the plume as a function of the local Γ for $\Gamma_0 = \{2,\ 5,\ 10,\ 20,\ 50,\ 100,\ 200,\ 1000\}$.

The maximum inclination in the induced flow along the plume perimeter, $\theta_p = \theta_{max}$, attained by each plume considered in figure 4.11, has been plotted against its respective source Richardson number in figure 4.12 (a). From the plot, we predict the greatest inclination to occur for $\Gamma_0 \approx 100$.

Figure 4.13 is a complementary plot to figure 4.11 illustrating the vertical variation of the induced flow inclination along the plume perimeter θ_p for different plumes. Each curve in figure 4.13 corresponds to a plume with a different source Γ_0 value. The local value of Γ for a lazier plume varies more rapidly with height, and consequently, its induced flow, in general, reaches a maximum inclination at a lower height in the plot. The height of maximum inclination, $\zeta = \zeta_{max}$, and the plume neck height $\zeta = \zeta_n$ (i.e. locally when $\Gamma = 2$) have been plotted as a function of the source Γ_0 value in figure 4.12 (b). Comparing the fitted curves in figure 4.12 (b), we identify that the height of maximum inclination is consistently a small distance above the height of the plume neck. Moreover, we predict that a local maximum is attained by each of the curves in figure 4.12 (b). The plume neck height is greatest when $\Gamma_0 \approx 10$, whilst the maximum inclination height is greatest when $\Gamma_0 \approx 5$. The latter occurs at a small value of Γ_0 as the plume has a relatively slow variation in Γ with height, whilst also exhibiting a contracting above the source (as a result of $\Gamma_0 > 2$). This combination results in its associated curve in figure 4.13 having the largest radius of curvature, and hence the greatest height at which maximum inclination is attained. It is important to note that the values cited above are of course specific to the particular entrainment model chosen, and for this reason are not discussed further.

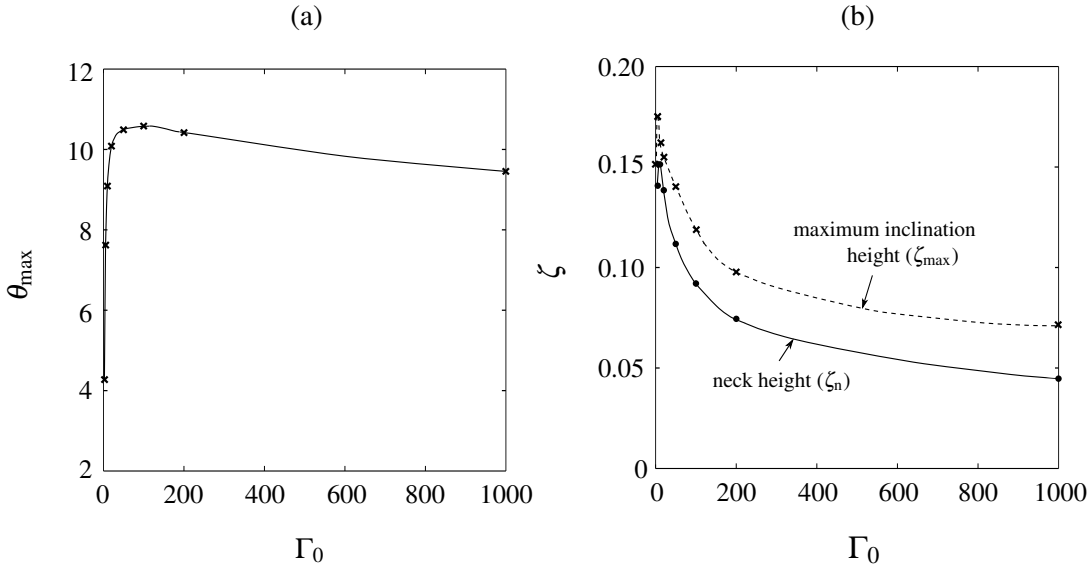

Fig. 4.12 (a) The maximum inclination, $\theta_p = \theta_{max}$ (in degrees), attained by streamlines in the induced flow (or equivalently the magnitude of the local maxima in figure 4.11), and (b) the (dimensionless) heights of the plume neck ζ_n and maximum inclination of the streamlines ζ_{max}, for plumes with source conditions $\Gamma_0 = \{2,\ 5,\ 10,\ 20,\ 50,\ 100,\ 200,\ 1000\}$.

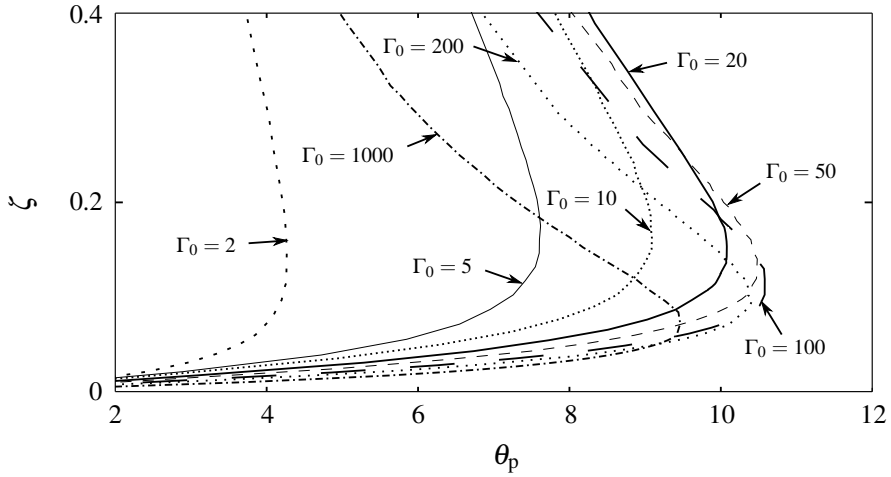

Fig. 4.13 The local variation in inclination θ_p (in degrees) with (dimensionless) height ζ for source conditions $\Gamma_0 = \{2,\ 5,\ 10,\ 20,\ 50,\ 100,\ 200,\ 1000\}$.

4.5 Conclusions

In this chapter a solution has been developed for the flow induced by a contracting lazy plume above slender horizontal slot. Our solution shows that, in contrast to the (purely horizontal) flow induced by the pure plume, and downwardly inclined flow induced by the jet (see Chapter 2), a contracting plume induces a flow with an upward inclination. This presents a consistent picture, with the inclination of the induced flow responding to the relative excess in buoyancy flux at the source of the lazy plume. The inclination of the contracting plume's induced flow is found to vary with the plume source Richardson number Γ_0. Moreover, in contrast to the idealised induced flows (presented in Chapter 2), the inclination of the induced flow for a given plume varies with height, attaining a maximum marginally above the plume neck height.

In addition to the insight into the flow induced by the contracting plume, a key contribution of this chapter are the developments to the solution method. A novel conformal mapping has been devised that has enabled us to accurately account for the curved plume perimeter. Further, the modification at a large vertical extent imposed to maintain boundedness of the plume boundary condition has enabled us to utilise Poisson's theorem to model the near-field of the induced flow. This has wider implications, indicating that the general solution technique need not be disregarded when boundary conditions are unbounded. Any future developments to our fundamental understanding of lazy plumes that occur, for example to improve the description of plume entrainment as in Carlotti & Hunt (2017), can be accounted for using the solution technique described upon a straightforward reimplementation beginning with the plume boundary condition. This highlights the robustness of the modelling approach.

In the following chapter we devise a model for the flow induced by a plume that is formed by a vertical off-source uniform supply of buoyancy flux. Such a plume can be considered as analogous to the lazy plume in this chapter, as the flow is strongly accelerated by the input of buoyancy. The acceleration occurs along the entire height of the distributed plume due to the continuous input of buoyancy with height, as we shall see in the following chapter.

Chapter 5

Flows induced by vertically distributed plumes

In this chapter an analytical solution is developed for the flow induced by a partially-confined vertically distributed plume in an otherwise quiescent uniform environment. The distributed plume is formed by a planar vertical source emitting a flux of buoyancy uniformly over its entire area. This can be considered to be equivalent to an off-source supply of buoyancy flux above the line source. The general solution technique in the seminal paper by Taylor (1958) is adopted, with the model of a vertically distributed plume developed by Cooper & Hunt (2010) used to represent the plume boundary condition. The method of separation of variables is used to solve the governing boundary value problem, but equally the method from complex analysis applied in the previous chapter could have been employed.

The purpose of the following is to set the scene for modelling the induced flow, rather than provide a detailed literature review. A review of planar boundary layers can be found in Wells & Worster (2008). Plane vertical surfaces at a different temperature to their surroundings are prevalent. Examples include an area of a room's wall that is heated via solar radiation and the façade of glazed atria cooled by outdoor air. Heat transfer from the surface results in a warming or cooling of fluid adjacent to it, resulting in a local buoyancy g' which drives vertical motion leading to the development of a convective boundary layer. This boundary layer is referred to as a vertically distributed plume (Cooper & Hunt, 2010; Caudwell et al., 2016; McConnochie & Kerr, 2016b). A vertically distributed plume can also be formed following a supply of buoyant fluid from a vertical source. An example is the plume that forms due to the ablation of a vertical ice wall submerged in a polar ocean as modelled by Kerr & McConnochie (2015), McConnochie & Kerr (2016a) and McConnochie & Kerr (2016b). The Grashof number relates driving buoyancy forces to momentum diffusivity in

the plume and in a rising plume increases with height. At a sufficiently large height, when the Grashof number, Gr, exceeds a critical value of 10^9 (Turner, 1979), the plume flow becomes fully turbulent. In the turbulent regime, a horizontal flow cross-section can be separated into three distinct regions each governed by different flow dynamics; a near-wall laminar conductive region, an intermediate viscous turbulent layer and outer inertial turbulent layer (Wells & Worster, 2008). Vliet & Liu (1969) measure that the inner layers only account for a small proportion ($< 0.25\%$) of the plume's total volume flux.

Literature on distributed plumes is mainly centred on those which develop adjacent to isothermal surfaces. These studies primarily focus on identifying the vertical variation of the convective heat flux, H, supplied at the source from the leading edge of the surface. This is useful, for instance, to identify the lifetime of a submerged ice feature, for which the melting rate is controlled, in part, by the heat supplied to the ice–water interface (Wells & Worster, 2008). The heat flux is typically represented in terms of the Nusselt number,

$$Nu = \frac{Hy}{\rho_a c_h D \Delta T} \tag{5.1}$$

(Jiji, 2006), signifying the ratio of the convective to conductive heat transfer across the boundary, where ρ_a is the density of the ambient, c_h the specific heat capacity, D the relevant thermal diffusivity and ΔT the temperature difference between the surface and the ambient. Experimental studies (e.g. Cheesewright (1967), Tsuji & Nagano (1988), Tsuji & Nagano (1989)) have concluded that in the turbulent region of the plume flow,

$$Nu = Ra^{1/3}, \quad \text{where} \quad Ra = \frac{g' y^3}{D\nu} = Gr \cdot Pr, \tag{5.2}$$

with Ra denoting the Rayleigh number, ν the kinematic viscosity and $Pr = \nu/D$ the Prandtl number. This scaling has also been proposed based on asymptotic and scaling arguments by George & Capp (1979) and Hölling & Herwig (2005). Expression (5.2) suggests that the heat flux supplied at the source is independent of height. By relating the convective heat flux to the plume buoyancy flux using,

$$B = \frac{H e_c g}{\rho_a c_h} \tag{5.3}$$

(Linden, 1999), where e_c is the thermal expansion coefficient, we identify that the turbulent region of a plume adjacent to an isothermal surface can be considered to have identical dynamics to that which develops following a uniform source supply of buoyancy flux. The equivalence leads to the derivation of universal scalings for the distributed plume. The scalings for the mean width b, vertical velocity w and buoyancy g' (relative to the ambient)

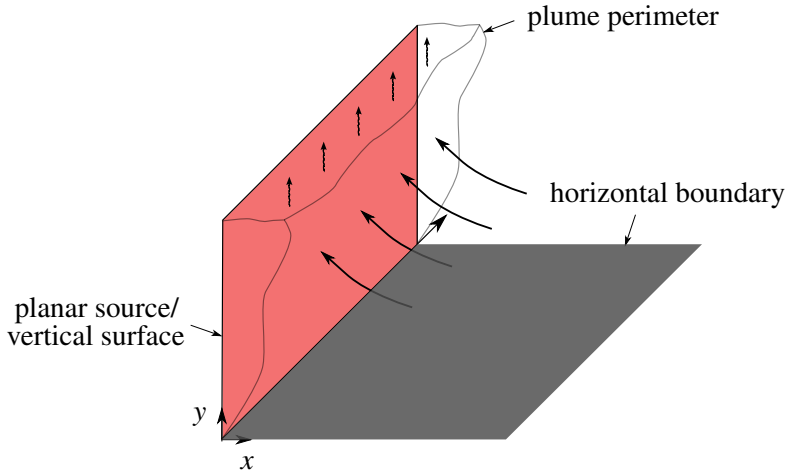

Fig. 5.1 Schematic of a partially-confined vertical planar source (red) emitting a constant flux of buoyancy uniformly over its area, and driving a turbulent convective plume that draws a bulk secondary laminar inflow (in the general direction indicated by the curved arrows) from an otherwise quiescent ambient.

in the turbulent region of a vertically distributed plume are

$$b \propto y, \quad w \propto y^{1/3} \quad \text{and} \quad g' \propto y^{-1/3} \tag{5.4}$$

(Wells & Worster, 2008; Cooper & Hunt, 2010).

The main focus of the literature on the distributed plume has been to gain insight into the boundary layer/plume flow. Studies have overlooked the secondary flow in the ambient that these flows induce. The induced flow can have important implications in practice, for example, influencing the comfort of occupants in a room where the flow of air naturally induced toward a warm or a cool wall may prove beneficial by leading odours, stale air or heat and humidity away from occupants and towards the wall.

We focus in this chapter on modelling the flow induced by the turbulent vertically distributed plume from a rigid vertical surface located in a partially-confined environment formed by a horizontal boundary in line with the base of the source. Figure 5.1 is a schematic of the situation considered. We adopt the general approach from Taylor (1958) (detailed in Chapter 2) to define a boundary value problem to model the plume induced flow. The induced flow is represented as an inviscid potential flow. The horizontal boundary is modelled using a slip-boundary condition, and the plume boundary condition using a vertical distribution of line sinks (or point sinks in the plane), with local strength governed by the local entrainment velocity. The strength of the sinks is determined based on the formulation of Cooper & Hunt

(2010).

This chapter is laid out as follows: §5.1 provides an outline of the general method that is employed to model the plume induced flow. The vertically distributed plume boundary condition is formulated in §5.1.1. Following this, in §5.2 an analytical solution for the induced flow is derived. In §5.3 we analyse the solution, including the resulting flow shape and speeds induced, the effect that the plume source strength has on the induced flow and typical induced flow speeds expected in an application in the built environment. Conclusions are given in §5.4.

5.1 Model development

In contrast to the development of solutions for the flows induced by turbulent plumes above non-idealised horizontal sources, it is not possible to identify a characteristic length scale when modelling the flow induced by a vertically distributed plume with a uniform input of buoyancy. As a result, from a modelling perspective, we decide to reframe the problem in terms of a more general scenario, corresponding to a distributed plume that is vertically offset by a distance a from the horizontal boundary. Our original problem now represents the limiting case when this characteristic scale $a \to 0$.

As before, we model the flow induced by the plume using an inviscid potential flow, expressed in terms of the stream function χ as

$$\nabla^2 \chi = 0. \tag{5.5}$$

To formulate the boundary conditions, with reference to figure 5.2, we introduce a global plane polar coordinate system (r, θ), originating at the base of the offset plume, and a second system, (r_a, θ_a), originating at a distance a below the horizontal boundary — the latter to account for the vertical plume offset. Indeed this approach was used by Hunt & Ingham (1992) when modelling the Aaberg exhaust hood. The coordinates (x, y) denote a local Cartesian coordinate system, originating at the offset distance a along the vertical axis (indicated by the dot in figure 5.6), used to model the distributed plume in §5.1.1. Measurements of a saline plume in the laboratory by Cooper & Hunt (2010)) showed that the distributed plume is straight-sided and slender. Therefore we approximate the plume width as infinitesimal and apply the plume boundary condition, $\chi = \chi_{\text{vdp}}$, along the vertical axis above the vertical offset at $y = a$. A streamline is enforced along the horizontal axis to represent the horizontal boundary. As with the horizontal boundary, we represent the

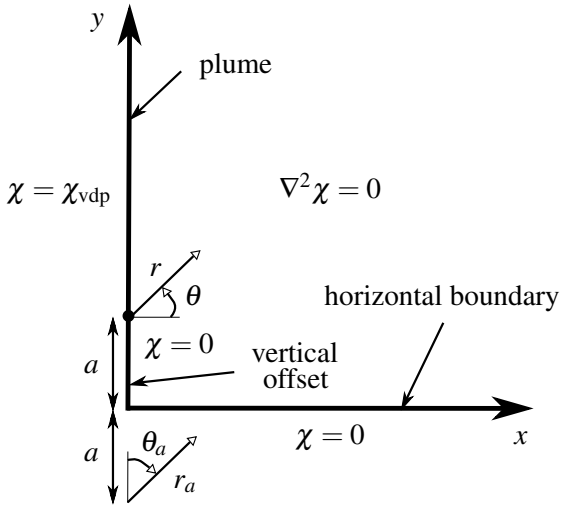

Fig. 5.2 Domain, boundary conditions and coordinates for the boundary value problem modelling the flow induced by a vertically distributed plume offset by a distance a from a horizontal boundary.

vertical offset as a solid boundary (supplying zero buoyancy flux) and thereby model it as a streamline.

The governing boundary value problem to be solved can thus be represented mathematically by Laplace's equation (5.5), and the boundary conditions

$$\chi = \chi_{\text{vdp}} \quad \text{on} \quad \theta = \pi/2 \quad \text{and} \quad \theta_a = 0, \tag{5.6}$$

$$\chi = 0 \quad \text{when} \quad \theta = -\pi/2 \quad \text{and} \quad \theta_a = 0, \tag{5.7}$$

$$\chi = 0 \quad \text{when} \quad r = r_a \quad \text{and} \quad \theta = \theta_a - \pi/2. \tag{5.8}$$

Boundary conditions (5.7) and (5.8) account for the vertical offset and horizontal boundary, respectively. In the limiting case of a zero offset, when $a \to 0$, we disregard condition (5.7) and consider Laplace's equation subject to the boundary conditions (5.6) and (5.8).

5.1.1 Plume boundary condition

To model the flow induced by the turbulent vertically distributed plume using the boundary value problem outlined in equations (5.5) – (5.8), we require the form of the boundary condition $\chi = \chi_{\text{vdp}}$ that describes the plume. For this, we adopt the model of the plume

formulated by Cooper & Hunt (2010) as outlined below — a formulation based on the integral technique from Morton et al. (1956) discussed in Chapter 2. The entrainment hypothesis, $u_e = \alpha w$, introduced in Taylor (1945) is used by Cooper & Hunt (2010) to close the governing equations. This hypothesis links the local entrainment velocity, u_e, to a characteristic local plume velocity, w, using the entrainment coefficient α. By tracking the position of a front in a filling box, Cooper & Hunt (2010) measure the (top-hat) entrainment coefficient, $\alpha = \alpha_{vdp} = 0.02$, in their experiments.

Assuming top-hat profiles (i.e. values remain constant across the plume width) for velocity and buoyancy and that the plume is turbulent for all heights, Cooper & Hunt (2010) derive the following coupled set of ordinary differential equations to model the distributed plume,

$$\frac{dQ}{dy} = \alpha_{vdp}\frac{M}{Q}, \quad \frac{dM}{dy} = \frac{QB}{M}, \quad \frac{dB}{dy} = \beta. \tag{5.9}$$

These equations represent the conservation of fluxes of volume, momentum and buoyancy, respectively, and are the starting point for determining the form of χ_{vdp}. The equations are expressed in terms of the integral fluxes of volume ($Q = bw$), momentum ($M = bw^2$) and buoyancy ($B = bwg'$), represented in terms of the plume width b, the local vertical velocity w and local buoyancy g'. The quantity β denotes the buoyancy flux per unit area supplied by the vertical source.

Solving the plume equations in (5.9), Cooper & Hunt (2010) give the fluxes Q, M and B as self-similar solutions, with

$$Q = \frac{3}{4}\left(\frac{4}{5}\right)^{1/3} {\alpha_{vdp}}^{2/3}\beta^{1/3}y^{4/3}, \tag{5.10}$$

$$M = \frac{3}{4}\left(\frac{4}{5}\right)^{2/3} {\alpha_{vdp}}^{1/3}\beta^{2/3}y^{5/3} \tag{5.11}$$

and

$$B = \beta y. \tag{5.12}$$

Using the solution for Q in (5.10), which is identical to the two-dimensional stream function χ, we propose a plume boundary condition to be applied in (5.6) of the form

$$\chi = \chi_{vdp} = c_v\beta^{1/3}y^{4/3}, \quad \text{where} \quad c_v = \frac{3}{4}\left(\frac{4}{5}\right)^{1/3} {\alpha_{vdp}}^{2/3}. \tag{5.13}$$

The coefficient in (5.13), evaluated empirically as $c_v = 0.05$ by Cooper & Hunt (2010) (with $\alpha_{vdp} = 0.02$), is in close agreement with $c_v = 0.043 \pm 0.003$ as measured by McConnochie

& Kerr (2016b). The experiments undertaken by the authors to measure these values of c_v are detailed in Chapter 7.

5.2 Solution for the induced flow

We begin by applying the method of separation of variables to identify the general solution to Laplace's equation (5.5). Following Riley et al. (2006), the solution is assumed to be a product of separate functions of the independent variables, r and θ (which originate at the base of the offset plume source), i.e.

$$\chi = R(r)\Phi(\theta). \tag{5.14}$$

Substituting (5.14) into Laplace's equation (5.5) gives

$$\frac{r}{R}\frac{d}{dr}\left(r\frac{dR}{dr}\right) = -\frac{1}{\Phi}\frac{d^2\Phi}{d\theta^2}. \tag{5.15}$$

Evidently, the left-hand side of (5.15) is solely a function of r, and the right-hand side is solely a function of θ. For both sides to be equivalent, the expressions must equate to a constant. Assigning λ^2 as the constant, one can rearrange the expressions and formulate two separate ordinary differential equations,

$$r^2\frac{d^2R}{dr^2} + r\frac{dR}{dr} - \lambda^2 R = 0 \tag{5.16}$$

and

$$\frac{d^2\Phi}{d\theta^2} + \lambda^2\Phi = 0. \tag{5.17}$$

Solving (5.16) and (5.17), we obtain their respective general solutions,

$$R(r) = k_\lambda r^\lambda + l_\lambda r^{-\lambda} \tag{5.18}$$

and

$$\Phi(\theta) = m_\lambda \cos(\lambda\theta) + n_\lambda \sin(\lambda\theta) \tag{5.19}$$

for $\lambda \neq 0$, and

$$R(r) = k_0 \ln r + l_0 \tag{5.20}$$

and

$$\Phi(\theta) = m_0\theta + n_0 \tag{5.21}$$

for $\lambda = 0$. The terms k_λ, l_λ, m_λ and n_λ in (5.18) – (5.21) denote constants. Owing to the linearity of the Laplace equation, we can linearly superpose the solutions (5.18) – (5.21) to form the general solution

$$\chi(r,\theta) = (k_0 \ln r + l_0)(m_0\theta + n_0) + \sum_{\lambda=1}^{\infty} (k_\lambda r^\lambda + l_\lambda r^{-\lambda})[m_\lambda \cos(\lambda\theta) + n_\lambda \sin(\lambda\theta)]. \quad (5.22)$$

To maintain spatial consistency and ensure that the dependent variable is a single-valued function, the constant λ in (5.22) takes positive integer values. We introduce an image polar coordinate system, (r_a, θ_a), in our model, as depicted in figure 5.2, to account for the vertical plume offset. As a consequence, we linearly superpose a second general harmonic solution to (5.22), giving

$$\begin{aligned}\chi(r,\theta,r_a,\theta_a) = {} & (k_0 \ln r + l_0)(m_0\theta + n_0) + \sum_{\lambda=1}^{\infty} (k_\lambda r^\lambda + l_\lambda r^{-\lambda})[m_\lambda \cos(\lambda\theta) + n_\lambda \sin(\lambda\theta)] \\ & + (k_0 \ln r_a + l_0)(m_0\theta_a + n_0) + \sum_{\lambda=1}^{\infty} (k_\lambda r_a^\lambda + l_\lambda r_a^{-\lambda})[m_\lambda \cos(\lambda\theta_a) + n_\lambda \sin(\lambda\theta_a)].\end{aligned} \quad (5.23)$$

To satisfy the boundary conditions (5.6) – (5.8), we match the boundary conditions to the general solution. To model the streamlines representing the horizontal boundary and vertical offset we set k_0, l_0, m_0, n_0, m_λ all to zero, add $\pi/2$ to the argument θ and change its sign, to obtain

$$\chi = n_\lambda \left[(k_\lambda r_a^\lambda + l_\lambda r_a^{-\lambda}) \sin(\lambda\theta_a) - (k_\lambda r^\lambda + l_\lambda r^{-\lambda}) \sin\left(\lambda\left(\theta + \frac{\pi}{2}\right)\right)\right]. \quad (5.24)$$

As a partially-confined problem is considered that is defined in the domain $0 \leq \theta \leq \pi/2$, the solution need not be single-valued. Therefore λ in (5.24) is not restricted to positive integer values. To satisfy the plume boundary condition (5.6) we first set $l_\lambda = 0$ and match the exponent of the local coordinate y in expression (5.13) with that of the global induced flow coordinate r, assigning $\lambda = 4/3$ in (5.24). The resulting expression is then matched with the plume boundary condition (5.13) along the vertical axis above the offset at $\theta = \pi/2$ and $\theta_a = 0$. This gives the solution for the flow induced by a vertically offset distributed plume that is partially-confined by a horizontal boundary as

$$\chi = \frac{3^{1/2}}{2}\left(\frac{4}{5}\right)^{1/3} {\alpha_{\mathrm{vdp}}}^{2/3} \beta^{1/3} \left[{r_a}^{4/3} \sin\left(\frac{4\theta_a}{3}\right) - r^{4/3} \sin\left(\frac{4}{3}\left(\theta + \frac{\pi}{2}\right)\right)\right]. \quad (5.25)$$

In the limiting case when the characteristic length scale $a \to 0$ the origin of the coordinate system (r,θ) and the image system (r_a,θ_a) coincide at the Cartesian axes origin in figure 5.2, and the solution in (5.25) simplifies to

$$\chi = \frac{3}{4}\left(\frac{4}{5}\right)^{1/3} \frac{{\alpha_{\text{vdp}}}^{2/3}}{\sin(4\theta_{\text{vdp}}/3)} \beta^{1/3} r^{4/3} \sin\left(\frac{4\theta}{3}\right) \quad \text{for} \quad 0 \leq \theta \leq \theta_{\text{vdp}}, \tag{5.26}$$

where $\theta_{\text{vdp}} = \pi/2$. The corresponding plane polar velocity components can be derived from (5.26) as

$$u_r = -\frac{1}{r}\frac{d\chi}{d\theta} = -\left(\frac{4}{5}\right)^{1/3} \frac{{\alpha_{\text{vdp}}}^{2/3}}{\sin(4\theta_{\text{vdp}}/3)} \beta^{1/3} r^{1/3} \cos\left(\frac{4\theta}{3}\right) \tag{5.27}$$

and

$$u_\theta = \frac{d\chi}{dr} = \left(\frac{4}{5}\right)^{1/3} \frac{{\alpha_{\text{vdp}}}^{2/3}}{\sin(4\theta_{\text{vdp}}/3)} \beta^{1/3} r^{1/3} \sin\left(\frac{4\theta}{3}\right). \tag{5.28}$$

Taking the square root of the sum of their squares, we obtain the induced flow speed

$$U(r) = |\nabla \times \boldsymbol{\Psi}| = ({u_r}^2 + {u_\theta}^2)^{1/2} = \left(\frac{4}{5}\right)^{1/3} \frac{{\alpha_{\text{vdp}}}^{2/3}}{\sin(4\theta_{\text{vdp}}/3)} \beta^{1/3} r^{1/3}. \tag{5.29}$$

One can also straightforwardly account for the plume width in our solution in (5.26) in instances when the width is significant (e.g. at a large height). Identifying the plume width using (5.10) – (5.11) as

$$b = \frac{Q^2}{M} = \frac{3\alpha_{\text{vdp}}}{4} y, \tag{5.30}$$

which indicates a linear growth, the solution in (5.26) is applied with

$$\theta_{\text{vdp}} = \frac{\pi}{2} - \tan^{-1}\left(\frac{3\alpha_{\text{vdp}}}{4}\right). \tag{5.31}$$

5.3 Analysis of solution

Figure 5.3 is a dimensionless plot of streamlines, $\chi/(a^{4/3}\beta^{1/3}) = const.$, and corresponding contours of constant speed, $U/(a^{1/3}\beta^{1/3}) = const.$ in the induced flow of an offset distributed plume. This (universal) plot is independent of the plume source strength β and the offset distance a. Figures 5.4 (a) and (b) are the corresponding dimensional plots for a plume with a vertical offset of $a = 1$ m and the limiting case when there is no plume offset, respectively. The streamline patterns show the shape of the plume induced flow that is expected to develop, for instance, adjacent to the wall of a large room that is heated by solar radiation. With this

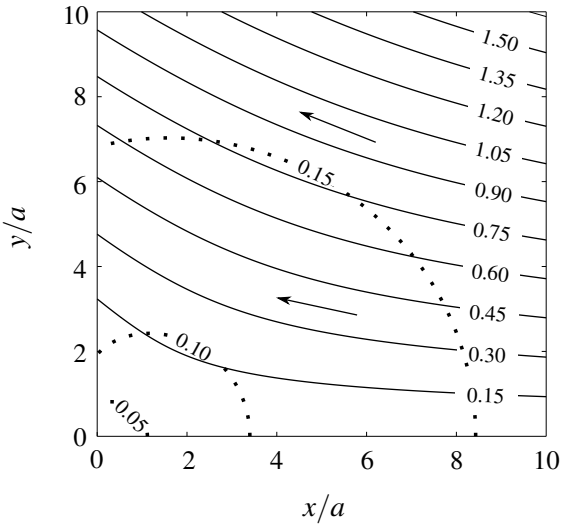

Fig. 5.3 Dimensionless streamlines (solid lines), $\chi/(a^{4/3}\beta^{1/3}) = const.$, and corresponding dimensionless contours of constant speed (dotted lines), $U/(a^{1/3}\beta^{1/3}) = const.$, for the flow induced by a vertically distributed plume offset by a distance a. Values of the stream function and speed corresponding to the contours are overlain. The arrows denote the direction of the induced flow.

example in mind, we have plotted figure 5.4 using a representative source convective heat flux of 1 kW.m^{-2} (Quintiere, 1997, p. 60), which based on expression (5.3) is equivalent to a source buoyancy flux per unit area of $\beta = 0.0281$ m^{2}s^{-2}. This value of β, and the coefficient $\alpha_{\text{vdp}} = 0.02$ measured by Cooper & Hunt (2010), are employed in all successive plots in this chapter unless otherwise stated.

Before analysing the induced flows, consider the perimeter of the plume which has been superposed in figure 5.4 (b). Indeed, an exploded view can be seen of the near-source region in figure 5.5. Here, the streamlines have been overlain by equivalent streamlines (in blue) output upon accounting for the plume width using (5.26). Evidently, the streamlines are graphically indistinguishable. Thus, we can conclude that approximating the plume as a vertical line is a reasonable approximation when modelling the induced flow. One should, however, ensure that the region of interest falls outside of the plume perimeter, defined using (5.30), when using the solution.

Immediately evident from figures 5.3 and 5.4 is the upward inclination of the induced flow. This is a consequence of the plume's vertical entrainment demand increasing with

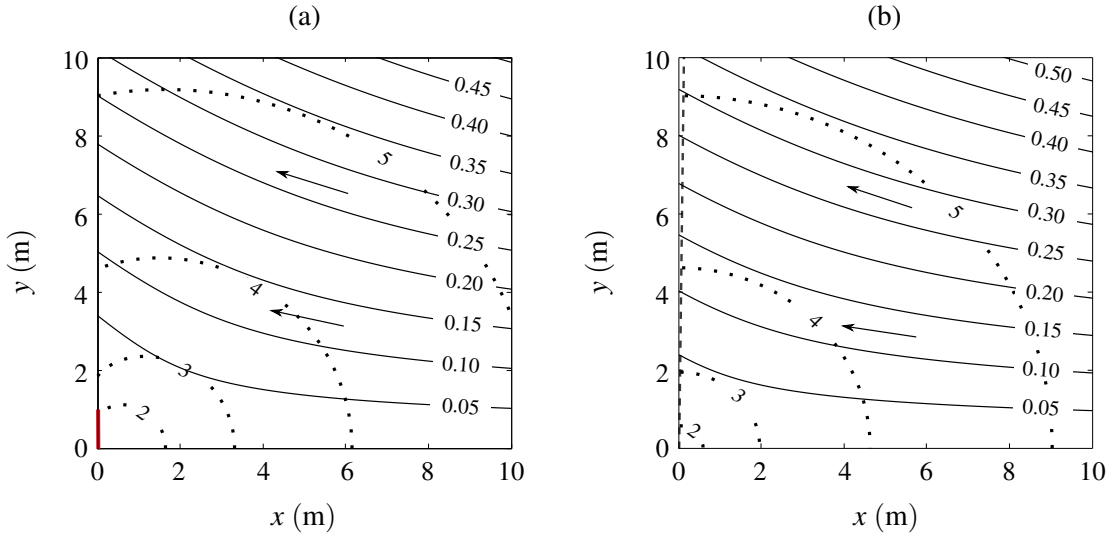

Fig. 5.4 Streamlines (solid lines), $\chi = const.$, and corresponding contours of constant speed (dotted lines), $U = const.$ $(\times 10^{-2})$ ms^{-1}, in the induced flow of a vertically distributed plume with source strength 1 kW.m^{-2} with (a) a vertical offset of $a = 1$ m (highlighted in red) and (b) no offset. The values of the stream function and speeds are overlain. The perimeter of the plume (dashed line) has been superposed in (b). The arrows denote the direction of the induced flow.

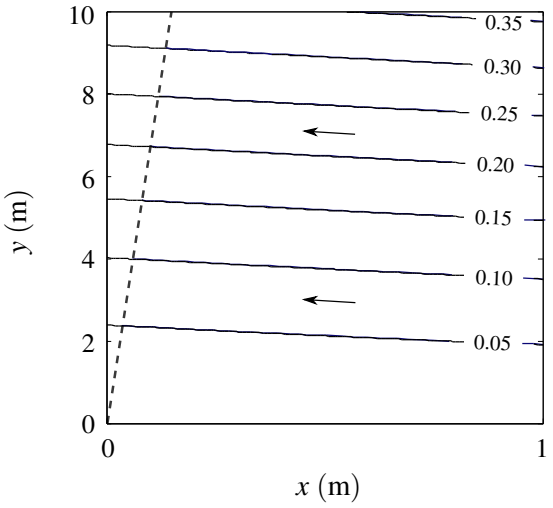

Fig. 5.5 Comparison of the streamline portraits for the flow induced by a distributed plume with zero offset upon approximating the plume as having zero width using expression (5.25) (in black) and accounting for the linear increase in the width of the plume (in blue). The blurred appearance of the streamlines is due to the streamlines lying almost on top of one another. The arrows indicate the general direction of flow.

height. Differentiating (5.10) with respect to y, this demand may be expressed as

$$\frac{dQ}{dy} = u_e = \alpha_{vdp}\frac{M}{Q} = \left(\frac{4}{5}\right)^{1/3} {\alpha_{vdp}}^{2/3}\beta^{1/3}y^{1/3}. \tag{5.32}$$

Buoyancy, which is continuously input over the entire height of the source, generates a buoyancy-induced momentum flux in the plume M, expressed in (5.11), that increases vertically at a faster rate than the corresponding volume flux Q (5.10). As the plume's entrainment velocity u_e is proportional to the local ratio, M/Q, it also increases with height. To satisfy this increasing vertical entrainment demand, fluid at a lower elevation in the induced flow compensates and diverts its course along an upwardly inclined trajectory, as opposed to maintaining a horizontal flow with large vertical velocity gradients. Along the rising path towards the plume, the induced flow also noticeably steepens, with streamlines measured directly from figure 5.4 (b) to have an inclination with the horizontal of $\theta_p = 30^\circ$ at the plume perimeter — a value which is independent of height. It is evident from figure 5.4 (a) that this inclination is more pronounced for a distributed plume with an offset, and further, from the scalings in figure 5.3 the inclination is greater at a given height for a plume with a larger offset.

Contours of constant speed are overlain in figures 5.3 and 5.4. The plume with zero offset in figure 5.4 (b) has contours, plotted using (5.29), that form concentric quarter circles about the base of the source. Each contour is independent of the azimuthal angle θ, in contrast to the equivalent contours of constant speed in figures 5.3 and 5.4 (a), which are asymmetric as a result of the plume offset. The increasing speeds with distance from the origin in the induced flow is a result of the entrained velocity (5.32) continuously increasing with height. To feed the entrainment demand in the limit of an infinite height, a source singularity is formed at an infinite distance from the base of the source. Speeds in the induced flow continuously increase away from the plume source towards this singularity.

The presence of a singularity may lead readers to question the practicality of the induced flow solution derived, particularly as buoyancy cannot be input over an infinite extent in reality. To address this issue, consider the more realistic scenario of a source with a finite height. In this instance, the (finite) source height becomes a relatively diminishingly small length compared to the vertical coordinate y as $y \to \infty$. In the vertical limit of an infinite height, the relative source height is infinitesimal. Therefore, here the distributed plume behaves as a pure plume above a line source, and locally induces a flow with a constant speed (see Chapter 2). Owing to the elliptic nature of the governing equation, this far-field behaviour also dictates the induced flow field at a large radial distance from the base of the plume source. Crucially, any modification to the plume boundary condition beyond a given height will only affect the induced flow field in the vicinity of the azimuthal curve along the corresponding radial distance from the base of the source and beyond. This highlights that when considering a plume source with a finite height, our induced flow solution (corresponding to a source of infinite height) remains accurate in the near-field as long as the source height is large in comparison to the dimensions of the induced flow region considered.

The contours of constant speed that are overlain onto the streamlines in figures 5.3 and 5.4 shed light on the flow characteristics of the induced flow. We observe that streamlines have a concave nature, whilst contours of constant speed have a convex form. Interestingly, this implies that the acceleration of fluid particles in the induced flow changes sign — as we shall see below, particles accelerate following an initial period of deceleration along their trajectories. This suggests (from volume conservation) that the spacing between adjacent streamlines increases and then decreases towards the source, which can be observed upon closer inspection of figures.

To provide insight into the aforementioned behaviour, we reanalyse the flow using a Lagrangian framework, where individual induced flow fluid particles are followed, as opposed to considering Eulerian control volumes. Focussing on the plume with zero offset ($a = 0$), we

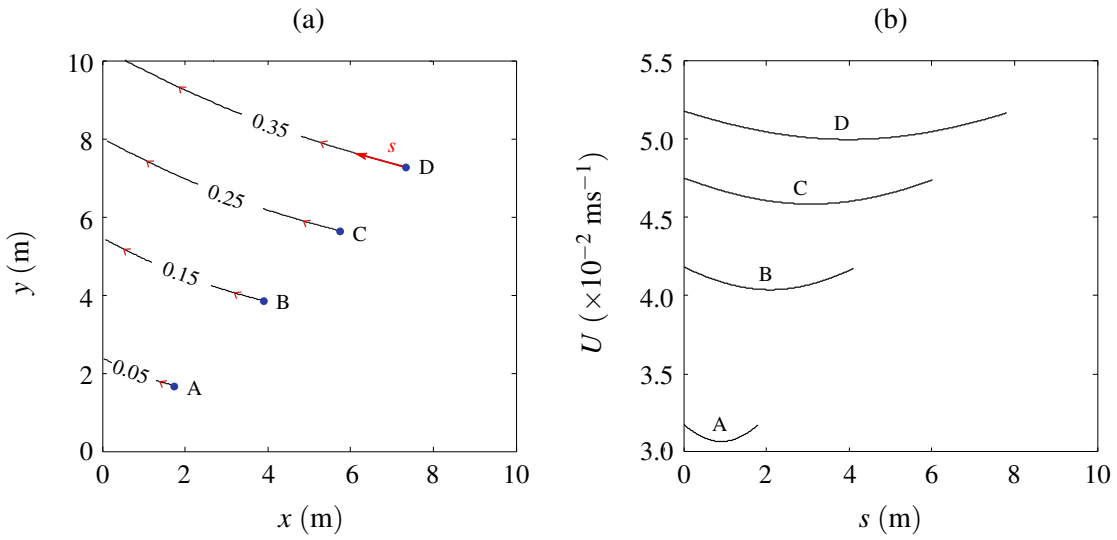

Fig. 5.6 (a) The trajectories of four fluid particles (A, B, C and D) initially placed at locations along $\theta = \pi/4$ in the induced flow of the vertically distributed plume. These trajectories correspond to the streamlines $\chi = 0.05$, 0.15, 0.25 and 0.35 $\mathrm{m^2 s^{-1}}$ in figure 5.4 (b). The red arrows indicate the direction of motion of each particle. (b) The speed of each fluid particle U as it moves along each of the trajectories, with s denoting the distance along each trajectory from the particle's initial position.

reframe expressions (5.27) and (5.28) corresponding to induced flow velocity components, as

$$\frac{dr_{\mathrm{pc}}}{dt} = u_{r_{\mathrm{pc}}} = -\left(\frac{4}{5}\right)^{1/3} \frac{{\alpha_{\mathrm{vdp}}}^{2/3}}{\sin(4\theta_{\mathrm{vdp}}/3)} \beta^{1/3} {r_{\mathrm{pc}}}^{1/3} \cos\left(\frac{4\theta_{\mathrm{pc}}}{3}\right) \tag{5.33}$$

and

$$\frac{d\theta_{\mathrm{pc}}}{dt} = \frac{u_{\theta_{\mathrm{pc}}}}{r_{\mathrm{pc}}} = \left(\frac{4}{5}\right)^{1/3} \frac{{\alpha_{\mathrm{vdp}}}^{2/3}}{\sin(4\theta_{\mathrm{vdp}}/3)} \beta^{1/3} {r_{\mathrm{pc}}}^{-2/3} \sin\left(\frac{4\theta_{\mathrm{pc}}}{3}\right), \tag{5.34}$$

respectively (where the subscript '$(\cdot)_{\mathrm{pc}}$' corresponds to a particle). Expressions (5.33) and (5.34) enable the positions (r_{pc}, θ_{pc}) of a particle in the induced flow to be determined at each instant in time from a given initial position. By definition, the trajectory of a particle will correspond to a streamline. Figure 5.6 (a) presents the trajectories of four particles A, B, C and D in the induced flow, initially placed along $\theta = \pi/4$, determined upon (numerically) solving the system of non-linear ODEs (5.33) and (5.34).

The speed of each fluid particle in figure 5.6 (a) can be predicted upon inputting the coordinates that have been output from (5.33) and (5.34) into expression (5.29). One can

also evaluate the distance s along a particle's trajectory using

$$s = \int_{\theta_i}^{\theta_{pc}} \left({r_{pc}}^2 + \left(\frac{dr_{pc}}{d\theta} \right)^2 \right)^{1/2} d\theta, \tag{5.35}$$

where θ_i and θ_{pc} denote the angular coordinates of the initial position and a given position along an induced flow particle's path, respectively. Figure 5.6 (b) represents the corresponding speeds U of the four particles in figure 5.6 (a) along their trajectories s. Evidently, there is a turning point, specifically a local minima, in each profile. Moreover, particles have a reduced acceleration and deceleration, but larger variation in speed along their paths with increasing height.

Our attention now turns to identifying the precise location in the environment at which the transition from a decelerating to accelerating regime occurs. First, we focus on a given streamline, by equating the stream function in (5.26) to a constant value μ, giving

$$\frac{3}{4}\left(\frac{4}{5}\right)^{1/3} \frac{{\alpha_{vdp}}^{2/3}}{\sin(4\theta_{vdp}/3)} \beta^{1/3} r^{4/3} \sin\left(\frac{4\theta}{3}\right) = \mu. \tag{5.36}$$

The position at which the acceleration of the fluid particles changes sign is where their speed is either a local minimum or maximum. Based on the physical arguments earlier, the speed reaches a local minimum. By identifying that the speed in the induced flow, illustrated in figure 5.4 (b), is solely a function of the radial coordinate r (see (5.29)), and increases with r, we seek the location along each streamline where the radial coordinate is minimised. A global locus can be identified once such a position is determined across all streamlines. To identify the location where the radial coordinate is minimised along a given streamline, we rearrange expression (5.36) in terms of r, to give

$$r = \left[\frac{3}{4\mu}\left(\frac{4}{5}\right)^{1/3} \frac{{\alpha_{vdp}}^{2/3}}{\sin(4\theta_{vdp}/3)} \beta^{1/3} \sin\left(\frac{4\theta}{3}\right) \right]^{-3/4}. \tag{5.37}$$

Equation (5.37) is then differentiated with respect to θ and equated to zero, resulting in

$$\frac{dr}{d\theta} = -\left\{ \left[\frac{1}{\mu}\left(\frac{3}{4}\right)^{10/3} \left(\frac{4}{5}\right)^{1/3} \frac{{\alpha_{vdp}}^{2/3}}{\sin(4\theta_{vdp}/3)} \beta^{1/3} \right]^{3/7} \sin\left(\frac{4\theta}{3}\right) \right\}^{-7/4} \cos\left(\frac{4\theta}{3}\right) = 0. \tag{5.38}$$

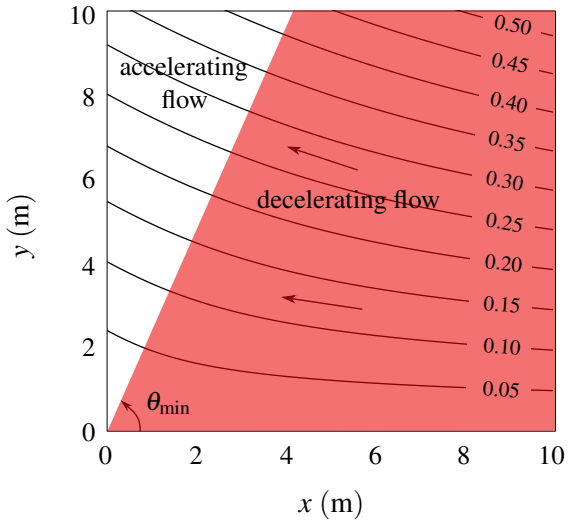

Fig. 5.7 Locus $\theta_{\min} = 3\pi/8$ separating the induced flow into regions where fluid is decelerating (in red) and accelerating.

Solving expression (5.38) for θ, we derive the periodic solution,

$$\theta = \frac{3\pi}{8}(2n-1), \tag{5.39}$$

from which we select the first root ($n = 1$) to give $\theta = \theta_{\min} = 3\pi/8$. This result signifies that fluid moving along a given streamline in the induced flow will undergo a transition from deceleration to acceleration once it encounters the locus at $\theta = 3\pi/8$. The position of the locus is depicted in figure 5.7, where it has been superposed onto the streamline portrait of the plume induced flow from figure 5.4 (b).

5.3.1 Effect of source strength

Thus far our focus has been on understanding flow features in the plume induced flow, with little emphasis placed on the role of the plume's source strength, i.e. of the source buoyancy flux per unit area β. Figure 5.8 presents the induced flow speeds for a plume with zero offset along the horizontal boundary and at a height of $y = 1.5$ m, for a range of plume source strengths. In the context of a room, $y = 1.5$ m corresponds to the approximate head height of an occupant. The source strengths are increased in unit increments of $\beta = 0.0281$ m^2 s^{-2} up to 5β. In general, we observe from the spacing between adjacent curves, that the incremental increase in the induced flow speed U diminishes with source strength β, note $U \propto \beta^{1/3}$ from (5.29). It is also evident that the speed of the induced flow along the horizontal boundary

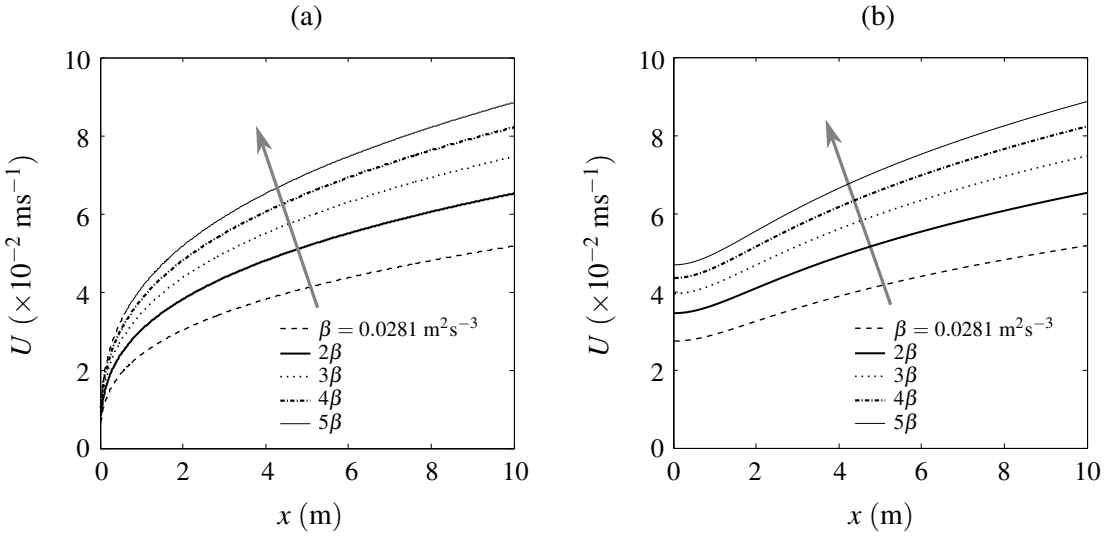

Fig. 5.8 Induced flow speeds for a plume with zero offset (a) along the horizontal boundary and (b) at a height $y = 1.5$ m for source strengths $\beta = 0.0281$ m^{2}s^{-3}, 2β, 3β, 4β and 5β. The arrows indicate the direction of increasing source strength.

has a steep gradient close to the source. This is a consequence of the fact that the horizontal velocity $u_e = 0$ at the base of the plume.

5.3.2 Effect of source offset

In figure 5.9 we illustrate the variation in speed along the horizontal boundary of the induced flow as a function of the plume offset. Increasing the plume offset results in lower induced flow speeds being induced at a given position along the horizontal boundary. The speeds are also less sensitive to any change in the offset when the base of the plume is at a greater height.

5.3.3 Application

In this section we investigate the speeds induced using our induced flow solution in an application in the built environment alternative to that of the solar patch on the wall of a room considered earlier. Consider the lobby of a large building with a glass façade exposed to the outdoor environment. On a cold morning, a downward flowing vertically distributed plume develops adjacent to this façade inside the lobby and induces a flow. Let us consider, for instance, the situation where the temperature outside is -5 °C, and approximately 20 °C inside the lobby. Taking the heat transfer coefficient of (single-glazed) glass as $h = 6$

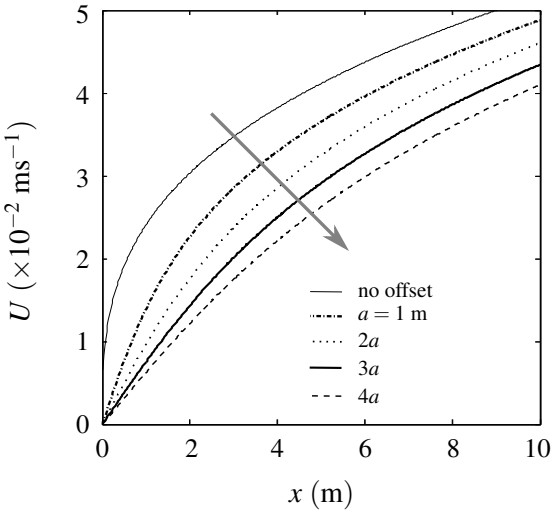

Fig. 5.9 Speeds of the flow induced along the horizontal boundary by a vertically distributed plume with offsets $a = 0, 1$, 2, 3 and 4 m. The arrow indicates the direction of increasing magnitude of the offset.

Wm^{-2}.$^{\circ}C^{-1}$ (Rubin, 1982), we estimate the heat flux through the façade as $H = h\Delta T = 25 \times 6 = 150$ Wm^{-2}. Utilising equation (5.3), this heat flux is equivalent to a source buoyancy flux per unit area input of $\beta = 0.0042$ m^{2}s^{-3} (4 d.p.). Using this source strength, together with $\alpha_{\text{vdp}} = 0.02$, in the expression for speed (5.29), we predict that $U = 1.9 \times 10^{-2}$ ms^{-1} at a 1.5 m height and horizontally 3 m from the façade. This speed is approximately 3% of that in the plume at that height. In this application, the flow speeds predicted are below background air speeds of circa 0.1 ms^{-1} that are commonplace in occupied spaces (Melikov et al., 1988).

Whilst a natural next step of the work is to provide validation for the model, the literature focusses on filling boxes, with experiments (discussed in Chapter 7) undertaken within the confines of a tank where stratification and the solid boundaries influence the pattern of flow induced. For these reasons, the solution, which has been formulated in a uniform environment, cannot at present be compared to empirical measurements.

5.4 Conclusions

An analytical solution for the flow induced by a partially-confined, vertically distributed plume has been developed. The model enables us to predict the shape of and speeds in the induced flow.

In the absence of a characteristic length scale in the problem, we force a length scale via a vertical plume offset $a \neq 0$ from a horizontal boundary, and model the induced flow in this more general case. Our original problem can be viewed as the limiting case when $a \to 0$. The analytical solution derived indicates that the induced flow follows an increasingly (upwardly) inclined path towards the plume. The flow attains an inclination in the case of a plume with no offset of $\theta_p = 30^\circ$ at the plume perimeter. The flow shape is a consequence of the increasing vertical entrainment demand of the plume. Specifically, fluid particles at a lower elevation divert their course along an upward path to meet the demand. This flow pattern is analogous to the flow induced by the lazy plume above a horizontal slot modelled in the previous chapter, though the inclination is more pronounced here due to the stronger vertical gradient in the entrainment velocity. Particles in the induced flow of the distributed plume decelerate and then accelerate along their path towards the plume. When the plume has a zero offset, this transition has been predicted to occur once the particles cross the locus at $\theta = 3\pi/8$.

The vertically distributed plume and lazy plume above a horizontal slot, considered in the current and previous chapters, respectively, are flows that have a relative excess in buoyancy flux. In the following chapter, we derive the complementary induced flow solution for the forced plume above a slender horizontal slot. In contrast to the corresponding lazy plume, the forced plume has a relative deficit in buoyancy flux (or equivalently a relative excess in momentum flux) supplied at the source.

Chapter 6

Flows induced by forced plumes

To provide a comprehensive understanding of the role that plume source conditions, and specifically the (relative) forcing at the source, has on the flow induced above a slender horizontal slot, in this chapter, we devise a solution for the flow induced by the forced plume ($0 < \Gamma_0 < 1$). The solution supplements the models for the flow induced by the pure plume ($\Gamma_0 = 1$) and contracting lazy plume ($\Gamma_0 > 2$) developed in Chapters 2 and 4, respectively.

Forced plumes are widespread in the environment. Examples include the coalesced flow rising above a row of closely spaced industrial chimney stacks, and the effluent released from multi-port diffusers following the waste-water treatment process (see Adams & Trowbridge (1985)). Forced plumes have markedly different dynamics to their pure plume and contracting lazy plume counterparts in the near-source region, as they have a greater forcing, or equivalently a relative excess in momentum flux M_0, at their source. The increased forcing drives a straight-sided plume that continously widens with height above the source, as shown by the measurements plotted in figure 3 (b) in Kotsovinos & List (1977). A local vertical flow transition occurs in the forced plume towards a pure plume regime. This occurs at a slower rate in comparison to the lazy plume, owing to the relative deficit of buoyancy flux supplied at the source. Morton (1959) undertook one of the earliest studies explicitly focussed on forced plumes. He represented the forced plume above a non-idealised source (with finite fluxes of volume, momentum and buoyancy) in a uniform environment using a virtual source of buoyancy and momentum only, located at some vertical distance below the actual source. Morton & Middleton (1973) later developed their so-called 'scale diagrams' to gain further insight into forced plumes based on the work of Morton (1959). These dimensionless plots show various characteristic heights, including the location of the virtual source, as a function of the source Richardson number Γ_0. The work of the aforementioned authors, which focussed on axisymmetric forced plumes above circular sources, has been

extended more recently by van den Bremer & Hunt (2014) where they apply the Γ-centred approach of Hunt & Kaye (2005) to the plumes above slender horizontal slots. Following the early developments of Morton (1959) and Morton & Middleton (1973), work conducted on forced plumes has largely centred on modelling plume entrainment (Priestley & Ball, 1955; List & Imberger, 1973, 1975; Yannopoulos & Noutsopoulos, 1990; Wang & Law, 2002), an aspect of forced plumes discussed in §6.1. A search of the literature reveals that no studies have focussed on the induced flow of the forced plume.

In this chapter, we model the flow induced by the forced plume to complement the induced flow solutions derived in previous chapters, build on our current understanding of forced plumes attained from the literature, and to gain insight into an aspect of forced plumes of which we currently have little knowledge. Following the general approach of Taylor (1958), the induced flow is modelled as an inviscid potential flow governed by the Laplace equation subject to boundary conditions representing the forced plume and horizontal boundary. The horizontal boundary is modelled as a streamline. The plume boundary condition is modelled using the formulation from van den Bremer & Hunt (2014). Given the plume is straight-sided and it is as straightforward to enforce the boundary condition along the actual plume perimeter as on the vertical axis using our solution technique (the latter as done by Taylor (1958)), the boundary condition is imposed on the plume perimeter.

In §6.1 we begin by developing the plume boundary condition and subsequently defining the governing boundary value problem for the flow induced by the forced plume. Unlike the boundary condition for the vertically distributed source which takes a self-similar form, the boundary condition for the forced plume is complicated by comparison. As a consequence, this chapter reverts to deriving the solution in the complex plane rather than using the method of separation of variables. In §6.2 we devise the conformal mapping that maps between the upper-half plane and the induced flow region. Following this, we derive the solution for the induced flow in §6.3, and analyse the solution in §6.4. In §6.4.1 we consider the validity of the solution in the limiting case of the jet ($\Gamma_0 = 0$) and compare it to the corresponding idealised solution presented in Chapter 2. The 'Velocity Ratio' diagnostic, introduced in Chapter 3, is applied to compare the effects that a forced plume and lazy plume have on their environments in §6.5. Conclusions are drawn in §6.6.

6.1 Plume boundary condition for $0 < \Gamma_0 < 1$

Thus far the entrainment model, $u_e = \alpha w$ (Taylor, 1945), has been employed with a constant value of α. The average value of the entrainment coefficient for the (pure) plume, $\alpha_p = 0.13$

(upon averaging the measurements of Kotsovinos (1975), Lee & Emmons (1961), Yuana & Cox (1996)), is considerably larger than the corresponding average value for the jet, $\alpha_j = 0.05$ (based on measurements from Kotsovinos (1975), Chen & Rodi (1980), Antonia et al. (1983)) (see Chapter 2). The larger value of α measured for the plume is attributed to the contribution of buoyancy to the flow's turbulent energy, and a build up of 'eddies' to the scale of the width of the plume flow to create large-scale engulfment of ambient fluid (Kotsovinos, 1977). These inferences are confirmed by turbulence intensity measurements of velocity and temperature fluctuations across the jet and plume flows from Kotsovinos (1977). Specifically, the fluctuations remain constant across the width of the plume, in contrast to the jet which exhibits peaks close to the flow perimeter, and moreover, turbulence intensity measurements of temperature and velocity (taken at a specified downstream location) have a greater magnitude of circa a factor 1.5 and 2, respectively, in the plume compared with the jet (cf. figures 6, 7 and 17 in Kotsovinos (1977)). The approximate factor 2.5 difference (with a range from an upper bound of 4 to a lower bound of 1.7 based on the individual measurements) between α_p and α_j makes it difficult to justify using a universal constant for α when modelling the forced plume, which corresponds to the regime between the two pure limits. Moreover, selecting a constant value for α implies that the jet spreads at twice the rate of the pure plume, a feature which is inconsistent with observations that indicate equal spreading rates (Fischer et al., 1979). As a consequence of these shortcomings, List & Imberger (1975) proposed the entrainment model,

$$\alpha = \alpha_j + (\alpha_p - \alpha_j)\Gamma = \alpha_p(\kappa + (1-\kappa)\Gamma) \quad \text{for} \quad 0 < \Gamma < 1, \tag{6.1}$$

where the ratio of the entrainment coefficients $\kappa = \alpha_j/\alpha_p$ and Γ denotes the local plume Richardson number which for Gaussian profiles is defined as

$$\Gamma = \frac{1}{2^{3/2}\alpha_p}\frac{BQ^3}{M^3}. \tag{6.2}$$

Note that the coefficient in (6.2) is defined using the pure plume entrainment coefficient α_p. Crucially, the model in (6.1) attains the respective jet and plume entrainment coefficients in the forced plume limits, when $\Gamma = \Gamma_0 = 0$ and $\Gamma = \Gamma_0 = 1$, respectively, and applies a simple linear model to describe the entrainment behaviour between. The use of this and other entrainment models are discussed in Chapter 7.

van den Bremer & Hunt (2014) adopt the linear entrainment model (6.1) to formulate a governing system of equations to describe the forced plume. Specifically, the equations are formulated therein with (6.1) using the Γ-centred approach (outlined in Chapter 2), and

expressed in terms of the dimensionless parameters; the Richardson number Γ (6.2), the half-width $\bar{b} = b(\zeta)/b_0$ and the centre-line velocity $\bar{w} = w_{\mathrm{m}}(\zeta)/w_0$, where b_0 and w_0 refer to the source half-width and centre-line velocity, respectively. The governing equations are

$$\frac{d\Gamma}{d\zeta} = \frac{3\kappa\Gamma(1-\Gamma)}{\bar{b}}, \quad \frac{d\bar{b}}{d\zeta} = 2\kappa - (2\kappa-1)\Gamma, \quad \frac{d\bar{w}}{d\zeta} = \frac{\bar{w}\kappa}{\bar{b}}(\Gamma-1). \tag{6.3}$$

The dimensionless vertical and horizontal coordinates are scaled on the source width as

$$\zeta = \frac{2\alpha_{\mathrm{p}}}{\pi^{1/2}b_0}y \quad \text{and} \quad \Delta = \frac{2\alpha_{\mathrm{p}}}{\pi^{1/2}b_0}x, \tag{6.4}$$

respectively. With reference to (4.5), we note this is an identical scaling as for the lazy plume induced flow in Chapter 4. The corresponding source conditions for the forced plume are

$$\Gamma = \Gamma_0, \quad \bar{b} = 1, \quad \bar{w} = 1 \quad \text{at} \quad \zeta = 0, \tag{6.5}$$

where $0 < \Gamma_0 < 1$. van den Bremer & Hunt (2014) solve the system of equations in (6.3), subject to (6.5), to obtain solutions for the plume width and centre-line velocity,

$$\bar{b} = \left(\frac{\Gamma}{\Gamma_0}\right)^{2/3}\left(\frac{1-\Gamma_0}{1-\Gamma}\right)^{1/(3\kappa)}, \quad \bar{w} = \left(\frac{\Gamma_0}{\Gamma}\right)^{1/3}, \tag{6.6}$$

respectively, with

$$\frac{d\Gamma}{d\zeta} = 3\kappa\Gamma(1-\Gamma)\left(\frac{\Gamma_0}{\Gamma}\right)^{2/3}\left(\frac{1-\Gamma}{1-\Gamma_0}\right)^{1/(3\kappa)}. \tag{6.7}$$

With $\kappa = 1/2$ we get the original model proposed by Priestley & Ball (1955). Imposing a value of $\kappa = 1/2$, van den Bremer & Hunt (2014) reduce the solutions in (6.6) and (6.7) to

$$\bar{b} = 1+\zeta, \quad \Gamma = \left(1+\frac{1-\Gamma_0}{\Gamma_0}(1+\zeta)^{-3/2}\right)^{-1}, \quad \bar{w} = (\Gamma_0+(1-\Gamma_0)(1+\zeta)^{-3/2})^{1/3}. \tag{6.8}$$

The solution for $\bar{b}$ indicates that the plume is straight-sided, as observed in the experiments of Kotsovinos & List (1977). The value $\kappa = 1/2$ is also consistent with measurements indicating that the plume entrainment coefficient α_{p} is approximately twice as large as that of the jet entrainment coefficient α_{j}. The solution in (6.8) is independent of Γ_0, implying that the plume boundary condition is to be applied along a fixed perimeter. To formulate the forced plume boundary condition, we first note the equivalence between the dimensionless

volume flux and stream function,

$$q = \frac{Q}{Q_0} \equiv \Psi = \frac{\chi}{\chi_0}, \tag{6.9}$$

with $\Psi = 1$ at the plume source. Noting that $q = \bar{b}\bar{w}$, using (6.8) gives

$$q = (\Gamma_0(1+\zeta)^3 + (1-\Gamma_0)(1+\zeta)^{3/2})^{1/3}. \tag{6.10}$$

In the limits of the pure jet ($\Gamma_0 = 0$) and pure plume ($\Gamma_0 = 1$), (6.10) reduces to

$$q = (1+\zeta)^{1/2} \quad \text{and} \quad q = (1+\zeta), \tag{6.11}$$

respectively. The vertical gradient of q in (6.10), or equivalently twice the scaled entrainment velocity, is given by

$$\frac{dq}{d\zeta} = \frac{u_\mathrm{e}}{\alpha_\mathrm{p} w_0} = \frac{3\Gamma_0(1+\zeta)^2 + (3/2)\cdot(1-\Gamma_0)(1+\zeta)^{1/2}}{3(\Gamma_0(1+\zeta)^3 + (1-\Gamma_0)(1+\zeta)^{3/2})^{2/3}}. \tag{6.12}$$

With the induced flow modelled on only one side of the plume due to the symmetry about the plume's centre-line, we halve the volume flux in (6.10), and use the equivalence between q and Ψ in (6.9), to define a boundary condition for the forced plume

$$\Psi = \Psi_\mathrm{fp} = \frac{1}{2}\left(\Gamma_0(1+\zeta)^3 + (1-\Gamma_0)(1+\zeta)^{3/2}\right)^{1/3} \quad \text{along} \quad \Delta = \Delta_\mathrm{fp} = \frac{2\alpha_\mathrm{p}\bar{b}(\zeta)}{\pi^{1/2}}. \tag{6.13}$$

The subscript '$(\cdot)_\mathrm{fp}$' in (6.13) denotes 'forced plume'. As outlined in Chapter 4, Poisson's theorem requires that boundary conditions remain bounded. Expression (6.13) fails to satisfy this criterion, as it maintains non-zero velocities in the induced flow at an infinite height above the source. In practice, velocities in a plume will become indistinguishable from background air disturbances at sufficiently large heights. To capture this behaviour and simultaneously achieve boundedness, we continuously reduce the (positive) gradient of the stream function Ψ in (6.13) above some height, and crucially, ensure that this local gradient, which is equivalent to the local entrained velocity, reaches zero at or below an infinite height. Enforcing an identical rate of increase in the stream function to that in (4.19) for the lazy plume, reasonable given this is imposed at large height where the plume is approximately

pure, the modified plume boundary condition takes the form

$$\Psi(\zeta) = \Psi_{\rm fp}(\zeta) = (1/2)\cdot \mathrm{H}(\zeta_L - \zeta)\left(\Gamma_0(1+\zeta)^3 + (1-\Gamma_0)(1+\zeta)^{3/2}\right)^{1/3} + \\ \mathrm{H}(\zeta-\zeta_L)\left[(1/2)\cdot\left(\Gamma_0(1+\zeta_L)^3 + (1-\Gamma_0)(1+\zeta_L)^{3/2}\right)^{1/3} + 1 - e^{-(\zeta-\zeta_L)}\right] \tag{6.14}$$

along $\Delta = \Delta_{\rm fp}$ for $\zeta \geq 0$. In (6.14) the term ζ_L is the non-dimensional height beyond which the decay of the entrainment velocities is imposed. The Heaviside step function H in (6.14) ensures that the decay only occurs above the height $\zeta_{\rm L}$, which is selected to be sufficiently large so as not to affect the induced flow solution in our region of interest close to the source.

In summary, we require a solution of

$$\nabla^2\Psi = \frac{\partial^2\Psi}{\partial\Delta^2} + \frac{\partial^2\Psi}{\partial\zeta^2} = 0 \quad \text{for} \quad \Delta_{\rm fp} \leq \Delta < \infty, \quad 0 \leq \zeta < \infty, \tag{6.15}$$

that satisfies the plume boundary condition in (6.14), and

$$\Psi = 1/2 \quad \text{on} \quad \zeta = 0 \quad \text{for} \quad \Delta \geq \Delta_{\rm fp}(0) = \frac{2\alpha_{\rm p}}{\pi^{1/2}}. \tag{6.16}$$

6.2 The conformal mapping

Poisson's theorem (2.27) guarantees a solution to Laplace's equation in the upper-half complex plane, subject to specifying appropriate (bounded) boundary conditions along the real-axis (Paliouras & Meadows, 1990). To exploit Poisson's theorem, we require a conformal mapping that maps between the upper-half plane and the region occupied by the induced flow of the forced plume. We propose the (inverse) mapping,

$$\omega = z^{\gamma} + a_{\rm h}, \tag{6.17}$$

which maps from the upper-half Z-plane to the induced flow region in the W-plane. Here, the translation $a_{\rm h}$ accounts for the plume source width, and the exponent γ specifies the internal angle, $\gamma\pi$, of the (straight-sided) wedge that is the induced flow region. Note that expression (6.17) corresponds to the mapping employed when modelling the flow induced by the lazy plume (4.26) with $a_{\rm v} = 0$. The parameter $a_{\rm v}$, which in Chapter 4 ensured that the real axis of the Z-plane mapped to the curved perimeter of the contracting lazy plume, takes a value of zero here, as the forced plume is straight-sided. With reference to (6.17), the corresponding

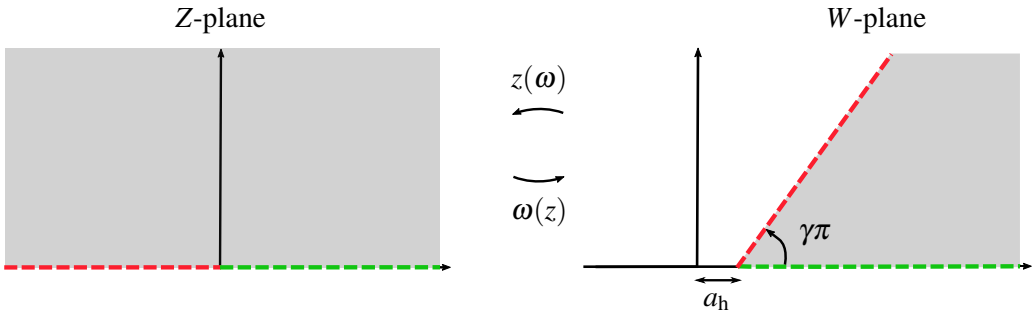

Fig. 6.1 The forward conformal mapping, $z(\omega) = (\omega - a_h)^{1/\gamma}$, and its corresponding inverse mapping, $\omega(z) = z^\gamma + a_h$, between the (shaded) upper-half Z-plane and induced flow region in the W-plane internal to a straight-sided wedge. The dashed lines represent boundaries of the two regions. The colours highlight corresponding locations along the boundaries upon applying the mappings.

forward mapping, mapping from the induced flow in the W-plane to the upper-half Z-plane, is

$$z = (\omega - a_h)^{1/\gamma}. \tag{6.18}$$

Figure 6.1 illustrates the (shaded) regions corresponding to the upper-half Z-plane and the induced flow region in the W-plane between which the functions (6.17) and (6.18) map. The dashed lines denote the boundaries of the two regions, with the colours indicating the corresponding locations upon applying the mappings.

Based on the expression derived for the plume width, $\bar{b} = 1 + \zeta$ (6.8), we identify that the interior angle $\gamma\pi = \tan^{-1}(\zeta/\Delta(b)) = 0.454\pi$. Therefore the mapping parameter $\gamma = 0.454$. The horizontal translation corresponds to the half-width of the plume source and thus takes a value of $a_h = \Delta(b_0) = 2\alpha_p/\pi^{1/2}$. Employing the aforementioned values of the constants, the mappings (6.17) and (6.18) are known. Note the mappings are independent of Γ_0.

6.3 Solution for the induced flow

Poisson's theorem (2.27), the forward map in (6.18), and its inverse in (6.17), can now be applied to derive the solution for the flow induced by the forced plume.

Mapping using (6.18) from the W- to the Z-plane, we identify the locations along the real axis of the Z-plane along which the boundary conditions are applied. This enables us to specify the input into Poisson's theorem, as

$$f(\tau,0) = f(\eta,0) = \begin{cases} \Psi_{fp} & \text{for} \quad \eta = [-\infty, 0] \\ 1/2 & \text{for} \quad \eta = [0, \infty] \end{cases} \tag{6.19}$$

where η denotes the real coordinate in the Z-plane. Decomposing Poisson's theorem into the sum of two integrals to account for each of the boundary conditions in (6.19), we derive the solution

$$f(\eta,\xi) = \int_{-\infty}^{0} P(\eta-\tau)\Psi_{\rm fp}(\mathrm{Im}[\omega(\tau)])\,d\tau + \frac{1}{2}\int_{0}^{\infty} P(\eta-\tau)\,d\tau \tag{6.20}$$

where

$$P(\eta) = \frac{\pi^{-1}\xi}{\eta^2+\xi^2} \tag{6.21}$$

in the upper-half Z-plane. The limits of the integrals here correspond to the intervals (along the real axis) over which each boundary condition in (6.19) is applied, and the argument of $\Psi_{\rm fp}$ denotes the vertical coordinate in the W-plane. Evaluating the second integral in (6.20)

$$f(\eta,\xi) = \int_{-\infty}^{0} P(\eta-\tau)\Psi_{\rm fp}(\mathrm{Im}[\omega(\tau)])d\tau + \frac{1}{4} + \frac{1}{2\pi}\tan^{-1}\left(\frac{\eta}{\xi}\right) \tag{6.22}$$

To determine the solution in the original induced flow domain, we map the coordinates of the solution in (6.22) back to the W-plane, to give

$$\begin{aligned}\Psi(\Delta,\zeta) &= F^{-1}(f(\eta,\xi)) \\ &= F^{-1}\left\{\int_{-\infty}^{0} P(\eta-\tau)\Psi_{\rm fp}(\mathrm{Im}[\omega(\tau)])\,d\tau + \frac{1}{4} + \frac{1}{2\pi}\tan^{-1}\left(\frac{\eta}{\xi}\right)\right\}.\end{aligned} \tag{6.23}$$

The function $F^{-1}(f(\eta,\xi))$ in (6.23) maps the coordinates (η,ξ) in the Z-plane back to coordinates (Δ,ζ) in the original W-plane of the induced flow, thus performing an equivalent operation to the inverse mapping $\omega(z)$ in (6.17) acting on the complex coordinate z. As stated in Chapter 4, we have adopted the notation $F^{-1}()$, which strictly acts on the coordinates (η,ξ) of the function, for convenience and acknowledge that this is not conventional.

6.4 Analysis of solution

Figure 6.2 illustrates (dimensionless) streamlines of the induced flow, $\Psi = const.$, and corresponding contours of constant speed, $\bar{u} = U/(2\alpha_{\rm p}w_0) = const.$, for plumes with $\Gamma_0 = \{0.01,\ 0.1,\ 0.5\}$. As in Chapter 4, the solution is plotted on evaluating the integral in (6.23) using an adaptive quadrature numerical scheme, and confirmed on comparison with the full numerical solution of the governing boundary value problem for the induced flow based on a finite-difference scheme (outlined in Appendix E, with further details in §4.3.1 and §4.3.2 in Hunt (1994)). To maintain consistency with the plots corresponding to the lazy plume in figure 4.9, we fix the source half-width $b_0 = {Q_0}^2/((2\pi)^{1/2}M_0)$, and solely vary the source

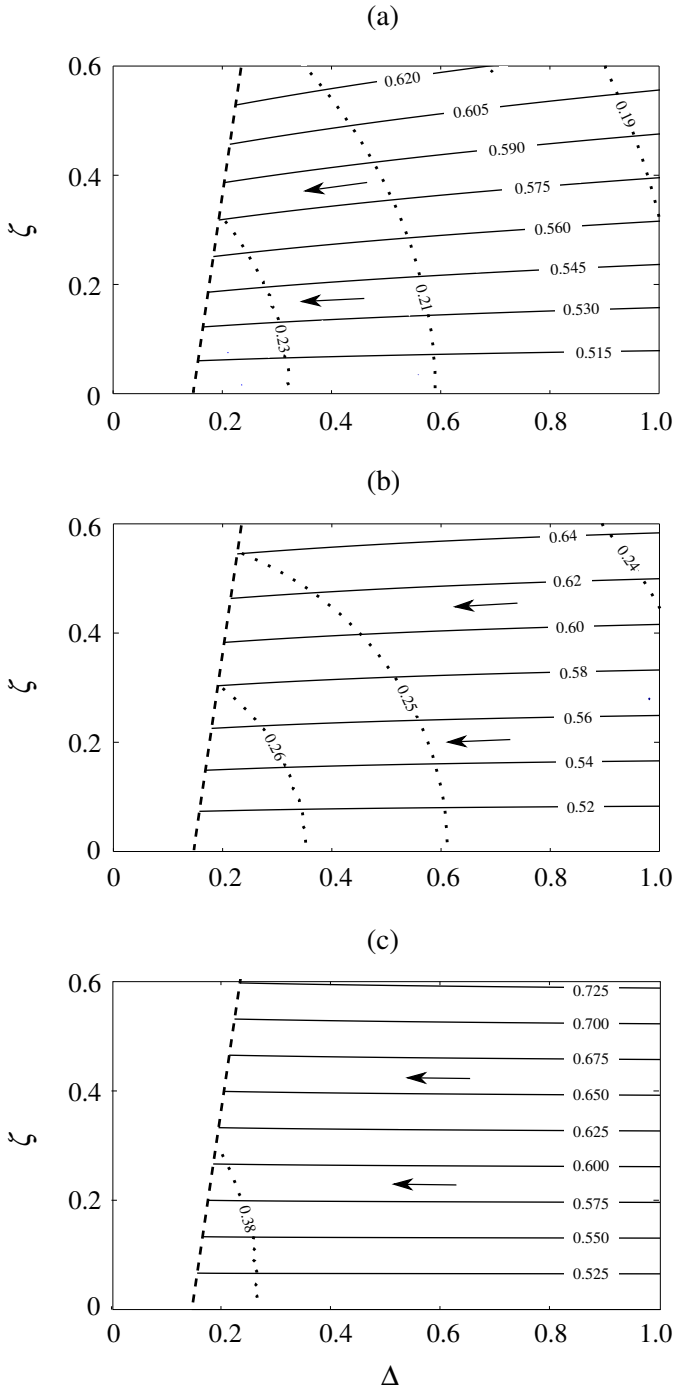

Fig. 6.2 Dimensionless streamlines, $\Psi = const.$ (solid lines), and corresponding contours of constant speed, $\bar{u} = U/(2\alpha_p w_0) = const.$ (dotted lines), for forced plumes with source conditions (a) $\Gamma_0 = 0.01$, (b) $\Gamma_0 = 0.1$ and (c) $\Gamma_0 = 0.5$. Values have been overlain onto each streamline and contour of constant speed. Arrows indicate the bulk direction of flow. The mapped edge (dashed line) corresponding to the plume perimeter, obtained upon applying the inverse mapping, $\omega(z) = z^{0.454} + \Delta(b_0)$, to the real axis of the Z-plane, is independent of Γ_0.

buoyancy flux B_0 to achieve the desired Γ_0 value in figure 6.2. In this respect, the forced plume can be viewed as having a relative deficit of source buoyancy flux compared to the pure plume. The highly forced plume induced flow exhibits a downward inclination and a decreasing speed with distance from the source, similar to the induced flow of the idealised jet in figure 2.3, owing to the 'jet-like' nature of the flow in the near-source region. This is not unsurprising given in the limit as $\Gamma_0 \to 0$ the forced plume approaches the jet. The magnitude of the flow inclination and the rate of decrease of speed from the source is, however, generally lower than that corresponding to the idealised jet, owing to the presence of a source supply of fluid and a finite speed at the source of the plume. The downward inclination of the plume induced flow becomes increasingly more pronounced with height, as the effect of the horizontal boundary reduces. With the supply of buoyancy flux continuously undertaking work above the source, eventually the momentum flux induced by buoyancy becomes the dominant component of the plume flow. This results in the local plume Richardson number Γ increasing vertically from its source value ($0 < \Gamma_0 < 1$) to one. The increasing value of Γ translates to an eventual decreasing inclination of the induced flow streamlines adjacent to the plume beyond some height. Therefore, similar to the solution for the flow induced by the lazy plume in Chapter 4, we predict a turning point in the inclination of the streamlines at the plume perimeter. The less highly forced plume solution (figure 6.2 (c)) has lost the downward inclination in the induced flow. This solution is not discussed further here as it raises questions as to the appropriateness of the entrainment model. This discussion forms a key component of Chapter 7.

6.4.1 Limiting case of jet with $\Gamma_0 = 0$

In this section we consider the validity of the forced plume induced flow solution (6.23) in the limiting case of the jet when $\Gamma = \Gamma_0 = 0$. The linear entrainment model (6.1) used to formulate the forced plume solution attains the jet entrainment coefficient α_j in the limit when $\Gamma \to 0$. The only change required to the current formulation to derive an induced flow solution for the jet is the scaling of the horizontal and vertical coordinates, which we modify to be scaled on α_j as

$$\zeta = \zeta_\mathrm{j} = \frac{2\alpha_\mathrm{j}}{\pi^{1/2} b_0} y \quad \text{and} \quad \Delta = \Delta_\mathrm{j} = \frac{2\alpha_\mathrm{j}}{\pi^{1/2} b_0} x, \tag{6.24}$$

respectively. Figure 6.3 illustrates the streamline portrait and contours of constant speed of the induced flow solution using the coordinates in (6.24) and $\gamma = 0.454$, alongside the idealised solution taken from Taylor (1958) and presented in Chapter 2. The idealised solution corresponds to the flow induced by a jet with an infinite source velocity issuing from a source

of infinite length and infinitesimal width. Note that the non-idealised solution is presented in a dimensionless form so as not to illustrate the solution for a specific scenario corresponding to particular values of the source parameters. Though a direct quantitative comparison is not made between the figures, we identify, based on a qualitative comparison, that both induced flows exhibit downwardly inclined flow patterns. However, upon closer observation, crucially, a vertical transition occurs in figure 6.3 (a), with the downward inclination of the flow at the jet perimeter increasing with height (to approach $\theta_\mathrm{p} = -45^\circ$ as $\zeta \to \infty$) as the effect of the horizontal boundary becomes less pronounced. This transition is in agreement, upon closer observation, with the induced flow streamlines in the visualisation from Lippisch (1958) in figure 1.2. The induced flow solution for the idealised jet in figure 6.3 (b) maintains a constant inclination of $\theta_\mathrm{p} = -45^\circ$ at the plume perimeter for all heights. The reason for the difference becomes apparent upon inspecting the jet entrainment velocities (which can be straightforwardly derived from the respective jet boundary conditions). More specifically, the (dimensionless) entrainment velocity,

$$\frac{dq}{d\zeta_\mathrm{j}} = \frac{u_\mathrm{e}}{\alpha_\mathrm{j} w_0} = (1+2\zeta_\mathrm{j})^{-1/2} \tag{6.25}$$

(from (6.12) with $\Gamma_0 = 0$ and using the vertical coordinate ζ_j), of the non-idealised jet decreases from its unit value at the source, in contrast to the idealised scenario for which the (dimensional) entrainment velocity, $d\chi/dy$ (2.5), decreases from a singularity at the source. Evidently, this singularity leads to non-physical behaviour of the induced flow throughout the entire domain.

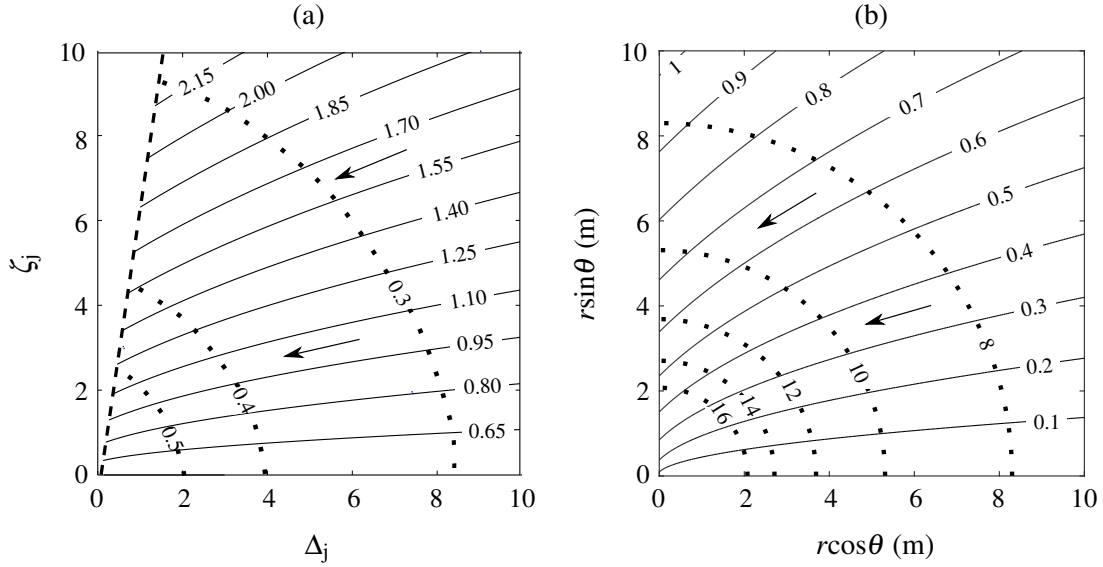

Fig. 6.3 Streamlines (solid lines) and contours of constant speed (dotted lines) for the flows induced by the partially-confined: (a) non-idealised jet, plotted using (6.23) with the rescaled coordinates in (6.24) and the speed $\bar{u} = U/(2\alpha_j w_0)$; and (b) line jet from figure 2.3. The values of the stream function and the speeds, which are dimensionless in (a) and dimensional in (b), are overlain on each contour. The dashed line in (a) denotes the perimeter of the jet. The arrows indicate the direction of motion.

6.5 Relative effects of forced and lazy plumes on their environments

In the following, we assess the effect on their environments of the forced plume, with $\Gamma_0 = 0.1$, in comparison to that of the lazy plume, with $\Gamma_0 = 10$, modelled in Chapter 4. As an example, we select the source fluxes for the forced plume, $M_0 = 0.109$ m^{3}s^{-2}, $B_0 = 0.003$ m^{3}s^{-3} and $Q_0 = 0.25$ m^{2}s^{-1}. These fluxes correspond to a plume source velocity of $w_0 = 2^{1/2}M_0/Q_0 = 0.615$ ms^{-1} and source buoyancy of $g'_0 = 2^{1/2}B_0/Q_0 = 0.017$ ms^{-2}. In this example the lazy plume has a source velocity that is approximately a factor of 3.5 times lower than that of the forced plume, but is subject to a source buoyancy that is 6.2 times greater. Owing to the lower entrainment coefficient of jets relative to plumes, accounted for here using the linear entrainment model in (6.1), note that the source entrainment velocity, $u_e = \alpha w_0$, is only 1.93 times lower for the lazy plume. The source width of the forced and lazy plumes are 0.23 m and 0.31 m, respectively.

Figure 6.4 illustrates the output upon applying the 'Velocity Ratio' diagnostic, which was introduced in Chapter 3, to compare the flows induced by these forced and lazy plumes. More specifically, the induced flow fields of speed, which were straightforwardly obtained

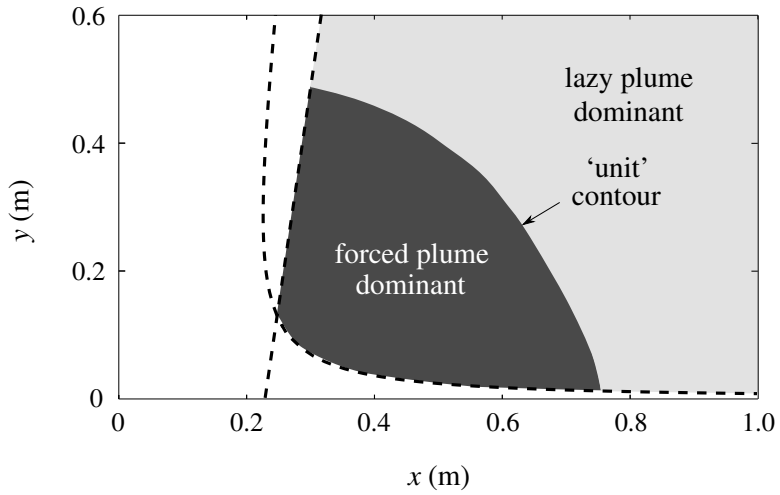

Fig. 6.4 'Unit' contour separating the forced plume dominant region ($U_{\mathrm{fp}}/U_{\mathrm{lp}} > 1$) from the lazy plume dominant region ($U_{\mathrm{fp}}/U_{\mathrm{lp}} < 1$) in the induced flow. The forced plume has a source velocity $w_0 = 0.615$ ms^{-1} and source buoyancy input $g'_0 = 0.017$ ms^{-2}, whilst the lazy plume has an approximately 3.5 times lower source velocity and 6.2 times higher source buoyancy. The straight and curved dashed lines correspond to the perimeters of the forced and lazy plumes.

using the dimensionless plots in figures 4.9 and 6.2, are represented as a fraction, $U_{\mathrm{fp}}/U_{\mathrm{lp}}$, at every location across the flow field. This enabled a 'unit' contour to be defined where the speeds are equivalent, which separates regions where the fraction is above and below unity, i.e. where the forced and lazy plumes have a stronger influence on the environment. Note that as the plume perimeters are accounted for in the induced flow solutions, the fraction can only be evaluated in the region external to the dashed lines denoting the plume perimeters and horizontal boundary.

Figure 6.4 illustrates that the forced plume, with a greater source (entrainment) velocity relative to the lazy plume, has a stronger effect on the environment closer to the source. Beyond the 'unit' contour, the effect of the larger buoyancy input at the source of the lazy plume takes over, and has a stronger effect in comparison to the forced plume. Following on from the comments made in Chapter 4, figure 6.4 also reiterates that a plume with a greater Γ_0 value does not necessarily induce greater flow speeds across the entire induced flow domain, which may have been a misinterpreted conclusion from the dimensionless plots in figures 4.9 and 6.2.

6.6 Conclusions

Together with the induced flow solutions for the pure and contracting lazy plumes in Chapters 2 and 4, respectively, we now have a representation of the induced flow across a broad range of plume source Richardson numbers. Highly forced plumes induce flows with a downward inclination, and increasing the forcing (lowering the Γ_0 value) of these plumes results in a steeper inclination in the induced flow. As with the lazy plume, we find that the inclination of the induced flow streamlines of a high forced plume exhibits a local variation with height. For a given induced flow, a transition occurs from a steepening inclination with height, as the effect of the horizontal boundary becomes increasingly less pronounced, to an eventual decreasing inclination with height as the influence of the plume's source input of buoyancy becomes dominant. The less highly forced plume fails to exhibit any downward inclination. This raises questions as to the appropriateness of the entrainment model, which forms a key component of the discussion in the following chapter.

The limiting case of the induced flow solution for the jet ($\Gamma_0 = 0$) was considered. In contrast to Taylor's idealised model, the solution indicated that the inclination of the induced flow streamlines increased with height. This result is qualitatively consistent with the visualisation from Lippisch (1958) in figure 1.2. Finally, we applied the 'Velocity Ratio' diagnostic, introduced in Chapter 3, to compare the flow induced by a forced plume with that induced by a lazy plume subject to a lower source velocity and markedly higher source buoyancy input. The output of the example considered indicated that the forced plume had the stronger influence closer to the source, before the effect of the larger buoyancy input in the lazy plume became dominant beyond some distance from the source. One should note that it is the source entrainment velocity, and not simply the source velocity, that determines the strength of the induced flow of the forced plume near the source, owing to the dependence of α on the flow's local Richardson number.

Based on the insights gained in this and previous chapters, the following chapter challenges many of the accepted assumptions and models employed herein and widely in the literature.

Chapter 7

A discussion on the induced flow modelling assumptions and their implications

Work in Chapters 4 – 6 centred on modelling and enhancing our understanding of an array of induced flows driven by two-dimensional plumes. These ranged from the flows induced by vertically distributed plumes, examples of which include, the flow adjacent to a vertical ice sheet (McConnochie & Kerr (2016a)) or cooled glazed window in an atrium, to the flows induced by plumes above slender horizontal slots, for instance, the forced plume released from multi-port diffusers following the waste-water treatment process (Adams & Trowbridge (1985)), or the lazy plume issuing from the top vent of a naturally ventilated room (Hunt & Coffey (2010)). Our solutions indicate that contrasting flow patterns and speeds are induced by each of the plumes considered, highlighting the significance of the plume source conditions and geometry in defining the flow driven in the ambient. When using the solutions derived to gain insight into the induced flows, one must pay close attention to their formulation. In particular, only with an appreciation of the key assumptions made in their development can the model limitations and range of applicability be realised. In this chapter, we examine and challenge many of the key modelling assumptions employed herein and widely in the literature. Some of the inferences will have been apparent whilst reading earlier chapters, whilst others will be less foreseeable. Though a number of avenues appear open at this stage to model other induced flows, crucially, this chapter challenges whether or not modelling other induced flows should be the next step.

This chapter is structured as follows. In §7.1 we discuss work from the literature undertaken on modelling the influence of second-order effects on the flow induced by the

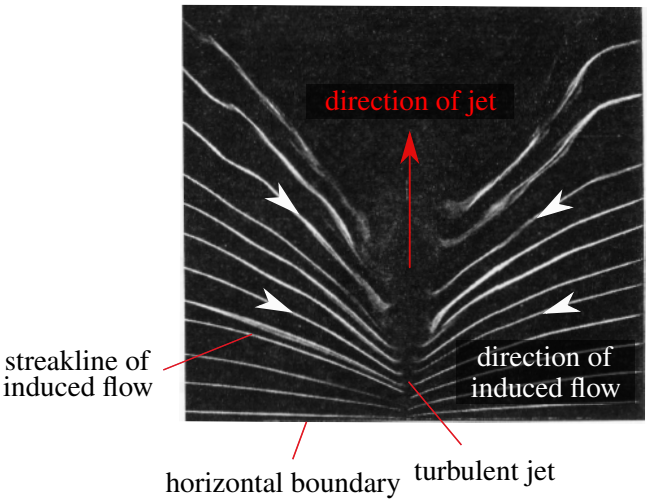

Fig. 7.1 Flow visualisation taken from Lippisch (1958) illustrating (white) downwardly inclined streaklines of the flow induced by a vertical turbulent jet issuing from a narrow slot in a horizontal boundary.

(idealised) jet. Based on the insight gained from the induced flow solutions in earlier chapters, we then turn our attention to a discussion on and critical analysis of the entrainment closures currently employed when modelling the forced and lazy plumes in §7.2 and §7.3, respectively. We complete the chapter with a review of, and comparison between, experimental studies measuring the entrainment coefficient for the vertically distributed plume in §7.4.

7.1 Second-order effects

The general modelling approach followed in Chapters 4 – 6 assumes that (i) the plume is in a stationary environment, and (ii) the induced flow is horizontal at the plume perimeter. Kotsovinos (1975) was the first to question these assumptions. He argued in response to (i) that a horizontal ambient pressure gradient must be generated in order to establish movement of fluid in the ambient, and that (ii) the induced flow typically has an inclination at the perimeter of a plume or jet flow, as seen, for instance, in the visualisation in figure 7.1. These inferences led Kotsovinos (1975) to question the validity of the widely employed modelling assumption that a constant momentum flux is maintained along a jet. Specifically, he stated that the ambient pressure gradient generated reduced the local jet momentum flux, whilst the inclination of the induced flow could either increase or decrease the momentum flux depending on whether the flow was upwardly or downwardly inclined, respectively. This influence on the jet momentum flux effects the local strength of the jet when modelled as a

sink, and thereby the corresponding induced flow. Various authors, including Kotsovinos (1975), Schneider (1985), Kotsovinos (1978) and Kotsovinos & Angelidis (1991) modelled the streamwise variation of the jet momentum flux. Of these studies, Kotsovinos & Angelidis (1991) were the only ones to account for both contributions ((i) and (ii) above) to the momentum flux variation in their model. They adopt the general modelling approach from Taylor (1958) but use a modified jet boundary condition that is dependent on the local momentum flux, $M(y)$, as opposed to the (source) momentum flux M_0. More specifically, starting from Taylor's (1958) induced flow solution (see table 2.1), which we shall refer to as the first-order solution, Kotsovinos & Angelidis (1991) determine the resulting variation in the jet momentum flux which, in turn, leads to the prediction of a new induced flow field. The authors employ an iterative numerical technique, and iterate until the difference between successive values of the inclination of the streamlines in the induced flow is less than 0.001°. Streamlines are predicted to enter the jet (modelled as a vertical line) issuing from a horizontal boundary at an angle of $\theta_\mathrm{p} = -48.7^\circ$ (where θ_p is defined to increase clockwise from the horizontal, as shown in figure 4.1), which is steeper than Taylor's (1958) solution of $\theta_\mathrm{p} = -45^\circ$. This is made clear in the comparison of the induced flow streamlines presented in figure 7.2 (a) which is taken from Kotsovinos & Angelidis (1991). Kotsovinos & Angelidis (1991) state that the increased inclination is in qualitative agreement with the visualisations by Giger (1987) and Lippisch (1958). The difference between the solutions indicates that second-order effects can influence the induced flow of a jet issuing from a horizontal boundary significantly. Taylor's (1958) solution (in Chapter 2) and the Kotsovinos & Angelidis (1991) second-order solution derived for the unconfined jet are, by contrast, found to coincide, as shown by the induced flow streamline portrait in figure 7.2 (b). In this case, the loss in momentum flux due to the induced pressure gradient is compensated for by the momentum flux increase resulting from the (slight) upward inclination of the induced flow along the jet axis. The difference in the inclination of induced flow streamlines at the jet axis, when modelling the induced flow using Taylor's (1958) approach and the second-order approach by Kotsovinos & Angelidis (1991) has been generalised by Kotsovinos & Angelidis (1991) to inclinations of the solid boundary $-90^\circ \leq \theta_\mathrm{b} \leq 15^\circ$ (where $\theta = \theta_\mathrm{b}$ is taken as positive in the anti-clockwise direction from the horizontal, with $\theta_\mathrm{b} = -90^\circ$ corresponding to the unconfined jet where the solid boundary represents the plane of symmetry below the source). It is found that reducing θ_b has the effect of reducing the difference in inclination output by the models from approximately 6° when $\theta_\mathrm{b} = 15^\circ$, to less than 1° when $\theta_\mathrm{b} = -90^\circ$.

Kotsovinos & Angelidis (1991) compare their predictions for the streamwise variation of momentum flux for a jet issuing from a horizontal boundary (i.e. when $\theta_\mathrm{b} = 0^\circ$) with the empirical measurements of Miller (1957), Heskestad (1965), Goldschmidt & Eskinazi

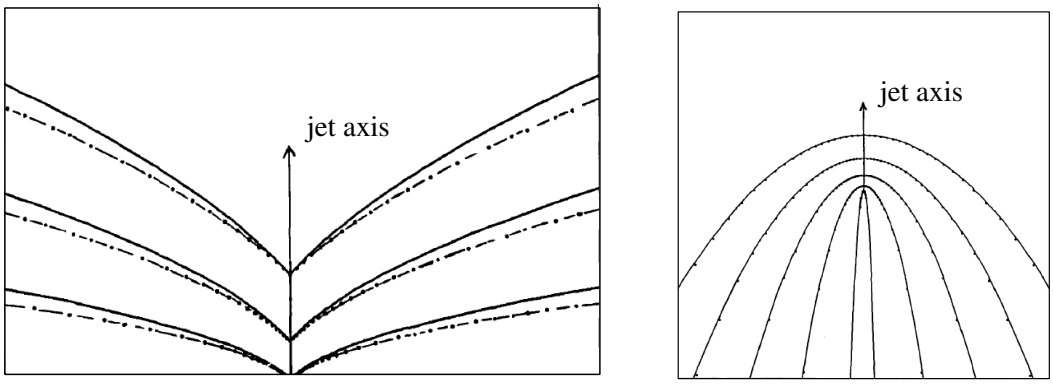

Fig. 7.2 Streamlines of the flow induced by a vertical jet (a) issuing from a horizontal boundary and (b) in an open space taken from Kotsovinos & Angelidis (1991). The dashed lines correspond to Taylor's (1958) solution (using a constant jet momentum flux) and the solid lines denote the second-order solution developed by Kotsovinos & Angelidis (1991) (using a non-constant jet momentum flux with height).

(1966), Kotsovinos (1975) and Giger (1987). The measurements all appear to show that a momentum flux reduction of at least 20% occurs over 200 source widths downstream. However, the precise magnitude and rate of the reduction differs amongst each of the authors. Noting that a given rate of the reduction corresponds to a specific inclination of the induced flow streamlines at the jet axis, θ_p, Kotsovinos & Angelidis (1991) identify that $\theta_p = -48.7^\circ$ (which they theoretically derive) coincides with the measurements of Heskestad (1965), whilst the data for all other experiments more closely align with θ_p values between -43° and -59.5°. To further highlight the uncertainty in the momentum flux reduction, Appendix A in Giger et al. (1991) presents measurements from 27 authors, who exhibit a range of values for the variation in momentum flux over 50 source widths from the jet's source. Arguably, these variations observed could be due to: differences in the experimental set-ups; secondary flow effects, e.g. an induced recirculation or the presence of a viscous boundary layer formed in the environment resulting from the finite dimensions of the rooms or laboratory tanks; and/or alternatively, a weak density gradient or ambient current present (other than that driven by the induced flow).

The aforementioned research papers have shown that the horizontal pressure gradient in the ambient and inclination of the induced flow have an influence on the streamwise variation of the jet momentum flux. It has been identified that, in a partially-confined environment with a horizontal boundary, this leads to an increase in the downward inclination of the

induced flow entering the jet of 3.7°. The jet represents a limiting case of the forced plume (with source Richardson number $0 < \Gamma_0 < 1$) considered in Chapter 6. For the forced plume, second-order effects are, in general, expected to be smaller and reduce further as the flow becomes more 'plume-like' (i.e. Γ_0 increases from the pure jet limit of $\Gamma_0 = 0$). This is due to the reduced inclination of the induced flow streamlines with increasing Γ_0, as is evident from our solution illustrated in figure 6.2 in Chapter 6. The reduced inclination results in a smaller vertical component of the induced flow opposing the plume motion and reducing the local plume momentum flux. The influence of the second-order effects on the flows induced by the contracting lazy plume and vertically distributed plume (Chapters 4 and 5) will be minimal, as a result of the upward inclination of the induced flow having a positive contribution to the plume's momentum flux. This will potentially offset the momentum flux reduction that occurs from the induced pressure gradient. Based on the discussion above, we can be confident in having employed the general (first-order) approach from Taylor (1958) to model the flows induced by the vertically distributed plume and plumes above a horizontal slot. In addition, the increased complexity of the second-order approach and computational cost to implement the method outweighs the marginal improvement in accuracy that would be gained in the solutions. It is also worth highlighting that any advancements to account for second-order effects would be questionable until the modelling issues presented in the following sections are addressed.

7.2 Forced plume entrainment

A solution was developed for the flow induced by a forced plume ($0 < \Gamma_0 < 1$) in Chapter 6. Owing to the larger value of the entrainment coefficient measured for the pure plume ($\alpha = \alpha_\mathrm{p} = 0.13$) relative to that for the jet ($\alpha = \alpha_\mathrm{j} = 0.05$), the forced plume, which corresponds to a flow between these limits, was not modelled using a constant value of the entrainment coefficient. Further, selecting a constant value of α would result in a jet spreading at twice the rate of a pure plume, a feature which is inconsistent with observations that indicate equal spreading rates (Fischer et al., 1979). As a consequence of these shortcomings, we adopted the entrainment model proposed by List & Imberger (1975)

$$\alpha = \alpha_\mathrm{j} + (\alpha_\mathrm{p} - \alpha_\mathrm{j})\Gamma, \tag{7.1}$$

with Γ denoting the local plume Richardson number. A value of $\kappa = \alpha_\mathrm{j}/\alpha_\mathrm{p} = 0.5$ represents an instance, corresponding to the formulation proposed by Priestley & Ball (1955), for which the forced plume is straight-sided, i.e. with $d\bar{b}/d\zeta = 1$, where $\bar{b} = b/b_0$ and $\zeta =$

$2\alpha_p y/(\pi^{1/2} b_0)$ are the dimensionless local half-width and vertical coordinate, as defined in Chapter 6. Consistent with observations by Kotsovinos & List (1977) that the forced plume is indeed straight-sided, we employed this value of κ when deriving the induced flow solution in Chapter 6. The resulting induced flow streamline portraits presented in §6.4, which have been replicated for convenience in figure 7.3, indicate that highly forced plume induced flows are generally downwardly inclined; an intuitive result considering that these plumes behave in a 'jet-like' manner in the near-source region. It is also apparent from figure 7.3, however, that the induced flow streamlines corresponding to $\Gamma_0 = 0.5$ do not display downward inclination, in spite of the plume being moderately forced (relative to the pure plume). In fact, upon closer inspection, the streamlines exhibit a slight upward inclination. Such an observation directs us towards plotting the vertical gradient of the forced plume boundary condition (6.14), namely $d\Psi/d\zeta$ (or equivalently the entrainment velocity $u_e/(2\alpha_p w_0) = (1/2)\cdot dq/d\zeta$), for the induced flow. As before q and Ψ are the scaled volume flux and stream function, respectively. We plot the vertical variation of $d\Psi/d\zeta$ for a range of source Γ_0 values using $\kappa = 0.5$ in figure 7.4 (solid lines). Focussing on the solid lines in the plot, evidently, the plume flow exhibits an array of near-source entrainment characteristics. Immediately above the source at $\zeta = 0$, the vertical gradient of the entrainment velocity changes sign with Γ_0; from negative for a highly forced plume, to positive for a weakly forced plume. Note that the aforementioned flow features, output when using $\kappa = 0.5$, also prevail (but are shifted) for other realistic values of the ratio κ. Consider, for instance, the dotted and dashed lines in figure 7.4 which correspond to $\kappa = 0.4$ and $\kappa = 0.6$, respectively. It is evident that the increasing entrainment demand with height for $\Gamma_0 = 0.5$ (positive gradient) is responsible for the upwardly inclined induced flow pattern observed in figure 7.3 (c).

Prior to continuing the discussion, at this point it is worth stating that inferences made subsequently are pertinent to plume flows that are turbulent at (or very close to) their source. Specifically, we do not consider flows with a significant development region, as this region is strongly dependent on the source geometry used in the application or experiment. Flows that are turbulent for instance at their source do exist in applications, including, for example, when wastewater is discharged from a multi-port diffuser into a river body (as observed in Adams & Trowbridge (1985)). Hunt & Kaye (2001) discuss obtaining turbulent plume source conditions in laboratory experiments, and devise an intricate nozzle design containing a sharp expansion and meshing to achieve this condition using their set-up.

Focussing on a forced plume that is turbulent at (or very close to) the source, on physical grounds one would expect the source supply of momentum flux to be dominant over the momentum flux induced by the buoyancy force immediately above the source. Thus, irrespective of the source Richardson number of the forced plume, 'jet-like' behaviour is expected in the

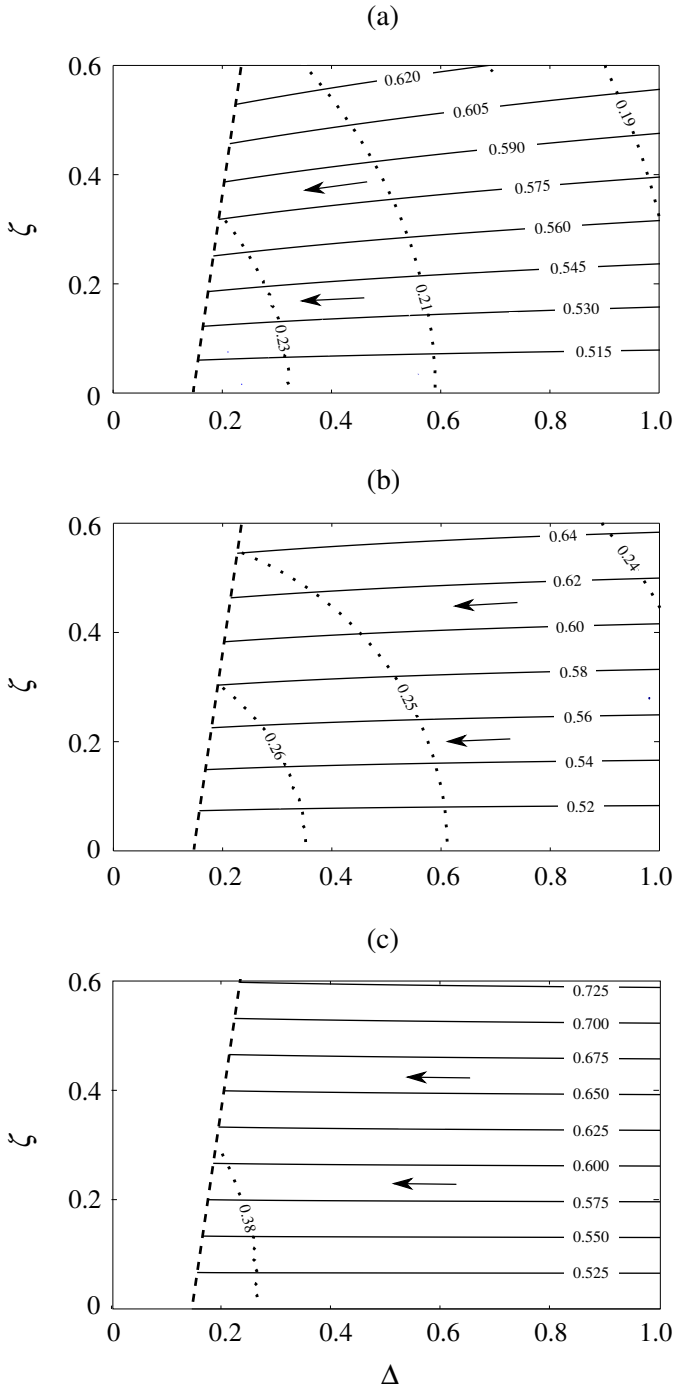

Fig. 7.3 Dimensionless streamlines, $\Psi = \chi/\chi_0 = const.$ (solid lines), and corresponding contours of constant speed, $\bar{u} = U/(2\alpha_p w_0) = const.$ (dotted lines), for forced plumes with source conditions (a) $\Gamma_0 = 0.01$, (b) $\Gamma_0 = 0.1$ and (c) $\Gamma_0 = 0.5$. Values have been overlain onto each streamline and contour of constant speed. Arrows indicate the bulk direction of flow. The mapped edge (dashed line) corresponds to the plume perimeter.

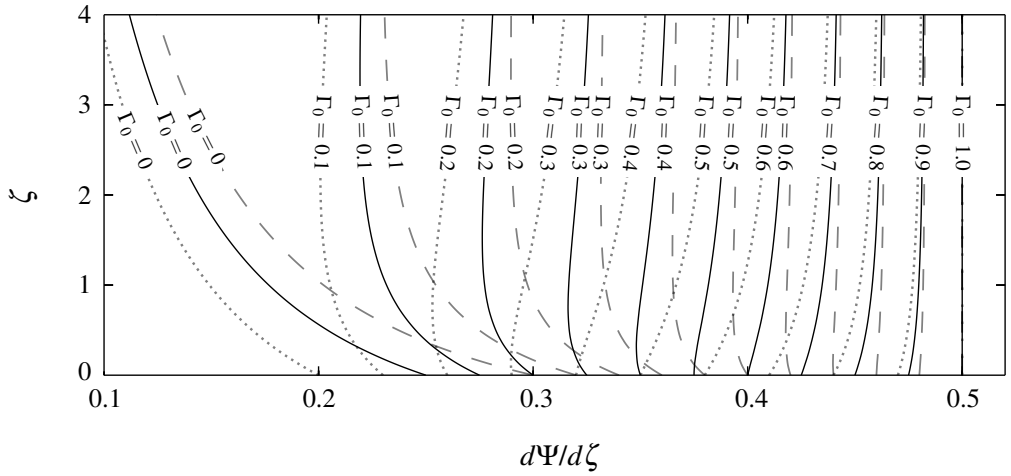

Fig. 7.4 The vertical variation of the gradient of the plume boundary condition (6.14), $d\Psi/d\zeta$, for forced plumes with $0 < \Gamma_0 < 1$, derived using the linear entrainment closure in (7.1) with $\kappa = \{0.4 \text{ (dotted line)}, \ 0.5 \text{ (solid line)}, \ 0.6 \text{ (dashed line)}\}$.

near-source region, from which a vertical transition to the pure plume asymptote will occur. Indeed this flow behaviour is observed in the experiments of Kotsovinos & List (1977) and Papanicolaou & List (1988) for the forced plume above a slot and circular source, respectively. These authors' measurements indicate that the plume behaves as a jet up to (approximately) a 'jet-length' from the source, before undergoing a vertical transition and maintaining a pure plume state beyond 5 'jet-lengths'. The notion of a 'jet-length' was introduced when developing diagnostics to compare the idealised jet and idealised plume in Chapter 3. There, the 'jet-length' provided the characteristic scale for separating regions of the induced flow where the jet and plume induced greater speeds relative to one another. The momentum-driven jet had a stronger influence close to the source, and the buoyancy-driven plume had the dominant effect beyond some distance from the source. For a non-idealised source issuing with both source fluxes of momentum and buoyancy, the notion of a 'jet-length' still applies (indeed it was for this situation that it was originally conceived), and defines a characteristic vertical scale over which the source momentum flux is greater than the buoyancy-induced momentum flux. It is evident in figure 7.4, however, that a 'jet-like' region does not exist above the source for $0 < \Gamma_0 < 1$, and hence there is no notion of a 'jet-length'. In fact, figure 7.4 indicates that the flow behaviour (at the source) moves increasingly away from that of a jet with increasing Γ_0. Indeed, when $\Gamma_0 > 0.5$, the non-physical flow feature of an increasing entrainment velocity with height occurs, which does not correspond to the characteristics measured or otherwise of either a jet or a pure plume. This non-physical behaviour arises, as

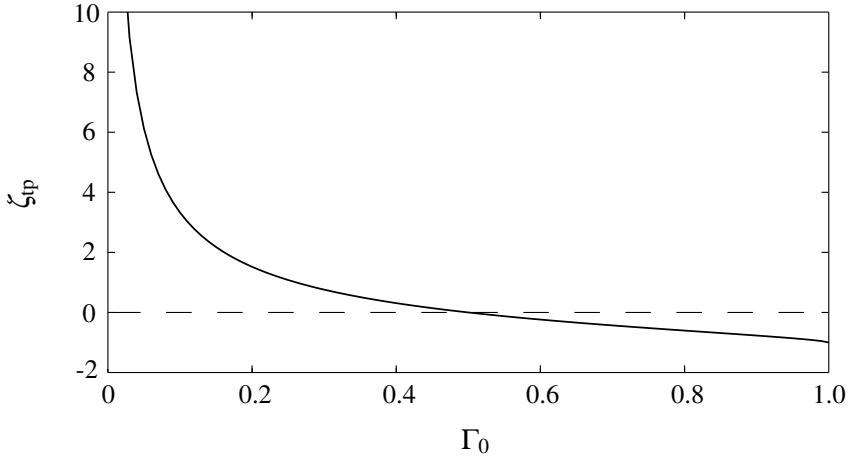

Fig. 7.5 The height of the turning point $\zeta = \zeta_{tp}$ in the profiles of entrainment velocity for $\kappa = 0.5$ plotted in figure 7.4, as function of the plume source Richardson number Γ_0.

the linear entrainment model in (7.1) does not include information on proximity to the source. Thus, a flow with a given source Richardson number has an entrainment coefficient at its source identical to the local entrainment coefficient of a flow with the same local Richardson number at some height.

A turning point is evident in a number of the profiles in figure 7.4. The turning point, given by

$$\zeta = \zeta_{tp} = \left(\frac{1-\Gamma_0}{\Gamma_0}\right)^{2/3} - 1, \tag{7.2}$$

is located on differentiating the expression for (twice) the entrainment velocity, $dq/d\zeta$ in (6.12), with respect to the vertical coordinate, and equating the resulting expression to zero. Expression (7.2) is plotted as function of Γ_0 in figure 7.5. The turning point is located at $\zeta_{tp} = -1$ for the pure plume ($\Gamma_0 = 1$) (not shown in figure 7.4), increases in height for a lower Γ_0 value, and asymptotes to $\zeta_{tp} \to \infty$ for the jet ($\Gamma_0 = 0$). The turning point is at the source, $\zeta_{tp} = 0$, for $\Gamma_0 = 0.5$. The presence of a turning point is not unsurprising, considering that the flow transitions with height for $0 < \Gamma_0 < 1$. More specifically, we would anticipate that plume entrainment velocities would need to exhibit a turning point, in order to transition from a 'jet-like' scaling immediately above the source (i.e. initially following the curve corresponding to the jet in figure 7.4), to the pure 'plume-like' scaling exhibited in figure 7.4 at a large height. Although we anticipate the existence of a turning point in reality, we argue that it is a construct of the entrainment model (7.1) for the turning point to be located at exactly $\zeta_{tp} = -1$ for the pure plume and at $\zeta_{tp} = 0$ when $\Gamma_0 = 0.5$ (figure 7.5).

As an alternative to specifying a form for the entrainment coefficient α, Yannopoulos & Noutsopoulos (1990) for the plume above a slot (and equivalently Noutsopoulos & Yannopoulos (1987) for the plume above a circular source) close their governing equations by modelling entrainment using spreading coefficients where the plume is assumed to widen at a prescribed rate (see Jirka et al. (1975)). Specifically, they specify that the function,

$$\phi = \left(\frac{K_w^2 + K_c^2}{K_w} \right)^{1/2}, \tag{7.3}$$

takes a constant value. The terms $K_w = b_w/y$ and $K_c = b_c/y$ denote the spreading coefficients of velocity and tracer concentration (equivalent to a scaled buoyancy), respectively, with y denoting height and b_w and b_c the horizontal distance at which the respective (Gaussian) properties fall to $1/e$ of their centre-line values. The assumption of a constant value for expression (7.3) is confirmed by the authors' measurements. Specifically, they identify that $\phi = 0.60$ upon measuring the spreading rates as $K_w = 0.132$ and $K_c = 0.173$. The terms K_w and K_c are inherently related to the entrainment coefficient α, and for comparative purposes, defining

$$\bar{y} = \frac{y}{2b_0}, \quad \text{and} \quad R_0 = \Gamma_0 R_\text{p} = \frac{B_0 {Q_0}^3}{{M_0}^3} \tag{7.4}$$

as the (alternatively defined) source Richardson number, we derive the entrainment coefficient that is equivalent to the model in expression (7.3), as

$$\alpha = \frac{\pi^{1/2} K_w (1/2 + (4/5 + A\bar{y}^{3/2}) R_0)}{2(1 + (8/5 + A\bar{y}^{3/2}) R_0)}, \tag{7.5}$$

with $A = \pi^{1/4} 2^{-7/4} \phi {b_0}^{-3/2}$ (see §F.1 in Appendix F for derivation). Note that expression (7.5) is independent of K_c. In §F.1 it is highlighted that the values of α from (7.5) at the source and at a large height are close to the average values measured for the jet ($\alpha = 0.05$) and pure plume ($\alpha = 0.13$), respectively, that were presented in Chapter 2. A plot from Yannopoulos & Noutsopoulos (1990) of the scaled streamwise centre-line velocity derived using (7.3), together with experimental measurements from Kotsovinos (1975) and Ramaprian & Chandrasekhara (1983), is presented in figure 7.6 (where $F_0 = {R_0}^{-1/2}$ denotes the plume source Froude number). Consistent with the entrainment coefficient variation in height in (7.5), the plot indicates that the centre-line velocity exhibits a 'jet-like' scaling at the source, and asymptotes to a pure 'plume-like' constant value with height. The physical basis for this behaviour becomes apparent upon deriving the form of the local Richardson

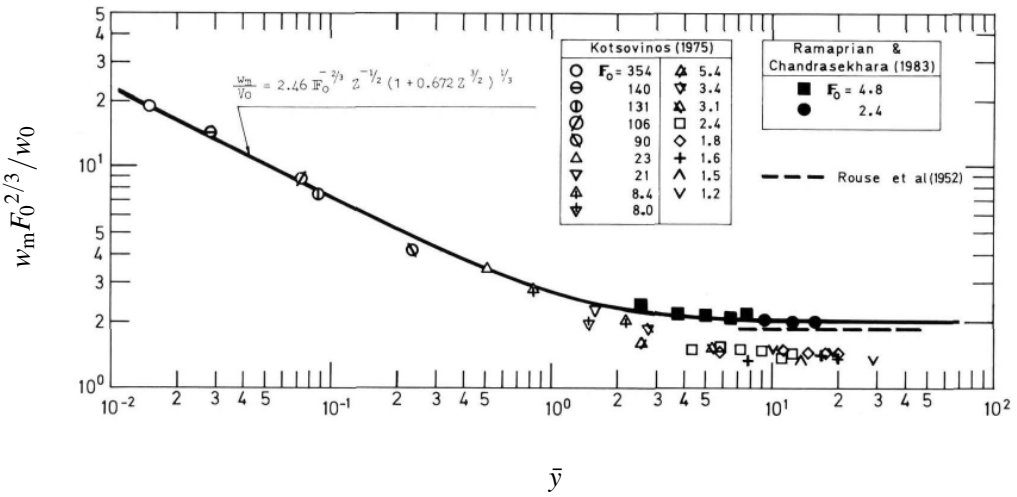

Fig. 7.6 Image taken from Yannopoulos & Noutsopoulos (1990) of the vertical variation of the dimensionless centre-line velocity for a plume, together with velocity measurements from various authors.

number,

$$\Gamma(\bar{y}) = \frac{2^{7/4}\pi^{3/4}{K_\mathrm{w}}^{3/2}R_0}{R_\mathrm{p}}\bar{y}^{3/2}\left(1+\frac{8R_0}{5}+\left(\frac{\pi}{2}\right)^{1/4}\phi R_0\bar{y}^{3/2}\right)^{-1} \tag{7.6}$$

(see §F.2 in Appendix F for derivation). This expression indicates the non-physical result that regardless of the value of Γ_0 all plume flows begin as a pure jet ($\Gamma_0 = 0$) at their source located at $\bar{y} = 0$ (i.e. with zero buoyancy flux), and acquire buoyancy immediately above their source, before transitioning to a pure plume regime (i.e. $\Gamma \to 1$ as $\bar{y} \to \infty$). Yannopoulos & Noutsopoulos (1990) did not examine $\Gamma(\bar{y})$ and so perhaps this non-physical result was not clear to them. Similar non-physical flow behaviour has also been output by Noutsopoulos & Yannopoulos (1987) and the so-called 'second-order' models developed by Wang & Law (2002) and Yannopoulos (2006), which additionally account for the turbulent contributions to the mass and momentum fluxes, and the vertical variation of the concentration-to-velocity width ratio.

The plume models discussed thus far require prior specification of the profiles of velocity and buoyancy, together with a closure that describes plume entrainment. The resulting governing equations are a set of ordinary differential equations (ODEs) in terms of integral quantities (see Appendix A). An alternative modelling approach is to directly utilise the original partial differential equations, and introduce a turbulence model to describe the unknown turbulent shear stresses. This technique has been employed with a $k-\varepsilon$ turbulence model by Chen & Chen (1979) and Hossain & Rodi (1982) (where k and ε are the turbulent kinetic

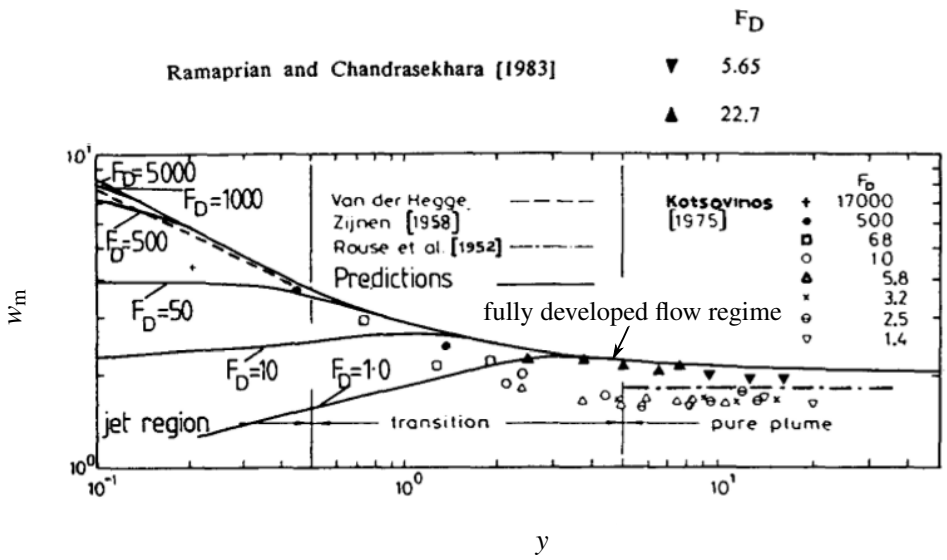

Fig. 7.7 The vertical variation of the plume centre-line velocity predicted using the model from Malin (1987), together with velocity measurements by various authors, for a range of source Froude numbers $1 < F_D < 5000$. Models devised by various authors in the pure regimes have also been overlain. Image taken from Malin (1987).

energy and dissipation rate of turbulent kinetic energy, respectively), a $k-W$ turbulence model by Malin (1987) (where W is the time mean square of the vorticity fluctuations) and a composite eddy viscosity model by Baker et al. (1989). Although this approach requires fewer assumptions in comparison to the integral approach, the method is more complicated, for instance, with Malin (1987) requiring 14 empirical coefficients to be evaluated. Figure 7.7 is a plot from Malin (1987) of the vertical variation of the centre-line velocity, w_m, for a range of source Froude numbers $1 < F_\mathrm{D} < 5000$ (where $F_\mathrm{D} = 1/(\Gamma_0 R_\mathrm{p})$ with $R_\mathrm{p} \approx 0.29$), together with measurements from Kotsovinos (1975) and Ramaprian & Chandrasekhara (1983). Note that a pure plume corresponds to $F_\mathrm{D} \approx 3.5$ and $F_\mathrm{D} \to \infty$ denotes a jet. The centre-line velocity curve is in close agreement with measurements from Ramaprian & Chandrasekhara (1983) in the pure plume regime (but overestimates those from Kotsovinos (1975)). Moreover, the (very) highly forced plume exhibits 'jet-like' behaviour close to its source, with the model in close agreement with the model for a jet proposed by van der Hegge Zijnen (1958). It is evident, however, that for $F_D \leq 50$ (equivalent to $\Gamma_0 \geq 0.07$), the plume centre-line velocity w_m initially increases with height above the source. This is in contrast with the solution based on the linear entrainment model (7.1), and with our intuition that forced plumes behave in a 'jet-like' manner immediately above their source. A similar output to that in figure 7.7 has also been illustrated by Chen & Chen (1979) based on their solution. Although Malin

(1987) and Chen & Chen (1979) state that their models are to be used to describe the fully developed region of the plume flow, which corresponds to the main (descending) curve in figure 7.7, one should note that the model outputs would not be valid when the flow is fully developed at (or very close to) the source. The solution from Baker et al. (1989), based on a composite eddy viscosity model, exhibits 'jet-like' behaviour immediately above a virtual origin (below the real source), as opposed to immediately above the real source. Further, Baker et al. (1989) do not explicitly model the dependency of plume flow properties on the source Richardson number.

To summarise, inspired by the induced flow solution for the forced plume in Chapter 6, we have identified that the vertical variation of flow properties of the plume based on current entrainment models result in some form of non-physical flow behaviour. Either the solutions do not exhibit 'jet-like' behaviour immediately above the plume source, or the plume is a jet (with no buoyancy) at the source. Furthermore, entrainment models are currently validated mainly using measurements away from the plume source and, thereby, authors have also overlooked or neglected flow behaviour close to the source. Though we have now questioned the validity of the forced plume induced flow solution in Chapter 6, it is the development of this solution that has led us to fundamentally question existing entrainment models. Arguably then, developing an improved understanding of entrainment is a priority for future research relative to incorporating the second-order effects discussed in §7.1.

7.3 Lazy plume entrainment

We utilised the entrainment closure, $u_\mathrm{e} = \alpha w$ (Taylor, 1945), which relates the local entrainment velocity u_e to a local vertical velocity w in the plume via a constant fraction, α, when modelling the flow induced by the lazy plume in Chapter 4. Though initially proposed to describe pure plume entrainment, the solution for the lazy plume based on a constant entrainment coefficient successfully exhibits (qualitative) flow features consistent with experiments, including the plume contraction and plume neck observed in figure 4.1. Only very recently have Carlotti & Hunt (2017) developed the first entrainment model to specifically describe lazy plume entrainment. Their model accounts for the enhanced entrainment in highly lazy plumes above a circular source observed by Pham et al. (2005) and Kaye & Hunt (2009) and takes the form of a power-law function, given by

$$\alpha = \alpha_\mathrm{p} \Gamma^{\omega}, \tag{7.7}$$

where the exponent $0 \leq \omega < 1$. A value of $\omega = 0.62$ is found by Carlotti & Hunt (2017) to have close agreement with the measurements from Kaye & Hunt (2009). We did not employ the entrainment model in (7.7) when developing our solution for the lazy plume induced flow in Chapter 4 as the focus of the work was on the solution approach rather than the details of plume entrainment. Moreover, the developments in Chapter 4 occurred prior to the publication of Carlotti & Hunt (2017), and whilst their formulation successfully models lazy plumes above circular sources, measurements of entrainment by lazy plumes above slender horizontal slots are not available in the literature to further validate the model against. Experiments will soon be undertaken within the research group to quantify entrainment into lazy plumes above slender slots. Once the appropriate entrainment model has been formulated using these measurements, it will be straightforward to determine the corresponding induced flow solution using the method as outlined in Chapter 4. More specifically, the entrainment model will lead to a new plume boundary condition. Then, the method based on the theory of functions of a complex variable, as implemented in Chapter 4, needs to be simply reapplied. Specifically, the plume boundary condition is to be input into Poisson's theorem (4.30), following which the (inverse) conformal mapping, the constants of which are determined upon reimplementing the mapping optimisation outlined in §4.4, is to be applied to obtain the solution. This straightforward reimplementation of the method highlights the robustness of our modelling approach, as well as the ease with which the method can be applied to derive the induced flow solution following any developments regarding entrainment functions that may occur in the future.

7.4 Vertically distributed plume experiments

Measurements in the laboratory are necessary to determine the entrainment coefficient, α, which is required to close the governing equations describing the vertically distributed plume in Chapter 5. Experiments have used either a saline/fresh water plume or a thermal plume in a confined environment to determine the entrainment coefficient, and these are discussed and compared in this section.

Cooper & Hunt (2010) supply saline solution through a sintered vertical plate (using a pressure gradient) into a ventilated and a non-ventilated fresh water tank to form a downward flowing plume. Owing to the stratification in the confined environment and the hydrostatic pressure gradient across the porous plate, the authors measure some non-uniformity in the source volume and buoyancy fluxes. Kerr & McConnochie (2015) and McConnochie & Kerr (2016a,b) used an alternative experimental set-up of a vertical ice wall in a water tank. They fixed a heat exchanger at one end of their tank to grow an ice wall and subsequently control

the temperatures. The vertical ice wall dissolves in (homogeneous) salty water, with the dissolving fresh ice forming a distributed plume that is positively buoyant compared to the salty ambient. The resulting plume adjacent to the ice has a laminar flow component over approximately the lower 8 % of the wall height, before transitioning to a turbulent regime. In contrast, the saline plume in Cooper & Hunt (2010) exhibited laminar behaviour over a markedly smaller region, owing to the injection of fluid through the small pores of the sintered plate. The measured position of the dissolving ice interface adjacent to the turbulent region is relatively uniform, with the ice ablation velocity found to have a standard deviation of only 6% along the height (Kerr & McConnochie, 2015).

In spite of the differences between the aforementioned set-ups, McConnochie & Kerr (2016b) measure the value of the coefficient for the volume flux ($Q = c_{\mathrm{v}}\beta^{1/3}y^{4/3}$ (5.10)) as $c_{\mathrm{v}} = 0.043 \pm 0.003$, which is similar to $c_{\mathrm{v}} = 0.05$ measured by Cooper & Hunt (2010) in their saline plume experiments. Both authors measure their values of the coefficient based on tracking the rising/lowering of the ambient density interface and employing the classic filling box theory of Baines & Turner (1969). Noting that the local plume volume flux Q for the distributed plume is equivalent to the local stream function χ used to represent the plume boundary condition (5.13) in Chapter 5, the similarity in the measured values of c_{v} implies that the difference in the values has little impact on the plume boundary condition and, thereby, the induced flow solution. Despite little difference between the volume fluxes, McConnochie & Kerr (2016b) measure the vertical (top-hat) velocity in the plume to be approximately three times lower than that of Cooper & Hunt (2010). To explain this difference, note that the plume in Cooper & Hunt (2010) is an advective boundary layer (i.e. a high Péclet number flow), as a result of forcing fluid through pores in the sintered plate. In contrast, the plume adjacent to the ice wall in McConnochie & Kerr (2016b) is a diffusive boundary layer. Moreover, a diffusive boundary layer confines buoyancy closer to the vertical source, resulting in the maximum plume velocity being located nearer the source (McConnochie & Kerr, 2016b). This results in the source exerting a larger drag force on the plume, which is predicted by McConnochie & Kerr (2016b) to be approximately 90% of the upward buoyancy force based on their velocity measurements. This is in contrast to Cooper & Hunt (2010) who state that drag forces are negligible in their experiments and theory. From their measurements of volume flux and velocity, McConnochie & Kerr (2016b) explicitly identify a constant (top-hat) entrainment coefficient, $\alpha_{\mathrm{vdp}} = (1/w) \cdot \mathrm{d}Q/\mathrm{d}y = 0.048$, that is greater than the value $\alpha_{\mathrm{vdp}} = 0.02$ from Cooper & Hunt (2010).

Caudwell et al. (2016) create a distributed plume in their experiments using an approximately uniformly heated (isothermal) aluminium side-wall plate fixed on a sealed water tank. The plume exhibits a laminar region which occupies approximately half of the tank height.

In contrast to the saline technique of Cooper & Hunt (2010), maintaining a non-adiabatic condition on surfaces other than the source to prevent boundary layers forming is a significant challenge in thermal experiments. Caudwell et al. (2016) insulate the sides and bottom of their tank using synthetic plastics, and the top using polystyrene, to minimise the strength of any boundary layers that form. Using Particle Image Velocimetry (PIV) data, the authors sum the velocity measurements to identify an (average) value for the entrainment coefficient of $\alpha_{\text{vdp}} = 0.019$ over the turbulent region of the plume, which is in very close agreement with $\alpha_{\text{vdp}} = 0.02$ found by Cooper & Hunt (2010). However, a large variation in α_{vdp} is measured, falling from a value (close to) 0.08 to below 0.01 over the course of their experiment. This is due to the stratification in the tank, i.e. the deepening and warming of the upper layer, as well as flow features within the upper layer, which are evident from analysing the PIV data. For instance, from their images of the flow, one may observe a strong recirculation following impingement of the plume on the ceiling of the tank, which feeds directly into the turbulent region of the plume. This leads to an increase in the local value of α_{vdp} measured. The aforementioned features of the (confined) flow highlight the difficulty of using PIV data directly to estimate the plume entrainment coefficient, as opposed to taking bulk flow measurements as in Cooper & Hunt (2010) and McConnochie & Kerr (2016b).

7.5 Conclusions

The discussion in this chapter has centred on examining key modelling assumptions used in Chapters 4 – 6, providing insight into plume entrainment, and exploring aspects of plumes and their induced flows that have not previously been considered. We argued that the second-order effects of the ambient pressure gradient and inclination of the induced flow will have little influence on the plume induced flows. Despite the many differences amongst experiments undertaken on the vertically distributed plume, crucially, there is agreement over the entrainment velocities (i.e. the vertical gradient of the volume flux), which is the defining property governing the induced flow. A major challenge faced when modelling the flows induced by the forced and lazy plumes is accurately describing their entrainment behaviour. Based on the insight gained from our induced flow solution for the forced plume (6.23), we have highlighted that current entrainment models for the forced plume have fundamental limitations. Our understanding of entrainment into lazy plumes above slender slots is limited, owing to an absence of experimental campaigns undertaken on the subject. Despite the uncertainty in the solutions for the forced and lazy plume induced flows developed in the earlier chapters, once future developments have been made, it will be straightforward to derive the corresponding induced flow solutions using our solution technique.

Chapter 8

Conclusions

Given plume theory was introduced by Zeldovich (1937) 80 years ago, it is remarkable that even today there is still scope to gain insight into a fundamental aspect of plumes, namely, their induced flows. The work in this thesis has aimed to bridge the gap in our understanding of induced flows, of which we had little knowledge of in comparison to the turbulent jet and plume flow, and further, to take advantage of recent advances that have occurred in our knowledge of turbulent plumes. With specific conclusions already drawn at the end of each chapter, the aim of this chapter is to provide some broader general conclusions and statements based on the overall body of work.

Taylor's seminal work in 1958 modelled the flows induced by the idealised line jet and idealised line plume. The flows are idealised in that they issue from line sources of infinite length and infinitesimal width with a source singularity in velocity and buoyancy, respectively. Taylor's solutions are based on solving Laplace's equation subject to a vertical distribution of line sinks that describe the jet/plume entrainment. In this thesis, we adopt an approach analogous to Taylor's to derive solutions for the potential flows induced by plumes issuing from a source in a horizontal boundary with a non-zero width and a finite source velocity and buoyancy. These non-idealised plume flows fall into one of three categories, namely, pure, forced or lazy. A pure plume is a straight-sided flow with a balance of inertia and buoyancy forces that is invariant with height. A forced plume has a deficit in buoyancy flux (or excess in momentum flux) at its source relative to the pure plume. It is straight-sided and has an (approximately) equal spreading rate to that of the pure plume. A lazy plume has an excess in buoyancy flux (or deficit in momentum flux) at its source relative to the pure plume. In contrast to the pure and forced plumes, this flow exhibits a near-source contraction when it is sufficiently lazy due to a strong buoyancy-induced acceleration, before proceeding to expand with a linear growth rate at greater heights. The solution for the induced flow

of the pure plume developed herein proved an immediate extension of Taylor's solutions. On applying the standard solution technique of the method of separation of variables, the induced flow was identified to be uniform and horizontal (figure 2.5). This flow pattern is consistent with the visualisation from Kotsovinos (1977) (figure 1.1 (a)) and observations from Rankine's wind tunnel experiments as discussed in Taylor (1961). Armed with the solution for the plume plume, the effect on the environment of the more complex forced and lazy plumes was investigated. In order to develop induced flow solutions for these non-pure plumes, an alternative solution technique was required. The theory of functions of a complex variable was exploited, an approach which had not previously been utilised to model plume induced flows. Owing to the contracting perimeter of the lazy plume, crucially, the distribution of line sinks describing the plume's entrainment was enforced along the plume perimeter, as opposed to along a vertical line. This required a novel conformal mapping to be devised. The resulting solution for the lazy plume indicates that the induced flow is upwardly inclined (figure 6.2). The solution for the forced plume shows that the induced flow exhibits a downward inclination (figure 4.9). These contrasting flow patterns are due to the differences in the vertical variation of the plume entrainment and the plume geometries. Moreover, in response to the local variation in the plume dynamics in non-pure plumes, it is also found that the inclination of their induced flows varies with height. Overall, the flows induced by non-idealised plumes generally exhibit one of three qualitatively distinct induced flow patterns, dependent on the plume source Richardson number. In addition to the flows induced by plumes above horizontal slots, the notionally lazy plume driven by a vertical off-source uniform supply of buoyancy has also been modelled. The solution indicates that the induced flow is upwardly inclined, and is thus consistent with the above classification.

The current solution technique based on the theory of functions of a complex variable proves a robust modelling approach. Though the induced flow solutions derived are dependent on the entrainment closures adopted, developments regarding entrainment functions that may occur in the future can be straightforwardly implemented using the current method. More specifically, a new entrainment model will lead to a new plume boundary condition that is simply to be input into the integral theorem, following which the associated conformal mapping is to be applied to obtain the induced flow solution. Carlotti & Hunt (2017) recently devised an improved model to the classic constant-α based formulation from Taylor (1945), the very first to describe the entrainment by lazy plumes. Their model accounts for the enhanced entrainment, as observed by Kaye & Hunt (2009), in highly lazy plumes above circular sources relative to their pure counterparts. Though we did not adopt their model in this thesis (for reasons outlined in Chapter 7), once this (or indeed any other) model has been validated for the plume above a horizontal slot, the induced flow solution

will be straightforward to derive. In contrast to the lazy plume, many developments have occurred since Taylor's work in the description of entrainment by forced plumes. The linear entrainment model proposed by Priestley & Ball (1955) and List & Imberger (1975) is the most widely applied model and was adopted when developing the forced plume induced flow solution. This model successfully attains the respective jet and plume flow characteristics in the limits of the forced plume, and leads to a plume that is straight-sided which is consistent with observations by Kotsovinos & List (1977). Though such a model provided the closure to the governing equations describing the forced plume and enabled the induced flow solution to be derived, the resulting solution has led to concerns regarding the appropriateness of the model. Arguments have been devised herein highlighting that this entrainment model (and subsequently numerous other entrainment formulations) exhibit some form of non-physical flow behaviour at, or close to, the source. These centre around solutions indicating that the plume flow fails to exhibit 'jet-like' flow behaviour immediately above the source. The plume is expected to behave as a jet close to the source, as the source momentum flux is dominant over the buoyancy-induced component in this region. Indeed Papanicolaou & List (1988) observe that 'jet-like' behaviour occurs within a characteristic 'jet-length' from the source for a forced plume. These insights gained have focussed the need for a new entrainment model.

The work in this thesis is co-sponsored by Dyson Ltd One area of interest to the company is the design and production of devices for cooling and heating in rooms, e.g. their 'Air Multiplier' which blows air from a nozzle. Although the company's focus thus far has been on directly exploiting a turbulent jet/plume flow to achieve their goal, knowledge of the induced flow could, for instance, enable a greater understanding of the bulk flow patterns driven by their devices. Further, our understanding is that the company's design process is currently centred around elegant experiments and computational simulations. The theoretical framework used in this thesis provides an additional facet which could potentially be exploited to complement their current approaches.

The models in this thesis are predictive and have not been fully validated. Validation has taken the form of comparisons with the available measurements from previously published work. As a next step, an experimental campaign is required to fully validate the models, as well as to serve as a guide for future mathematical modelling. Experiments are currently being undertaken within the research group focussing on investigating plume entrainment, lazy and forced, in addition to other aspects crucial to the modelling of induced flows. The latter includes questions regarding the assumption of two-dimensionality of a real plume and the role of the boundary layer along the horizontal boundary adjacent to the source. Investigation of these aspects of the flow relating directly to the modelling assumptions form

what can only be regarded as the vital next step of the work and are recommended prior to developing any new models.

To finish, one may briefly reflect on the concept of mathematical modelling, defined by Eykhoff (1972) as '*a representation of the essential aspects of an existing system (or a system to be constructed) which presents knowledge of that system in a usable form*'. Mathematical modelling has been exploited as the fundamental tool to predict and gain insight into induced flows throughout this thesis. It is the intention that this approach, together with the resulting physical insights gained into the flows examined, proves of use and of significance to readers with interests in the fluid mechanics of jets and plumes and analytical methods, whilst also providing a stepping stone for readers to tackle related questions and problems in the future.

References

Adams, E. & Trowbridge, J. (1985). Circulation induced by coastal diffuser discharge. *J. Waterway, Port, Coastal, and Ocean Eng.*, 111(6):973–984.

Antonia, R., Browne, L., Rajagopalan, S. & Chambers, A. (1983). On the organized motion of a turbulent plane jet. *J. Fluid Mech.*, 134:49–66.

Aynsley, R. (2007). Circulating fans for summer and winter comfort and indoor energy efficiency. Technical report, Environment Design Guide.

Baines, W. D. & Turner, J. S. (1969). Turbulent buoyant convection from a source in a confined region. *J. Fluid Mech.*, 37:51–80.

Baker, C. B., Maffe, A. J. & Taulbee, D. B. (1989). An analysis of the two-dimensional turbulent buoyant jet. *Chemical Engineering Communications*, 81:1–14.

Batchelor, G. (1969). *An introduction to fluid dynamics*. Cambridge Univ. Press.

Batchelor, G. K., Moffatt, H. K. & Worster, M. G. (2000). *Perspectives in fluid dynamics: a collective introduction to current research*. Cambridge Univ. Press.

Carlotti, P. & Hunt, G. R. (2005). Analytical solutions for turbulent non-boussinesq plumes. *J. Fluid Mech.*, 538:343–359.

Carlotti, P. & Hunt, G. R. (2017). An entrainment model for lazy turbulent plumes. *J. Fluid Mech.*, 811:682–700.

Caudwell, T., Flór, J.-B. & Negretti, M. E. (2016). Convection at an isothermal wall in an enclosure and establishment of stratification. *J. Fluid Mech.*, 799:448–475.

Cheesewright, R. (1967). Turbulent natural convection from a vertical plane surface. *J. Heat Transfer*, 90:1–6.

Chen, C. J. & Chen, C. H. (1979). On prediction and unified correlation for decay of vertical buoyant jets. *Trans. A.S.M.E. C: J. Heat Transfer*, 101(3):532–537.

Chen, C. J. & Rodi, W. (1980). Vertical turbulent buoyant jets: a review of experimental data. *N.A.S.A. STI/Recon. Technical Report A*, 80.

Cooper, P. & Hunt, G. R. (2010). The ventilated filling box containing a vertically distributed source of buoyancy. *J. Fluid Mech.*, 646:39–58.

Driscoll, T. A. & Trefethen, L. N. (2002). *Schwarz-Christoffel mapping*. Cambridge Univ. Press.

Eggers, J. & Smith, A. F. (2010). Free streamline flows with singularities. *J. Fluid Mech.*, 647:187–200.

Eykhoff, P. (1972). *System identification: parameter and state estimation*. John Wiley & Sons.

Fischer, H., List, E., Koh, R., Imberger, J. & Brooks, N. (1979). *Mixing in inland and coastal waters*. Academic Press.

Forthmann, E. (1936). Turbulent jet expansion. Technical report, N.A.C.A. Tech. Memo. No. 789.

George, W. K. & Capp, S. P. (1979). A theory for natural convection turbulent boundary layers next to heated vertical surfaces. *Int. J. Heat and Mass Transfer*, 22(6):813–826.

Giger, M. (1987). *Der ebene freistrahl in flachem wasser*. PhD thesis, Institut fur Hydromechanik und Wasserwirtschaft, E.T.H. Zurich.

Giger, M., Dracos, T. & Jirka, G. H. (1991). Entrainment and mixing in plane turbulent jets in shallow water. *J. Hydraulic Research*, 29(5):615–642.

Goldschmidt, V. & Eskinazi, S. (1966). Two-phase turbulent flow in a plane jet. *Trans. A.S.M.E. E: J. Appl. Mech.*, 33:735–747.

Görtler, H. (1942). Berechnung von aufgaben der freien turbulenz auf grund eines neuen näherungsansatzes. *Zeitschrift für Angewandte Mathematik und Mechanik*, 22:244–254.

Heskestad, G. (1965). Hot-wire measurements in a plane turbulent jet. *Trans. A.S.M.E. E: J. Appl. Mech*, 32:721–734.

Hölling, M. & Herwig, H. (2005). Asymptotic analysis of the near-wall region of turbulent natural convection flows. *J. Fluid Mech.*, 541:383–397.

Hossain, M. S. & Rodi, W. (1982). A turbulence model for buoyant flows and its application to vertical buoyant jets. *HMT: Sci. and App. Heat and Mass Trans.*, pages 121–178.

Hunt, G. R. (1994). *The fluid mechanics of the Aaberg exhaust hood*. PhD thesis, University of Leeds.

Hunt, G. R. & Coffey, C. J. (2010). Emptying boxes - classifying transient natural ventilation flows. *J. Fluid Mech.*, 646:137–168.

Hunt, G. R. & Ingham, D. B. (1992). The fluid mechanics of a two-dimensional Aaberg exhaust hood. *The Annals of Occupational Hygiene*, 36:455–476.

Hunt, G. R. & Kaye, N. B. (2005). Lazy plumes. *J. Fluid Mech.*, 533:329–338.

Hunt, G. R. & Kaye, N. G. (2001). Virtual origin correction for lazy turbulent plumes. *J. Fluid Mech.*, 435:377–396.

Hunt, G. R. & van den Bremer, T. S. (2011). Classical plume theory: 1937-2010 and beyond. *I.M.A. J. Applied Math.*, 76:424–448.

Ivanov, V. I. & Trubetskov, M. K. (1994). *Handbook of conformal mapping with computer-aided visualization*. CRC Press.

Jiji, L. M. (2006). *Heat convection*. Springer.

Jirka, G., Abraham, G. & Harleman, D. (1975). An assessment of techniques for hydrothermal prediction. Technical report, Ralph M. Parsons Laboratory for Water Res. and Hydrod., M.I.T.

Joshi, P. & Taylor, R. (1983). Circulation induced by tidal jets. *J. Waterway, Port, Coastal, and Ocean Eng.*, 109(4):445–464.

Kaye, N. B. & Hunt, G. R. (2009). An experimental study of large area source turbulent plumes. *Int. J. Heat and Fluid Flow*, 30:1099–1105.

Kaye, N. B. & Linden, P. F. (2004). Coalescing axisymmetric turbulent plumes. *J. Fluid Mech.*, 502:41–63.

Kerr, R. C. & McConnochie, C. D. (2015). Dissolution of a vertical solid surface by turbulent compositional convection. *J. Fluid Mech.*, 765:211–228.

Kotsovinos, N. E. (1975). *A study of the entrainment and turbulence in a plane buoyant jet*. PhD thesis, California Institute of Technology.

Kotsovinos, N. E. (1977). Plane turbulent buoyant jets. Part 2. Turbulence structure. *J. Fluid Mech.*, 81:45–62.

Kotsovinos, N. E. (1978). A note on the conservation of the axial momentum of a turbulent jet. *J. Fluid Mech.*, 87:55–63.

Kotsovinos, N. E. & Angelidis, P. B. (1991). The momentum flux in turbulent submerged jets. *J. Fluid Mech.*, 229:453–470.

Kotsovinos, N. E. & List, E. J. (1977). Plane turbulent buoyant jets. Part 1. Integral properties. *J. Fluid Mech.*, 81:25–44.

Lee, S. L. & Emmons, H. W. (1961). A study of natural convection above a line fire. *J. Fluid Mech.*, 11:353–368.

Linden, P. F. (1999). The fluid mechanics of natural ventilation. *Annu. Rev. Fluid Mech.*, 31:201–238.

Lippisch, A. M. (1958). Flow visualization. *Aero. Eng. Rev.*, 36:24–36.

List, E. J. (1982). Turbulent jets and plumes. *Annual Rev. Fluid Mech.*, 14:189–212.

List, E. J. & Imberger, J. (1973). Turbulent entrainment in buoyant jets and plumes. *Journal Hydraulics Division*, 99:1461–1474.

List, E. J. & Imberger, J. (1975). Turbulent entrainment in buoyant jets and plumes. *Journal Hydraulics Division*, 101:617–620.

Malin, M. R. (1987). The decay of mean and turbulent quantities in vertical forced plumes. *Appl. Math. Modelling*, 11:301–314.

Markushevich, A. I. & Silverman, R. A. (2005). *Theory of functions of a complex variable*. American Mathematical Soc.

McConnochie, C. D. & Kerr, R. C. (2016a). The effect of a salinity gradient on the dissolution of a vertical ice face. *J. Fluid Mech.*, 791:589–607.

McConnochie, C. D. & Kerr, R. C. (2016b). The turbulent wall plume from a vertically distributed source of buoyancy. *J. Fluid Mech.*, 787:237–253.

Melikov, A. K., Hanzawa, H. & Fanger, P. O. (1988). Airflow characteristics in the occupied zone of heated spaces without mechanical ventilation. *A.S.H.R.A.E. Transactions*, 94:52–70.

Miller, D. R. (1957). *Static pressure distribution in free turbulent jet mixing*. PhD thesis, Purdue University.

Morse, P. M. & Feshbach, H. (1953). *Methods of theoretical physics*. McGraw-Hill.

Morton, B. R. (1959). Forced plumes. *J. Fluid Mech.*, 5:151–163.

Morton, B. R. & Middleton, J. (1973). Scale diagrams for forced plumes. *J. Fluid Mech.*, 58:165–176.

Morton, B. R., Taylor, G. & Turner, J. S. (1956). Turbulent gravitational convection from maintained and instantaneous sources. *Proc. Roy. Soc. Lond. A: Math., Phys. and Eng. Sci.*, 234(1196):1–23.

Noutsopoulos, G. & Yannopoulos, P. (1987). The round vertical turbulent buoyant jet. *Journal of Hydraulic Research*, 25(4):481–502.

Paliouras, J. D. & Meadows, D. S. (1990). *Complex variables for scientists and engineers*. Macmillan Publishing Company.

Papanicolaou, P. N. & List, E. J. (1988). Investigations of round vertical turbulent buoyant jets. *J. Fluid Mech.*, 195:341–391.

Pham, M. V., Plourde, F. & Kim, S. D. (2005). Three-dimensional characterization of a pure thermal plume. *Trans. A.S.M.E. C: J. Heat Transfer*, 127:624–636.

Prandtl, L. (1904). On fluid motions with very small friction. In *Third International Mathematical Congress*, pages 484–491, Heidelberg, Germany.

Priestley, C. H. B. & Ball, F. K. (1955). Continuous convection from an isolated source of heat. *Quart. J. Royal Met. Soc.*, 81(348):144–157.

Quintiere, J. G. (1997). *Principles of fire behaviour*. Delmar Cengage Learning.

Rajaratnam, N. (1976). *Turbulent jets*. Elsevier Scientific Pub. Co.

Ramaprian, B. R. & Chandrasekhara, M. S. (1983). Study of vertical plane turbulent jets and plumes. Technical report, Iowa Institute of Hydraulic Research, The University of Iowa.

Reichardt, H. (1942). Einige im kleinen überall lösbare, im großen unlösbare diophantische gleichungen. *Journal für die reine und angewandte Mathematik*, 184:12–18.

Riley, K. F., Hobson, M. P. & Bence, S. J. (2006). *Mathematical methods for physics and engineering: a comprehensive guide*. Cambridge Univ. Press.

Rooney, G. G. (2015). Merging of a row of plumes or jets with an application to plume rise in a channel. *J. Fluid Mech.*, 771:1–12.

Rouse, H., Yih, C. S. & Humphreys, H. W. (1952). Gravitational convection from a boundary source. *Tellus*, 4(3):201–210.

Rubin, M. (1982). Calculating heat transfer through windows. *Int. J. Energy Research*, 6(4):341–349.

Schlichting, H. (1968). *Boundary-layer theory*. McGraw-Hill, 6th edition.

Schneider, W. (1981). Flow induced by jets and plumes. *J. Fluid Mech.*, 108:55–65.

Schneider, W. (1985). Decay of momentum flux in submerged jets. *J. Fluid Mech.*, 154:91–110.

Setchi, A. (2012). *Mathematical modelling of flow through shunts: application to patent ductus arteriosus and side-to-side anastomosis*. PhD thesis, Imperial College London.

Spiegel, M. R. (1964). *Schaum's outlines: complex variables*. McGraw-Hill.

Taylor, G. I. (1945). Dynamics of a mass of hot gas rising in air. Technical report, U.S. Atomic Energy Commission, MDDC 919, LADC 276.

Taylor, G. I. (1958). Flow induced by jets. *J. Aerospace Sciences*, 25:464–465.

Taylor, G. I. (1961). Fire under influence of natural convection. In *International symposium on the use of models in fire research*, pages 10–31, National Academy of Sciences, Washington D.C.

Tollmein, W. (1926). Calculation of turbulent expansion processes. *Z. Agnew. Math. Mech.*, 6:468–478.

Townsend, A. A. (1976). *The structure of turbulent shear flow*. Cambridge Univ. Press.

Tsuji, T. & Nagano, Y. (1988). Characteristics of a turbulent natural convection boundary layer along a vertical flat plate. *Int. J. Heat and Mass Transfer*, 31(8):1723–1734.

Tsuji, T. & Nagano, Y. (1989). Velocity and temperature measurements in a natural convection boundary layer along a vertical flat plate. *Experimental Thermal and Fluid Science*, 2(2):208–215.

Turner, J. S. (1979). *Buoyancy effects in fluids.* Cambridge Univ. Press.

van den Bremer, T. S. & Hunt, G. R. (2014). Two-dimensional planar plumes and fountains. *J. Fluid Mech.*, 750:210–244.

van der Hegge Zijnen, B. G. (1958). Measurements of the velocity distribution in a plane turbulent jet of air. *Appl. Sci. Res.*, 7:256–276.

van Dyke, M. (1982). *An album of fluid motion*. The Parabolic Press.

van Reeuwijk, M. & Craske, J. (2015). Energy-consistent entrainment relations for jets and plumes. *J. Fluid Mech.*, 782:333–355.

van Reeuwijk, M., Salizzoni, P., Hunt, G. R. & Craske, J. (2016). Turbulent transport and entrainment in jets and plumes: a DNS study. *Physical Review Fluids*, 1:074301.

Vliet, G. & Liu, C. (1969). An experimental study of turbulent natural convection boundary layers. *J. Heat Transfer*, 91:517–531.

Wang, H. & Law, A. W. (2002). Second-order integral model for a round turbulent buoyant jet. *J. Fluid Mech.*, 459:397–428.

Wells, A. J. & Worster, M. G. (2008). A geophysical-scale model of vertical natural convection boundary layers. *J. Fluid Mech.*, 609:111–137.

Yannopoulos, P. & Noutsopoulos, G. (1990). The plane vertical turbulent buoyant jet. *J. Hydraulic Research*, 28(5):565–580.

Yannopoulos, P. C. (2006). An improved integral model for plane and round turbulent buoyant jets. *J. Fluid Mech.*, 547:267–296.

Yih, C. S. (1951). Free convection due to a point source of heat. In *Proc. First U.S. Nat. Cong. Appl. Mech.*, pages 941–947.

Yuana, L. M. & Cox, G. (1996). An experimental study of some line fires. *Fire Safety J.*, 27(2):123–139.

Zeldovich, Y. B. (1937). The asymptotic laws of freely-ascending convective flows. *Zhur. Eksper. Teor. Fiz.*, 7:1463–1465.

Appendix A

Evaluating the coefficients ε_{p} and ε_{j}

A.1 ε_{p} - Plume conservation equations

The integral approach, originally formulated by Zeldovich (1937) and popularised by Morton et al. (1956) to describe plumes above circular sources, was adopted by Lee & Emmons (1961) to describe the plume above a slender horizontal slot. In this section, we determine the plume coefficient, ε_{p} (2.8), based on the solution from Lee & Emmons (1961). We broadly outline the general steps followed to obtain the solution from Lee & Emmons (1961). Note that it is not our intention to provide a formal derivation.

The plumes considered have a high Rayleigh number, signifying that the destabalising effects of buoyancy in the flow are large relative to the stabalising effects of viscosity. Rouse et al. (1952) experimentally observed that time-averaged cross-sectional profiles of streamwise velocity, w, and buoyancy, g', at multiple downstream locations in these plumes have a similar geometrical shape; with the profiles decreasing exponentially from a maximum along their centre-lines. Further, they identified that normalising the streamwise velocity or buoyancy and transverse distance across the plume width by suitable scales resulted in the profiles collapsing onto a single (dimensionless) universal curve. This is the property of self-similarity and it forms a key basis of the model for the plume devised by Lee & Emmons (1961). Lee & Emmons (1961) describe the plume using a set of ordinary differential equations in terms of fluxes defined on integrating quantities across the flow's horizontal cross-section. To derive these equations, we first reduce the (double-averaged) Navier-Stokes equations to

$$w_x \frac{\partial w_y}{\partial x} + w_y \frac{\partial w_y}{\partial y} = \frac{1}{\rho_{\mathrm{o}}}(\rho g - \frac{dp}{dy}) = g', \tag{A.1}$$

where $g' = g(\rho - \rho_{\mathrm{a}})/\rho_{\mathrm{a}}$ with g denoting the gravitational acceleration and ρ and ρ_{a} representing the densities of the plume and ambient, respectively. A Cartesian coordinate system

(x,y) is adopted and the terms w_x and w_y denote the corresponding velocity components. The equation (A.1) indicates that the plume is driven by the source supply of buoyancy. A number of assumptions have been made in deriving the equation in (A.1). Specifically, the plume is long and thin, and that the dominant effect of the buoyancy forces over diffusive effects in a high Rayleigh number flow enable an inviscid approximation to be applied. With large vertical pressure gradients relative to transverse pressure gradients in a thin plume, the pressure in the plume is modelled using the pressure distribution in the ambient. Assuming the ambient is stationary to first-order, a hydrostatic pressure, $dp/dy = -\rho_{\mathrm{a}}g$, is assumed. Finally, a Boussinesq approximation is enforced, as the density differences between the plume and ambient are assumed small, i.e. $(\rho - \rho_{\mathrm{a}})/\rho_{\mathrm{a}} << 1$, implying that density variations can be ignored in all terms excluding that of the driving buoyancy force of the plume. To supplement the equation in (A.1), we state the continuity equation for an incompressible flow is given by

$$\frac{\partial w_x}{\partial x} + \frac{\partial w_y}{\partial y} = 0. \tag{A.2}$$

Using expressions (A.1) and (A.2), Lee & Emmons (1961) derive

$$\frac{dQ}{dy} = 2u_{\mathrm{e}} = 2^{3/2}\alpha\frac{M}{Q}, \quad \frac{dM}{dy} = \pi^{1/2}g'_{\mathrm{m}}b = \frac{BQ}{M} \tag{A.3}$$

to describe the plume in an otherwise quiescent ambient. These ordinary differential equations, which correspond to the conservation of volume and momentum, are expressed in terms of

$$Q = 2\int_0^\infty w_y dx = \pi^{1/2}w_{\mathrm{m}}b, \quad M = 2\int_0^\infty {w_y}^2 dx = 2^{-1/2}\pi^{1/2}{w_{\mathrm{m}}}^2 b, \tag{A.4}$$

and

$$B = 2\int_0^\infty g' w_y dx = 2^{-1/2}\pi^{1/2}w_{\mathrm{m}}g'_{\mathrm{m}}b \tag{A.5}$$

denoting the integral fluxes of volume, momentum and buoyancy per unit density and length, respectively. The integrals in (A.4) and A.5) have been evaluated on assuming self-similar Gaussian profiles for the vertical velocity and buoyancy, given by

$$w_y(x,y) = w_{\mathrm{m}}(y)e^{-x^2/b^2}, \quad g'(x,y) = g'_{\mathrm{m}}(y)e^{-x^2/b^2}, \tag{A.6}$$

where b denotes the transverse distance at which the properties fall to $1/e$ of their centre-line value and '$(\cdot)_{\mathrm{m}}$' corresponds to the value at the centre-line. Lee & Emmons (1961) include a

third equation,

$$\frac{dB}{dy} = 0 \tag{A.7}$$

(see Batchelor et al. (2000) for derivation), indicating that the plume buoyancy flux is invariant with height in a uniform environment. The governing equations in (A.3) and (A.7) require a closure describing the entrainment velocity u_e. Lee & Emmons (1961) have adopted the expression originally proposed by Taylor (1945),

$$u_e = \alpha w_m, \tag{A.8}$$

stating that the locally entrained velocity, u_e, is a fixed proportion, determined by the entrainment constant α, of the local characteristic vertical velocity in the plume w_m. The entrainment coefficient α must be determined empirically. It has been measured to take an average value of $\alpha = 0.13$ for pure plumes (see Chapter 2).

Lee & Emmons (1961) solve the governing equations in (A.3) and (A.7) subject to the source conditions for an (idealised) line plume of buoyancy, namely

$$Q = 0, \quad M = 0, \quad B = B_0 \ \text{ at } \ y = 0, \tag{A.9}$$

to obtain

$$Q = 2\alpha^{2/3} {B_0}^{1/3} y, \quad M = 2^{1/2} \alpha^{1/3} {B_0}^{2/3} y. \tag{A.10}$$

With the flux Q equivalent to the stream function χ and the induced flow modelled on one side of the line plume, we halve the expression for Q in (A.10) to obtain

$$\chi = \alpha^{2/3} {B_0}^{1/3} y. \tag{A.11}$$

On comparing this expression with the plume boundary condition given in (2.4), we determine the plume coefficient as

$$\varepsilon_p = {\alpha_p}^{2/3} \tag{A.12}$$

on setting $\alpha = \alpha_p$.

The integral equations governing a jet can be straightforwardly identified by setting $g'_m = 0$ in the conservation equations (A.3), resulting in

$$\frac{dQ}{dy} = 2u_e = 2^{3/2} \alpha \frac{M}{Q}, \quad \frac{dM}{dy} = 0, \tag{A.13}$$

with $\alpha = \alpha_j$. The entrainment coefficient has been measured to take an average value of $\alpha_j = 0.05$ for jets (see Chapter 2). The conserved momentum flux here is consistent with the

solution from Görtler (1942) in §A.2. The ordinary differential equations in (A.13) can be solved, subject to the source conditions for the (idealised) line jet, namely

$$Q = 0, \quad M = M_0 \text{ at } y = 0, \tag{A.14}$$

to obtain

$$Q = 2^{5/4}\alpha^{1/2}{M_0}^{1/2}y^{1/2}. \tag{A.15}$$

Noting again the equivalence between Q and the stream function χ, and with the induced flow modelled on one side of the line jet, we have

$$\chi = 2^{1/4}\alpha^{1/2}M^{1/2}y^{1/2}. \tag{A.16}$$

On comparing this expression with that of the jet boundary condition given in (2.3), we determine the jet coefficient as

$$\varepsilon_j = 2^{1/4}{\alpha_j}^{1/2}. \tag{A.17}$$

A.2 ε_j - Görtler (1942)

Schlichting (1968) outlines the solution, originally formulated by Görtler (1942), to describe a turbulent jet issuing from a slender slot. We have used this solution to express the jet coefficient ε_j (2.10) in terms of the jet spreading rate σ, as shown in the following.

Forthmann (1936) observed that jets exhibit self-similar behaviour, as time-averaged cross-sectional profiles of streamwise velocity collapse onto a single curve once suitably scaled. As will become evident when subsequently formulating the solution, this property of the jet allows for an assumed self-similar form of solution, and thus enables the original governing system of partial differential equations describing the jet to be reduced to a set of ordinary differential equations.

Based on an order of magnitude analysis of a long slender turbulent jet, the Reynolds stresses, streamwise velocity and its transverse gradient are large relative to all other components of the flow. As a result, the governing (double-averaged) Navier-Stokes equations describing the turbulent jet are reduced by applying the classic shear-layer approximation proposed by Prandtl (1904). Following Schlichting (1968), introducing the local Cartesian coordinates (x,y), with w_x and w_y denoting the corresponding velocity components, the jet is represented using

$$w_x\frac{\partial w_y}{\partial x} + w_y\frac{\partial w_y}{\partial y} = \frac{1}{\rho}\frac{\partial \tau}{\partial x} \tag{A.18}$$

and the continuity equation (A.2), subject to the boundary conditions

$$w_y \to 0 \quad \text{as} \quad x \to \infty, \tag{A.19}$$

$$\frac{\partial w_y}{\partial x} = 0 \quad \text{and} \quad w_x = 0 \quad \text{when} \quad x = 0. \tag{A.20}$$

The term τ on the right-hand side of (A.18) models the frictional shear-stresses imparted on the flow. In a turbulent flow, this is a dominated by 'virtual' Reynolds stresses attributed to unsteady fluctuations in the flow. In order to solve the governing equations (A.2) and (A.18) - (A.20), one must relate these Reynolds stresses to the mean flow, i.e. provide a turbulence closure. One of the simplest and most commonly employed closures is Prandtl's hypothesis, which is given by

$$\tau = \rho \varepsilon_t \frac{\partial w_y}{\partial x}, \tag{A.21}$$

where ρ is the density of the jet. The term ε_t in (A.21) denotes an eddy viscosity. It is modelled using Prandtl's constant momentum transfer mixing-length model as

$$\varepsilon_t \propto b w_m. \tag{A.22}$$

The formulation in (A.22) models the characteristic mixing length, denoting the distance a fluid particle will conserve a given property before mixing with the surrounding fluid, as proportional to the width of the jet b. The expression also states that the eddy viscosity ε_t remains fixed over a given cross-section of the jet, which implies that the momentum of a fluid particle is conserved across the width. Prandtl's hypothesis (A.21) is preferred in many situations over its more complex counterparts, for example the mixing length model used in the alternative solution given by Tollmein (1926), as it is simpler whilst maintaining close agreement with empirical observations (as shown in Rajaratnam (1976)). Other more sophisticated turbulence models, such as the $k-W$ model employed by Malin (1987), require numerical treatment and provide little improvement in accuracy.

To solve the governing boundary value problem, Goertler (1942) begins by expressing the jet centre-line velocity w_m and width b relative to their respective values at some fixed characteristic streamwise distance l from the source,

$$w_m = w_{ml} \left(\frac{y}{l}\right)^{-1/2}, \qquad b = b_l \left(\frac{y}{l}\right) \tag{A.23}$$

where the subscript '$(\cdot)_l$' denotes the value of the respective property at the streamwise distance l. These expressions are formulated as a result of the idealised nature of the source, which exhibits an infinite streamwise source velocity. Using the definitions in (A.23), the

eddy viscosity can be represented as

$$\varepsilon_{\mathrm{t}} = \varepsilon_{\mathrm{t}l} \left(\frac{y}{l}\right)^{1/2}, \quad \text{with} \quad \varepsilon_{tl} \propto b_l w_{\mathrm{m}l}. \tag{A.24}$$

Utilising the property of self-similarity, which has been observed for streamwise velocity profiles in the jet, and the definitions in (A.23) - (A.24), Görtler (1942) proposes the form of solution, in terms of the stream function χ, as

$$\chi = \frac{w_{\mathrm{m}l} l^{1/2}}{\sigma} y^{1/2} J(\eta), \quad \text{where} \quad \eta = \frac{\sigma x}{y} \tag{A.25}$$

represents a similarity coordinate expressed in terms of the two independent variables, and σ denotes a constant. The function J in (A.25) defines the shape of the stream function profile, and its coefficient determines the magnitude of the profile. By substituting the derivatives of expression (A.25), corresponding to the horizontal and vertical velocities, into expression (A.18), and then utilising continuity (A.2), Görtler (1942) derives the equation

$$\frac{1}{2}\left(\frac{\partial J}{\partial \eta}\right)^2 + \frac{1}{2} J \left(\frac{\partial^2 J}{d\eta^2}\right) + \frac{\varepsilon_{\mathrm{t}l}\sigma^2}{w_{\mathrm{m}l} l}\left(\frac{\partial^3 J}{d\eta^3}\right) = 0. \tag{A.26}$$

Evidently, the original governing partial differential equations have now been reduced to an ordinary differential equation. The corresponding boundary conditions for (A.26), equivalent to (A.19) and (A.20), are

$$\frac{\partial J}{\partial \eta} \to 0 \quad \text{as} \quad \eta \to \infty \tag{A.27}$$

and

$$J = 0, \quad \frac{\partial J}{\partial \eta} = 1 \quad \text{on} \quad \eta = 0, \tag{A.28}$$

respectively. Utilising the free constant available in the eddy viscosity model (A.22), Görtler (1942) proposes

$$\sigma = \frac{1}{2}\left(\frac{w_{\mathrm{m}l} l}{\varepsilon_{\mathrm{t}l}}\right)^{1/2}. \tag{A.29}$$

Using this expression, (A.26) can be reduced and integrated twice to give

$$\frac{\partial J}{\partial \eta} + J^2 = 1. \tag{A.30}$$

This first-order ordinary differential equation has solution

$$J = \tanh(\eta). \tag{A.31}$$

Having identified the shape function, attention turns to its coefficient in (A.25). On integrating the governing equations, the local flux of momentum M is found to be conserved along the jet, with

$$M = 2\int_0^\infty w^2 \,\mathrm{d}y = M_0 = \frac{4}{3}\frac{l}{\sigma}{w_m}_l{}^2. \tag{A.32}$$

Using this relation, the coefficient in (A.25) can be reformulated in terms of the source value M_0, to give the final form of solution

$$\chi = \frac{1}{2}\left(\frac{3M_0}{\sigma}\right)^{1/2} y^{1/2}\tanh(\eta). \tag{A.33}$$

The streamwise velocity, determined upon differentiating (A.33) with respect to the horizontal coordinate x, is

$$w = \frac{3^{1/2}}{2}{M_0}^{1/2}\sigma^{1/2}y^{-1/2}\,(1-\tanh^2\eta). \tag{A.34}$$

The constant σ denotes the jet spreading rate and it has been determined empirically by Reichardt (1942) as $\sigma = 7.67$. Schlichting (1968) states that there is very close agreement between the theoretical profile of velocity in (A.34) and experimental measurements from Forthmann (1936).

In order to use the solution given by Görtler (1942) to formulate a boundary condition for the flow induced by the (idealised) line jet, the stream function in (A.33) is evaluated at the perimeter of the jet, corresponding to $x \to \infty$. With $\tanh(\eta) \to 1$ as $x \to \infty$, expression (A.33) reduces to

$$\chi = \frac{3^{1/2}}{2}\left(\frac{M_0}{\sigma}\right)^{1/2} y^{1/2}. \tag{A.35}$$

This expression is equivalent to (half of) the volume flux of the jet. On comparing equation (A.35) with that for the jet boundary condition given in (2.3), we identify that

$$\varepsilon_j = 3^{1/2}\sigma^{-1/2}/2. \tag{A.36}$$

Appendix B

Γ-centred formulation

Based on the approach originally developed by Hunt & Kaye (2005), van den Bremer & Hunt (2014) recast the plume conservation equations from Lee & Emmons (1961) presented in §A.1 in Appendix A to model plumes above slender horizontal slots. Specifically, the approach recasts the equations originally expressed in terms of the (dimensional) fluxes Q, M and B and the vertical coordinate y, into corresponding equations in terms of the dimensionless variables, the local Richardson number Γ (2.17), width $\bar{b}$, velocity $\bar{w}$ and height ζ. The resulting dimensionless equations form the starting point for the derivation of the plume boundary conditions in Chapters 4 and 6.

The plume conservation equations from Lee & Emmons (1961), assuming Gaussian profiles for velocity and buoyancy, are given by

$$\frac{dQ}{dy} = 2u_\mathrm{e} = 2^{3/2}\alpha_\mathrm{p}\frac{M}{Q}, \quad \frac{dM}{dy} = \pi^{1/2}g'_\mathrm{m}b = \frac{BQ}{M}, \quad \frac{dB}{dy} = 0, \tag{B.1}$$

subject to the source conditions for a (non-idealised) plume above a slender horizontal slot, i.e.

$$Q = Q_0, \quad M = M_0, \quad B = B_0 \quad \text{at} \quad y = 0. \tag{B.2}$$

For convenience we first non-dimensionalise the equations in terms of the variables,

$$q = \frac{Q}{Q_0}, \quad m = \frac{M}{M_0}, \quad f = \frac{B}{B_0}, \quad \zeta = \frac{2\alpha_\mathrm{p}}{\pi^{1/2}}\frac{y}{b_0}, \tag{B.3}$$

to obtain

$$\frac{dq}{d\zeta} = \frac{m}{q}, \quad \frac{dm}{d\zeta} = \Gamma_0\frac{fq}{m}, \quad \frac{df}{d\zeta} = 0. \tag{B.4}$$

Expressing the local Richardson number, width and velocity in terms of the dimensionless fluxes defined in (B.3), as

$$\Gamma = \Gamma_0 \frac{f q^3}{m^3}, \quad \bar{b} = \frac{q^2}{m}, \quad \bar{w} = \frac{m}{q}, \tag{B.5}$$

we derive the equations

$$\frac{d\Gamma}{d\zeta} = \frac{3\Gamma(1-\Gamma)}{\bar{b}}, \quad \frac{d\bar{b}}{d\zeta} = 2-\Gamma, \quad \frac{d\bar{w}}{d\zeta} = \frac{\bar{w}}{\bar{b}}(\Gamma - 1) \tag{B.6}$$

as in van den Bremer & Hunt (2014). The plume source conditions corresponding to (B.2) are

$$\Gamma = \Gamma_0, \ \ \bar{b} = 1, \ \ \bar{w} = 1 \ \text{ at } \ \zeta = 0. \tag{B.7}$$

Appendix C

Schwarz-Christoffel theorem

The Riemann Mapping Theorem (Markushevich & Silverman, 2005) states that there exists a unique function that conformally maps between the upper-half plane and the interior region of a polygon in the complex domain. The Schwarz-Christoffel formula, given (in integral form) by

$$\omega(z) = A + C\int_{z_0}^{z}\prod_{k=1}^{n-1}(\zeta - z_k)^{\nu_k - 1}d\zeta \tag{C.1}$$

(Paliouras & Meadows, 1990), explicitly determines such a mapping. Here, the analytic function, ω, denotes a one-to-one mapping of the real coordinates z_k along the real-axis of the upper-half plane onto the vertices ω_k of the polygon, i.e. $\omega(z_k) = \omega_k$ for $k = 1,\ ...,\ n-1$ and $\omega(\infty) = \omega_n$ (where n denotes the number of vertices of the polygon). The term $\nu_k\pi$ corresponds to the interior angles of the polygon, and A and B represent complex constants to be found. Note that the coordinates z_k input into (C.1) must be predetermined.

The Schwarz-Christoffel theorem is not restricted to closed polygons, and can be applied when considering unbounded or partially-bounded domains (Paliouras & Meadows, 1990). In these scenarios, we denote the region at infinity using an additional vertex. To identify the interior angle associated with this vertex, we utilise the condition that the sum of all interior angles in an unbounded or bounded polygon must be $(n-2)\pi$, or equivalently,

$$\sum_{k=1}^{n}\nu_k = n - 2. \tag{C.2}$$

As an example, we utilise the Schwarz-Christoffel theorem in (C.1) to identify the (inverse) mapping (4.23) in Chapter 4 that maps between the upper-half plane and a straight-sided wedge with internal angle $\gamma\pi$ (see also Spiegel (1964)). To begin, we note that the induced flow in this instance occupies a semi-infinite region. Thus, we use expression (C.2)

to determine the angle associated with the vertex located at infinity as $-\gamma\pi$. This vertex, however, also corresponds to a point at infinity in the Z-plane. Equation (C.1) has been proven to be independent of points located at infinity in the Z-plane (see, e.g. Paliouras & Meadows (1990)), and thus the vertex does not contribute as an input in the Schwarz-Christoffel theorem. Inputting the interior angle $v_1\pi = \gamma\pi$ associated with the vertex located at the coordinate origin of the complex plane into (C.1), we obtain

$$\begin{aligned} \omega(z) &= A + C\int_{z_0}^{z} \zeta^{\gamma-1} d\zeta \\ &= A + (C/\gamma)\cdot(z-z_0)^{\gamma}. \end{aligned} \tag{C.3}$$

The origins of both the upper-half plane and the induced flow domain coincide. This is equivalent to satisfying the boundary condition $\omega(0) = 0$, which is achieved on selecting $A = 0$ and $z_0 = 0$ in (C.3). The constant C/γ is arbitrarily chosen to take a unit value, as it does not affect the general regions that are mapped, but instead the location of specific coordinates within them. Thus, the final form of the mapping is identified as

$$\omega(z) = z^{\gamma}. \tag{C.4}$$

The corresponding forward mapping is straightforwardly identified as

$$z(\omega) = \omega^{1/\gamma}. \tag{C.5}$$

In our example in §2.3.3 in Chapter 2, where the metal plate corresponds to a quadrant in the W-plane (with interior angle $\pi/2$), the exponent in (C.4) and (C.5) takes the value $\gamma = 1/2$.

Appendix D

Derivation of radius of 'unit contour'

From the solutions for the line jet and line plume derived in Appendix A, the local volume flux of the plume and jet are given by

$$Q_\mathrm{p} = 2{\alpha_\mathrm{p}}^{2/3}{B_0}^{1/3}y, \quad Q_\mathrm{j} = \left(\frac{3}{\sigma}\right)^{1/2}{M_0}^{1/2}y^{1/2} \tag{D.1}$$

(cf. Görtler (1942), Lee & Emmons (1961)). As the the focus here is to compare the effect that the jet and plume have on their environments, we consider their corresponding entrained velocities

$$u_\mathrm{e} = \frac{1}{2}\frac{dQ_\mathrm{p}}{dy} = {\alpha_\mathrm{p}}^{2/3}{B_0}^{1/3}, \quad u_\mathrm{e} = \frac{1}{2}\frac{dQ_\mathrm{j}}{dy} = \left(\frac{3}{16\sigma}\right)^{1/2}{M_0}^{1/2}y^{-1/2}. \tag{D.2}$$

These expressions specifically model the horizontal component of the entrained flow. To account for any inclination in the induced flow, as in the case of the jet illustrated in figure 2.3, the entrainment velocities in (E.2) are modified to

$$u_\mathrm{e} = \frac{1}{2\cos\theta_\mathrm{p}}\frac{dQ_\mathrm{p}}{dy} = \frac{1}{\cos\theta_\mathrm{p}}{\alpha_\mathrm{p}}^{2/3}{B_0}^{1/3}, \quad u_\mathrm{e} = \frac{1}{2\cos\theta_\mathrm{j}}\frac{dQ_\mathrm{j}}{dy} = \frac{1}{\cos\theta_\mathrm{j}}\left(\frac{3}{16\sigma}\right)^{1/2}{M_0}^{1/2}y^{-1/2}. \tag{D.3}$$

These expressions represent the horizontal velocity components of the induced flow at the jet and plume perimeters, with θ_p and θ_j denoting the respective inclinations of the streamlines. With the velocities of the entrained flows identified, the expressions in (E.3) are equated and rearranged to determine the radius r_u of the 'unit' contour, i.e.

$$\frac{1}{\cos\theta_\mathrm{p}}{\alpha_\mathrm{p}}^{2/3}{B_0}^{1/3} = \frac{1}{\cos\theta_\mathrm{j}}\left(\frac{3}{16\sigma}\right)^{1/2}{M_0}^{1/2}y^{-1/2} \quad \Rightarrow \quad y = r_\mathrm{u} = \frac{3M_0}{16\sigma{B_0}^{2/3}{\alpha_\mathrm{p}}^{4/3}}\frac{\cos^2\theta_\mathrm{p}}{\cos^2\theta_\mathrm{j}}. \tag{D.4}$$

Appendix E

Method for numerical solution

To verify the accuracy of the solutions for the flows induced by the lazy and forced plumes in Chapters 4 and 6, respectively, the corresponding governing boundary value problems were solved numerically using a finite-difference scheme. In the following we provide an overview of the numerical method. For further details on the method we guide the reader to §4.3.1 and §4.3.2 in Hunt (1994).

To solve an elliptic boundary value problem numerically, an additional boundary condition is required to supplement those used to develop the analytical solution. Specifically, a boundary condition is enforced along the outer curved perimeter of the numerical domain,

$$R = R_\infty \quad \text{from} \quad 0 < \theta < \pi/2, \tag{E.1}$$

where $R = (\Delta^2 + \zeta^2)^{1/2}$ denotes the dimensionless radial coordinate and $R_\infty >> 1$. The form of the boundary condition is specified using the analytical asymptotic (far-field) solution to the governing boundary value problem. For the induced flow, the asymptotic solution is obtained on solving the Laplace equation (4.20) subject to the streamline boundary condition (4.21) and the plume boundary condition ((4.19) for the lazy plume or (6.14) for the forced plume) as $\zeta \to \infty$. The plume boundary condition for both the lazy and forced plume at such a height is given by

$$\Psi = \frac{1}{2}\Gamma_0^{1/3}\zeta \quad \text{at} \quad \theta = \pi/2. \tag{E.2}$$

Following the method of separation of variables (see §5.2), we derive the asymptotic induced flow solution,

$$\Psi = \frac{\pi - 2\theta}{2\pi} + \frac{1}{2}\Gamma_0^{1/3} R\sin\theta, \tag{E.3}$$

which is used to specify the outer numerical boundary condition.

To obtain a numerical solution for the induced flow, a mesh is placed over the entire solution domain. The mesh was chosen to be sufficiently fine so as to ensure that the results were mesh independent. Further, as we require the domain to cover a sufficiently large radial distance in order to accurately implement the outer boundary condition and confirm that it does not incorrectly influence the flow, a transformation was adopted of the form $\bar{R} = R^a$ (where $a < 1$). This enabled the mesh size to be increased in the radial direction by a power $1/a$. Using such a transformation we derive the (transformed) Laplace equation

$$\frac{\partial^2 \Psi}{\partial \bar{R}^2} + \frac{a(a-1)+a}{a^2} \frac{1}{\bar{R}} \frac{\partial \Psi}{\partial \bar{R}} + \frac{1}{a^2} \frac{1}{\bar{R}^2} \frac{\partial^2 \Psi}{\partial \theta^2} = 0. \tag{E.4}$$

Note that a value of $a = 1/4$ is adopted when verifying the induced flow solutions in Chapters 4 and 6.

Defining the grid points in the $(\bar{R}, \theta)$ plane by the points of intersection of the circles $\bar{R} = k\delta\bar{R}$ $(k = 1, 2, ..p)$ and lines $\theta = m\delta\theta$ $(m = 1, 2, ..s)$, we approximate the solution to the transformed Laplace equation (E.4) at the points (k, m) using the finite-difference formula,

$$D_1 \Psi_{k-1,m} + D_4 \Psi_{k,m+1} - D_3 \Psi_{k,m} + D_2 \Psi_{k+1,m} + D_4 \Psi_{k,m-1} = 0, \tag{E.5}$$

where the coefficients D_1, D_2, D_3 and D_4 are given by

$$D_1 = (k\delta\bar{R})^{2(a-1)/a} \left(a^2 - \frac{a(a-1)+a}{2k} \right), \; D_2 = (k\delta\bar{R})^{2(a-1)/a} \left(a^2 + \frac{a(a-1)+a}{2k} \right), \tag{E.6}$$

$$D_3 = 2k^{-2/a} (\delta\bar{R})^{2(a-1)/a} \left(k^2 a^2 + \frac{1}{(\Delta\theta)^2} \right), \; D_4 = \frac{k^{-2/a} (\delta\bar{R})^{-2(a-1)/a}}{(\delta\theta)^2}. \tag{E.7}$$

The formulation of (E.5) is based on applying a central-difference approximation for the derivatives. To solve for the induced flow at the grid points, we apply (E.5) in an iterative Successive Over-Relaxation (S.O.R.) form, specified by

$$\Psi^{n+1}_{k,m} = \Psi^{n}_{k,m} + \frac{c}{D_3} \left(D_1 \Psi^{n+1}_{k-1,m} + D_4 \Psi^{n}_{k,m+1} + D_2 \Psi^{n}_{k+1,m} + D_4 \Psi^{n+1}_{k,m-1} - D_3 \Psi^{n}_{k,m} \right), \tag{E.8}$$

where c is the relaxation parameter and n denotes the number of iterations.

Appendix F

Derivation of α and Γ - Yannopoulos & Noutsopoulos (1990)

In this section we derive the expressions for the entrainment coefficient α and local Richardson number Γ for the model formulated by Yannopoulos & Noutsopoulos (1990) describing the forced plume above a horizontal slot.

F.1 Entrainment coefficient α

Yannopoulos & Noutsopoulos (1990) adopt the entrainment closure,

$$\phi = \left(\frac{K_w^2 + K_c^2}{K_w} \right)^{1/2}, \tag{F.1}$$

when modelling the plume flow above a horizontal slot, where the terms $K_w = b_w/y$ and $K_c = b_c/y$ denote the spreading coefficients of velocity and tracer concentration (equivalent to a scaled buoyancy flux), respectively. Specifying spreading coefficients to close the governing equations is an alternative to using the entrainment coefficient α. Solving the plume conservation equations for volume, momentum and concentration with (F.1), Yannopoulos & Noutsopoulos (1990) derive the expression for the centre-line plume velocity

$$w_{\mathrm{m}} = \frac{2^{3/4}}{\pi^{1/4}} \frac{w_0 {b_0}^{1/2}}{{K_w}^{1/2}} y^{-1/2} \left(1 + \frac{8R_0}{5} + \frac{\pi^{1/4}}{2^{7/4}} \frac{\phi R_0}{{b_0}^{3/2}} y^{3/2} \right)^{1/3}. \tag{F.2}$$

Uniform profiles are assumed at the source as the model accounts for a near-source flow development region. The term R_0 in (F.2), defined in (7.4) in Chapter 7, corresponds to an alternative source Richardson number. To determine the entrainment coefficient that is

equivalent to (F.1), we use the expression for the centre-line velocity in (F.2) to evaluate the volume flux, as

$$Q = \pi^{1/2} w_{\mathrm{m}} K_w y = 2^{3/4} \pi^{1/4} w_0 {b_0}^{1/2} {K_w}^{1/2} y^{1/2} \left(1 + \frac{8R_0}{5} + \frac{\pi^{1/4}}{2^{7/4}} \frac{\phi R_0}{{b_0}^{3/2}} y^{3/2} \right)^{1/3}, \quad \text{(F.3)}$$

and then differentiate with respect to the vertical coordinate to obtain

$$\frac{dQ}{dy} = 2^{3/4} \pi^{1/4} w_0 {b_0}^{1/2} {K_w}^{1/2} y^{-1/2} \frac{1/2 + 4R_0/5 + (\pi^{1/4}/2^{7/4}) \cdot (\phi R_0 / {b_0}^{3/2}) y^{3/2}}{\left(1 + 8R_0/5 + (\pi^{1/4}/2^{7/4}) \cdot (\phi R_0 / {b_0}^{3/2}) y^{3/2} \right)^{2/3}}. \quad \text{(F.4)}$$

This expression is equivalent to twice the entrainment velocity, i.e. $u_{\mathrm{e}} = (1/2) \cdot dQ/dy$. Writing (F.4) in terms of the entrainment model, $u_{\mathrm{e}} = \alpha w_{\mathrm{m}}$, from Taylor (1945), the entrainment coefficient takes the form

$$\alpha = \frac{\pi^{1/2} K_w (1/2 + (4/5 + A y^{3/2}) R_0)}{2(1 + (8/5 + A y^{3/2}) R_0)} \quad \text{where} \quad A = \frac{\pi^{1/4}}{2^{7/4}} \frac{\phi}{{b_0}^{3/2}}. \quad \text{(F.5)}$$

Notice that at the source ($y = 0$), expression (F.5) reduces to

$$\alpha|_{y=0} = \frac{\pi^{1/2} K_w}{4}, \quad \text{(F.6)}$$

which is evaluated as $\alpha = 0.0585$ using the value for the velocity spreading rate of $K_w = 0.132$ as measured by the authors. As $y \to \infty$, (F.5) reduces to

$$\alpha|_{y \to \infty} = \frac{\pi^{1/2} K_w}{2}, \quad \text{(F.7)}$$

which corresponds to a value of $\alpha = 0.1170$ using the aforementioned value of the velocity spreading rate. The values of α at the source and at a large height are close to the average values measured for the jet ($\alpha = 0.05$) and pure plume ($\alpha = 0.13$), respectively (see Chapter 2). This result is consistent with the well known result and our discussion in Chapter 7, specifically, that the forced plume behaves as a jet at its source and asymptotes to a pure plume with height.

F.2 Local Richardson number Γ

Defining the local fluxes of volume, momentum and buoyancy (for Gaussian profiles of velocity and buoyancy) as

$$Q = \pi^{1/2} w_{\mathrm{m}} K_w y, \quad M = 2^{-1/2} \pi^{1/2} {w_{\mathrm{m}}}^2 K_w y, \quad B = \pi^{1/2} g_0' \phi^{-1} {K_w}^{1/2} K_c c_{\mathrm{m}} w_{\mathrm{m}} y, \tag{F.8}$$

respectively, we evaluate the local Richardson number to be

$$\Gamma = \frac{R}{R_{\mathrm{p}}} = \frac{1}{R_{\mathrm{p}}} \frac{BQ^3}{M^3} = \frac{2^{3/2} \pi^{1/2} g_0' {K_w}^{1/2} K_c}{R_{\mathrm{p}} \phi} \left(\frac{c_{\mathrm{m}} y}{{w_{\mathrm{m}}}^2} \right). \tag{F.9}$$

Inputting

$$c_{\mathrm{m}} = \frac{2 b_0 w_0 \phi}{(\pi K_w)^{1/2} K_c} \left(\frac{1}{w_{\mathrm{m}} y} \right) \tag{F.10}$$

and w_{m} from (F.2) into (F.9), we get

$$\Gamma = \frac{2^{7/4} \pi^{3/4} {K_{\mathrm{w}}}^{3/2} R_0}{R_{\mathrm{p}}} \bar{y}^{3/2} \left(1 + \frac{8 R_0}{5} + \left(\frac{\pi}{2} \right)^{1/4} \phi R_0 \bar{y}^{3/2} \right)^{-1}, \tag{F.11}$$

where

$$\bar{y} = \frac{y}{2 b_0} \quad \text{and} \quad R_{\mathrm{p}} = \frac{4 \pi^{1/2} {K_{\mathrm{w}}}^{3/2}}{\phi}. \tag{F.12}$$

Taking the vertical limit $y \to \infty$ of expression (F.11) gives

$$\Gamma|_{y \to \infty} = 1, \tag{F.13}$$

corresponding to a pure plume. However, at the source ($y = 0$) it is clear from (F.11) that

$$\Gamma|_{y=0} = \Gamma_0 = 0. \tag{F.14}$$

This indicates that irrespective of its Γ_0 value, the model treats the flow as a jet ($\Gamma_0 = 0$) at its source. This unphysical result is also the reason for the source value of α in (F.6) corresponding to that of a jet.